Title
Magnetic Reconnection and Turbulence in the Inner Heliosphere

Author
Shi, Chen

Publication Date
2020

Peer reviewed|Thesis/dissertation

UNIVERSITY OF CALIFORNIA
Los Angeles

Magnetic Reconnection and Turbulence in the Inner Heliosphere

A dissertation submitted in partial satisfaction
of the requirements for the degree
Doctor of Philosophy in Geophysics and Space Physics

by

Chen Shi

2020

ABSTRACT OF THE DISSERTATION

Magnetic Reconnection and Turbulence in the Inner Heliosphere

by

Chen Shi
Doctor of Philosophy in Geophysics and Space Physics
University of California, Los Angeles, 2020
Professor Marco Velli, Chair

In this dissertation, we discuss two fundamental processes in the inner heliosphere: magnetic reconnection and turbulence. Understanding the two processes is crucial for a more complete description of the solar atmosphere and solar wind. Our studies are confined within magnetohydrodynamic (MHD) and Hall-MHD regimes. We employ methods of linear stability analysis, numerical simulation, as well as satellite data analysis. The main results of our studies are summarized as follows. (1) Through linear stability calculation and linear MHD simulations, we confirm that the inhomogeneous flow inside a reconnecting current sheet stabilizes the tearing instability. The threshold Lundquist number S_c for stabilization is on the order of 10^4. (2) Through nonlinear Hall-MHD simulations, we show that during the "recursive" reconnection process driven by tearing instability, the generation of secondary plasmoids is suppressed as the system scale approaches the ion inertial length. (3) We calculate the linear dispersion relation of the tearing instability under a generalized three-dimensional configuration with Hall effect and guide field. We show that the largest linear growth rate is in general found in parallel modes rather than oblique modes, regardless of the guide field strength. (4) We carry out high-resolution two-dimensional MHD simulations, based on expanding-box-model (EBM), of Alfvén waves propagating inside large-scale solar wind streams. We show that the stream structures significantly impact the evolution of Alfvénic turbulence properties, such as the cross helicity and residual energy. (5) Through

the EBM simulations in combination with a superposed-epoch analysis using OMNI data set, we show that, around heliospheric current sheets (HCSs), the Alfvénicity of the solar wind turbulence is destroyed. (6) We analyze Parker Solar Probe (PSP) data of the first four orbits and carry out a statistical study of the turbulence properties in the young solar wind. A radial evolution of various turbulence properties is observed in the data.

The dissertation of Chen Shi is approved.

Vassilis Angelopoulos

Christopher Russell

Troy Carter

Marco Velli, Committee Chair

University of California, Los Angeles

2020

Table of Contents

List of Figures

List of Tables

Acknowledgements

I greatly thank my PhD advisor Prof. Marco Velli for his help in preparing this dissertation. As my supervisor, he guided me for the past five years in many aspects. Marco is an extremely nice person and an excellent scientist. He not only helped me in solving professional problems but also provided me with great opportunities for academic success such as attending various conferences.

I also want to thank my collaborators Anna Tenerani, Fulvia Pucci, Franco Rappazzo,Victor Réville, Maria Elena Innocenti and Olga Panasenco. I learned a lot from them, including physics and numerical simulation technique.

I would like to thank Prof. Vassilis Angelopoulos, Prof. Ray Walker, Prof. Christopher Russell, and other faculty members in EPSS and AOS of UCLA. They gave me a lot of helpful advice on research and presentation of my research. Prof. Vassilis Angelopoulos helped a lot on my application of postdoc jobs. Prof. Ray Walker trained me when I prepared for the qualification exam. I also thank Prof. Troy Carter for being my dissertation committee member.

I appreciate the effort made by EPSS staff, especially Lauri Holbrook and Richard Fort. They got everything well arranged for me so that my life at UCLA went smoothly.

I cherish the memory of happy times spent with other PhD students and researchers at UCLA. Xin An, Xu Zhang, Zixu Liu, San Lu, and many others are not only excellent colleagues but also great friends.

Last, I would like to thank my wife Kun Zhang and my parents. They are always supporting and encouraging me.

Section 2.1 is a version of (Shi et al., 2018). Section 2.2 is a version of (Shi et al., 2019). Section 3.1 is a version of (Shi et al., 2020).

Curriculum Vitae

2011 – 2015	B.S. in Space Physics, Peking University, Beijing, China.
2015 – Present	Ph.D. student in Geophysics and Space Physics, University of California, Los Angeles.

Publications

Shi, C., Velli, M., & Tenerani, A., "Marginal stability of Sweet–Parker type current sheets at low Lundquist numbers", ApJ, 859, 2 (2018)

Shi, C., Tenerani, A., Velli, M., & Lu, S., "Fast recursive reconnection and the Hall effect: Hall-MHD simulations", ApJ, 883, 2 (2019)

Shi, C., Velli, M., Tenerani, A., Rappazzo, F., & Réville, V., "Propagation of Alfvén waves in the expanding solar wind with the fast-slow stream interaction", ApJ, 888, 2, (2020)

Shi, C., Velli, M., Tenerani, A., Rappazzo, F., & Réville, V., "Turbulence in the solar wind: influence of the heliospheric current sheet", in preparation for ApJ

Shi, C., Velli, M., Pucci, F., Tenerani, A., & Innocenti, M. E., "Oblique tearing mode instability: guide field and Hall effect", in preparation for ApJ

Réville, V., Velli, M., Panasenco, O., et al., "The role of Alfvén wave dynamics on the large scale properties of the solar wind: comparing a MHD simulation with PSP E1 data", ApJS, 246, 2 (2020)

Tenerani, A., Velli, M., Matteini, L., et al., "Magnetic Field Kinks and Folds in the Solar Wind", ApJS, 246, 2 (2020)

Panasenco, O., Velli, M., D'Amicis, R., et al., "Exploring Solar Wind Origins and Connecting Plasma Flows from the Parker Solar Probe to 1 au: Nonspherical Source Surface and Alfvénic Fluctuations", ApJS, 246, 2 (2020)

Lu, S., Angelopoulos, V., Artemyev, A. V., et al., "Turbulence and Particle Acceleration in Collisionless Magnetic Reconnection: Effects of Temperature Inhomogeneity across Pre-reconnection Current Sheet", ApJ, 878, 109 (2019)

Liu, H., Zong, Q.-G., Zhang, H., et al., "The Geometry of an Electron Scale Magnetic Cavity in the Plasma Sheet", GRL, 46 (2019)

CHAPTER 1

Introduction

1.1 Solar Atmosphere and Solar Wind

The Sun is the closest star to the Earth, which is orbiting the Sun and is greatly affected by solar activity. Although people have been observing the Sun since ancient times, it is only within the last century that people have gradually established a comprehensive and deep understanding of the physical processes related to the Sun, attributed to the advancement of observational technologies and fundamental physics.

Surrounding the Sun is the solar atmosphere which extends to several solar radii before it is accelerated to supersonic speed and becomes the *solar wind*. We now know that the solar atmosphere is highly ionized and consists mainly of electrons and protons. This state of matter is what we call *plasma*. The quiet solar atmosphere can be divided roughly in four layers, namely *photosphere*, *chromosphere*, *transition region* and *corona* from bottom to top. Figure 1.1 shows the temperature as a function of height from the visible bottom of the solar atmosphere in log-linear scale. In the photosphere, the temperature drops with height from about 10^4K and reaches its minimum value at the boundary between photosphere and chromosphere. Then the temperature starts to increase gradually in the choromosphere and reaches $T \sim 10^6$K in the low corona after a sudden increase in the transition region. The solar atmosphere is actually highly dynamic. Physical processes on different time scales are happening all the time. For example, the sunspot and solar activity vary on the 11-year solar cycle; active regions (AR) typically last for days; and solar flares and coronal mass ejections (CME) happen from hours to minutes. Especially, the explosive phenomena happening in the solar atmopshere such as the solar flares and CMEs are accompanied by release of a

huge amount of energy and mass, which may impact the Earth and cause severe damage to human-made satellites and ground based electronic devices.

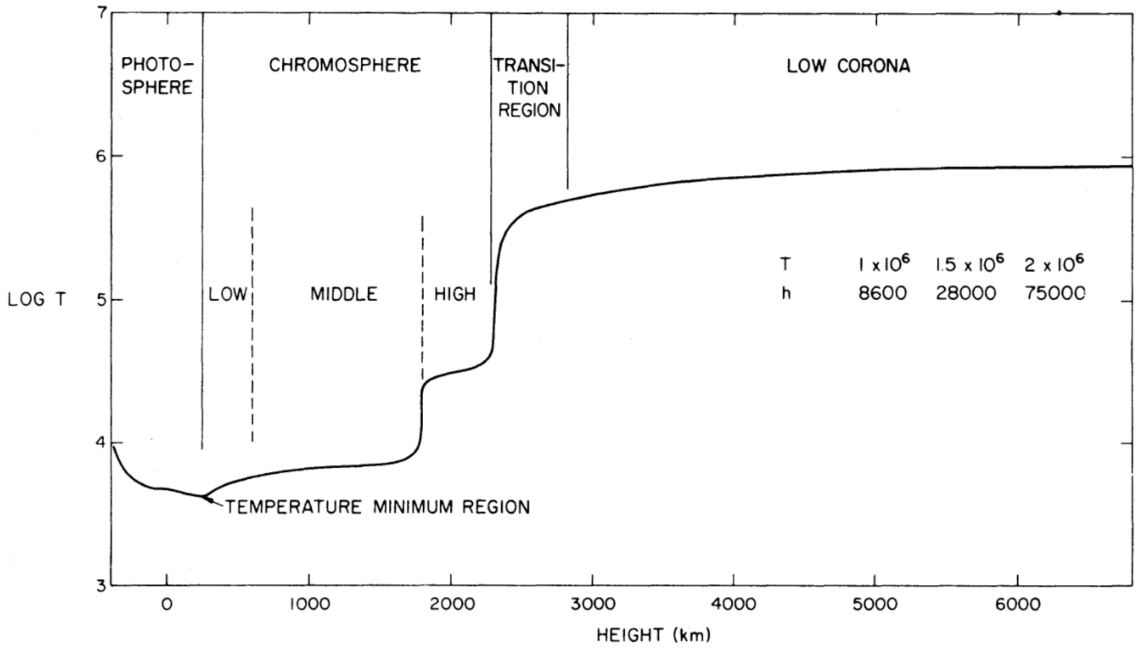

Figure 1.1: Temperature as a function of height from the visible bottom of the solar atmosphere. Figure I-1 of (Athay, 2012).

Parker (1958) pointed out that the extremely hot solar corona can escape solar gravity and expands supersonically into interplanetary space. These expanding plasma streams are the solar wind. The solar wind propagates outward until the edge of the heliosphere, i.e. the *termination shock*, as shown in Figure 1.2. It impacts objects inside the solar system such as the planets, comets and asteroids, etc. Especially, the solar wind interacts with the magnetic field of planets such as the Earth and leads to the formation of *magnetosphere* as shown in Figure 1.3. Energy is injected from the solar wind into the magnetosphere and the storage of energy inside the magnetosphere causes various space weather phenomena, e.g. the *magnetic storms* and *substorms*.

The explosive phenomena that happen in the solar atmosphere, together with the continuously blowing solar wind, are major topics of the heliospheric study as they significantly influence the well being of human society and lives. Since the 1950s, numerous man-made

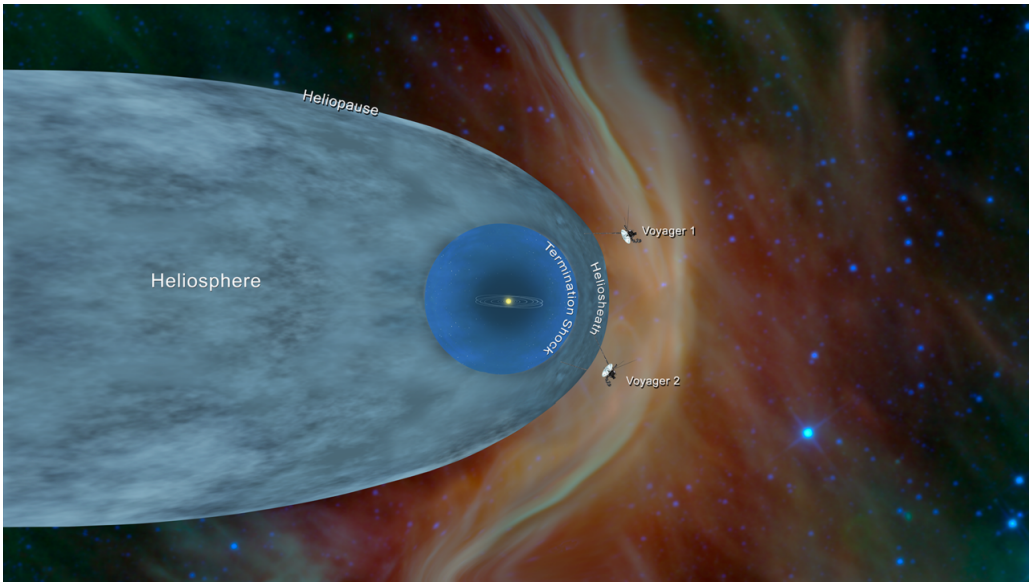

Figure 1.2: Structure of the outer heliosphere. NASA website.

satellites as well as ground based telescopes have collected a huge volume of valuable in-situ and remote-sensing data, greatly enhancing our knowledge of these phenomena. Two fundamental physical processes are believed to be crucial for fully understanding the complex processes in solar atmosphere and solar wind, namely *magnetic reconnection* and *turbulence*. Thus, in the following two subsections, we introduce the two topics in more detail.

1.2 Magnetic Reconnection and the Tearing Instability

Magnetic reconnection is a process that converts magnetic energy into kinetic and thermal energies of the ambient plasma. It is believed to be the underlying mechanism to explain most, if not all, of the explosive phenomena happening in Space.

The first theoretical model of reconnection was established in 1950s, by (Sweet, 1958) and (Parker, 1957), namely the *Sweet-Parker current sheet model*. In the framework of ideal *magnetohydrodynamics* (MHD), magnetic field lines cannot reconnect because they are "frozen" in the plasma. Thus, a resistivity, or equivalently magnetic diffusivity, is adopted in the Sweet-Parker model. In this case, a thin boundary layer, i.e. the current sheet, is

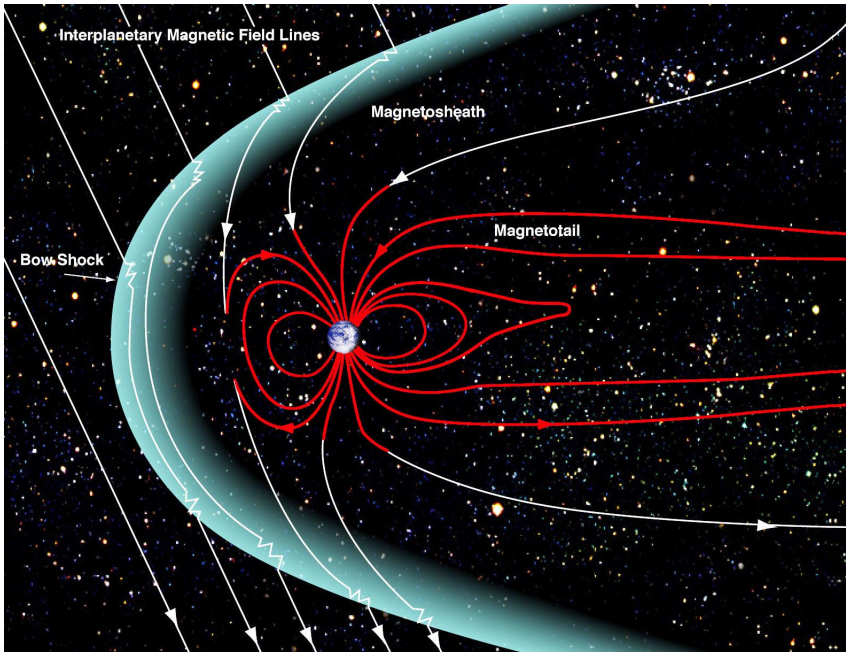

Figure 1.3: Interaction between the solar wind and Earth's magnetosphere. NASA website.

formed and maintained by the balance between the plasma inflow and diffusion of magnetic field. An important dimensionless parameter in this model is the *Lundquist number* S, defined by $S = LV_A/\eta$, where L is the length of the current sheet, V_A is the upstream Alfvén speed and η is the magnetic diffusivity. A simple analysis of the momentum equation and induction equation shows that in a Sweet-Parker type current sheet the inverse aspect ratio of the current sheet a/L, where a is the thickness of the current sheet, follows the relation $a/L \sim S^{-1/2}$. In astrophysical environments, S is typically huge ($S \gtrsim 10^8$ in the solar atmosphere), makes the Sweet-Parker current sheets extremely thin. This is a bottleneck for the reconnection rate R that may be defined as the rate of magnetic flux that is reconnected at the sheet. In a stationary scenario this flux is diffused by effective resistivity within the sheet: for the Sweet-Parker configuration considered above, this leads to a value $\sim u_{in}/V_A$ when normalized by the typical Alfvénic propagation time. However $u_{in}/V_A \sim S^{-1/2}$ from the balance of momentum across the sheet. In other words the extremely small thickness of the sheet requires a very small inflow speed, limiting the reconnection rate.

A more promising model was proposed by Petschek (1964). In *Petschek's model*, the

diffusion region is limited to a very small area so that a large opening angle is allowed, leading to a larger reconnection rate compared with Sweet-Parker model. However, MHD simulations confirmed that Petschek's scenario cannot be achieved if the resistivity is uniform in space (Biskamp, 1986). It was not until late 1990s that great progress was made in understanding magnetic reconnection, thanks to the improvement of computing capability. Researchers started to carry out simulations beyond the MHD regime, including the Hall-MHD, two-fluid and particle-in-cell (PIC) simulations (Birn et al., 2001). These simulations showed that, once kinetic effects were taken into account, reconnection enters a regime significantly different from the MHD case. A universally applicable reconnection rate $R \sim 0.1$ is achieved no matter which numerical model is chosen. Especially, PIC simulations greatly deepen our insight into the microscale, i.e. electron-scale, physics in magnetic reconnection (e.g. Daughton et al., 2006). Besides the numerical works, the Magnetosphere Multiscale (MMS) mission launched in 2015 also provides important data with resolution to electron scales (Burch et al., 2016a) and its data enhances people's understanding of reconnection in Earth's magnetopause and magnetotail. It is widely accepted that at kinetic scales, reconnection happens in a two-layer structure. As shown in Figure 1.4, near the reconnection site, or "X-point", the kinetic effect happens first in the ion scale, or *ion inertial length* more precisely, decoupling ions from the magnetic field, forming the *ion diffusion region*. In the ion diffusion region, magnetic field lines are frozen in the electron flow only. Further down to the electron scale, or *electron inertial length*, electrons decouple from the magnetic field and electron physics plays a major row, forming the *electron diffusion region*. Many studies were carried out on the electron physics (e.g. Burch et al., 2016b) and they show that electron dynamics is crucial in understanding the energy dissipation mechanism in magnetic reconnection.

Despite the progress in kinetic-scale reconnection, we are still left with the problem of how fast reconnection is triggered starting from MHD scales. In the solar atmosphere, explosive processes such as CMEs and solar flares are magnetohydrodynamic, i.e. much larger than the ion inertial length. Consequently, MHD-scale mechanism must be sought to explain the triggering of these processes and the *tearing instability* is a good candidate.

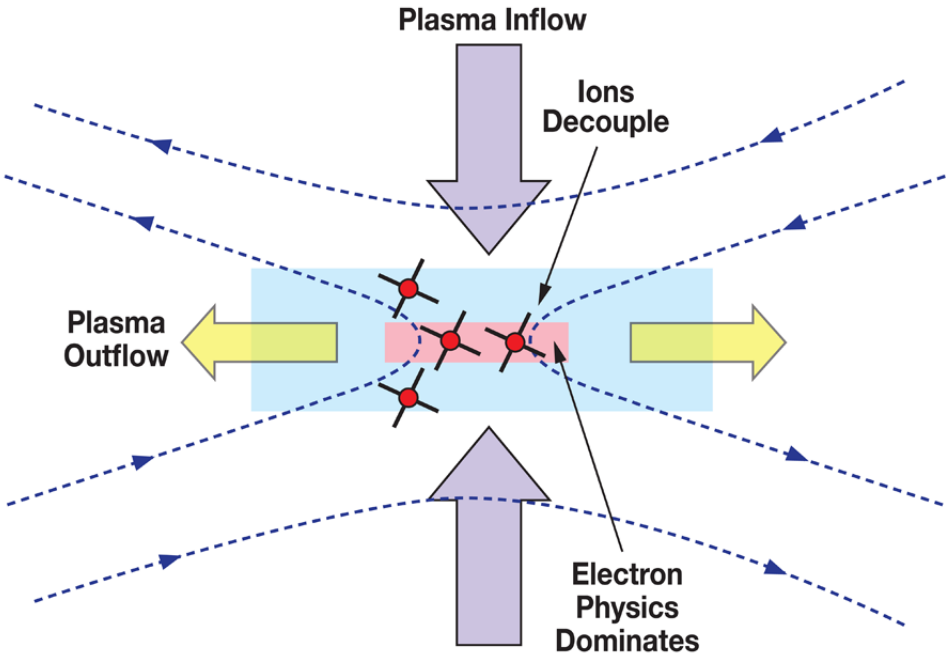

Figure 1.4: Illustration of the ion diffusion region and electron diffusion region. MMS website.

Tearing instability was first analyzed by Furth et al. (1963) and further developed by others (e.g. Coppi et al., 1966). These first analyses of tearing instability showed that, in a one-dimensional current sheet, there exists a fastest-growing mode that has a wave number $ka \sim S^{-1/4}$ and growth rate $\gamma\tau \sim S^{-1/2}$ where a is the thickness of the current sheet, $\tau = a/V_A$ is the Alfvén crossing time, V_A is the upstream Alfvén speed and $S = aV_A/\eta$ is the Lundquist number measured by a. However, from the above scaling relation, it is immediately seen that the growth rate of the tearing instability is extremely slow when $S \to \infty$. Thus, the tearing instability was not considered as a plausible explanation for fast reconnection in the solar atmosphere for decades. Loureiro et al. (2007) showed that, if a two-dimensional Sweet-Parker type current sheet is considered and we re-normalize the scaling relations of the tearing mode using the length L instead of the thickness a of the current sheet, we will get $kL \sim S_L^{3/8}$ and $\gamma\tau_L \sim S_L^{1/4}$, i.e. a positive scaling of the growth rate to Lundquist number (see also Tajima & Shibata, 2002). In reality, a general formula can be derived by assuming an arbitrary aspect ratio of the current sheet, say $a/L \sim S_L^{-\alpha}$

and we get $\gamma\tau_L \sim S_L^{-(1-3\alpha)/2}$ (Pucci & Velli, 2013). That is to say, for a current sheet with large thickness $a/L > S_L^{-1/3}$, the growth rate of tearing instability has a negative scaling relation with S_L and vice versa. This result indicates that, in the case of a huge Lundquist number S_L, there exists a critical inverse aspect ratio of a current sheet $a/L \sim S_L^{-1/3}$ such that above this value the tearing instability has nearly-zero growth rate and below this value the tearing instability has nearly-infinite growth rate. In the case $a/L = S_L^{-1/3}$, the growth rate of tearing instability is finite ($\gamma\tau_L = 0.62$) and is independent of S_L, or "ideal" (Pucci & Velli, 2013). Based on the *ideal-tearing* scenario, Tenerani et al. (2015) proposed the fast *recursive reconnection* process, similar to the "fractal" reconnection proposed by Shibata & Tanuma (2001). The core idea is that, an initially macroscopic current sheet, say in the solar atmosphere, collapses due to some external force such as compression and the thickness of the current sheet decreases. After the thickness of the current sheet approaches critical value, i.e. $a/L \sim S_L^{-1/3}$ for ideal tearing (or $a/L \sim S_L^{-1/2}$ for Sweet-Parker current sheet adopted by Shibata & Tanuma (2001)), instability grows fast and generates second order current sheets and plasmoids. These newly-formed current sheets dynamically lengthen and break into higher order current sheets when the critical aspect ratio is reached. This process happens recursively so that an initially macroscopic current sheet is destroyed and releases energy rapidly. Figure 1.5 shows the result from a 2.5D MHD simulation carried out by Tenerani et al. (2015). Color shows current density and we can observe the recursive formation of high order current sheets.

In conclusion, recursive reconnection is a good candidate to explain the transition to fast reconnection in solar atmosphere. However, there are many missing pieces in a complete description of this process, one of which is how the recursive process is stopped at small scales. There are two possibilities as the recursive reconnection proceeds: one is that the Lundquist number of high order current sheets becomes sufficiently small such that the tearing instability is stabilized, the other is that the size of the micro-scale current sheets approaches kinetic scale, i.e. ion inertial length, such that kinetic effect plays an important role and significantly modifies the process. Besides, understanding the stabilization mechanism of a

current sheet is also crucial for solving the onset problem of fast reconnection. Thus, we carried out two studies, one discussing the stabilizing role the background plasma flow on the linear tearing instability in the framework of linear MHD, the other discussing the role of Hall effect on the recursive tearing using Hall-MHD numercial simulations. In addition, we also carry out a study on the three-dimensional tearing instability with emphasis on the roles of guide field and Hall effect. These studies are presented in Chapter 2.

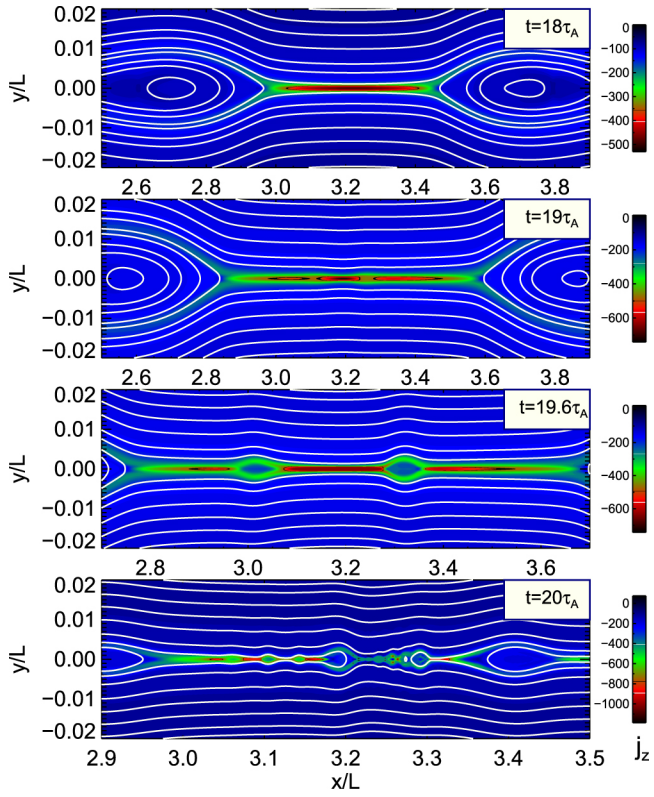

Figure 1.5: Current density in a recursive reconnection process. 2.5D MHD simulation by (Tenerani et al., 2015)

1.3 Turbulence in the Solar Wind

Turbulence is a ubiquitous process in nature, arising in air and fluids on the Earth but also present in astrophysical plasmas. The most intense studies of turbulence are carried out in the fields related to neutral fluids such as aerodynamics since turbulence is a major hazard in

engineering. But study of plasma turbulence is also necessary, not only because turbulence in plasma is quite different from, or more complicated than, the turbulence in the neutral fluids in the sense of fundamental physics, but also because it is crucial in understanding various important processes in astrophysical plasmas such as the plasma heating. Although people have noticed the phenomenon of turbulence for centuries, e.g. the drawings of turbulent flows by Leonardo da Vinci in the 16th century, the first and most important phenomenological model of turbulence was established only around mid-20th century by Kolmogorov (1941).

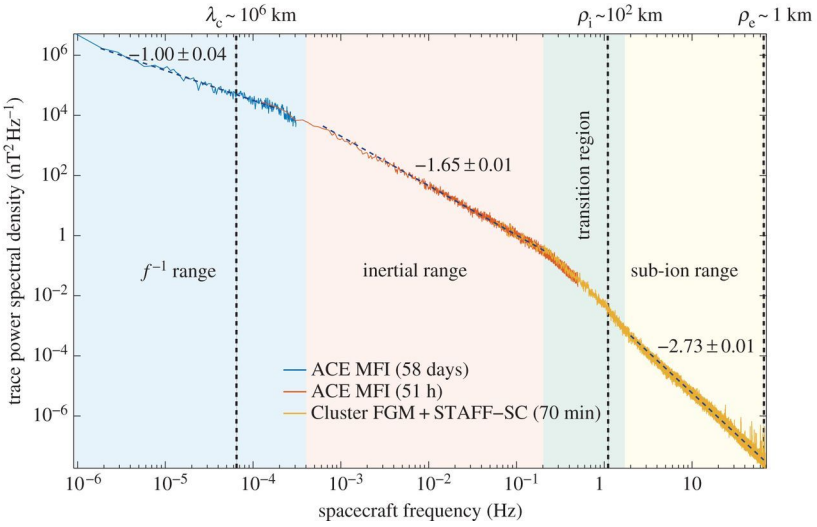

Figure 1.6: Power spectrum of solar wind magnetic field. (Kiyani et al., 2015).

Here we introduce the most fundamental concepts in *Kolmogorov's turbulence theory*, which is the basis for analysis of any turbulent system. Figure 1.6 shows the averaged power spectrum of magnetic field fluctuations in the solar wind. Abscissa is frequency in spacecraft frame, which can be mapped to wave number using Taylor hypothesis $kU \approx f$ where k is the wave number, U and f are the mean flow speed and frequency in spacecraft frame. Note that Taylor hypothesis is applicable only when the wave speed is small enough compared with the solar wind speed. The most prominent feature of the power spectrum is that it can be clearly divided into three regions. From large to small scales are the so called *energy containing scales*, *inertial scales*, and *dissipation scales*. In Kolmogorov's model, a fully-developed turbulent system has its energy injected into the energy-containing scales

by external forces and dissipated eventually in the dissipation scales through mechanisms such as viscosity. In the inertial scales where nonlinear interaction dominates, energy is neither injected nor dissipated but merely transferred between scales because the nonlinear interaction conserves the total energy of the system. Kolmogorov assumed that the energy transfer only happens between adjacent scales, i.e. energy flows from large to small scales inside the inertial range, and as a result the *energy transfer rate* must be a constant in a stable turbulence system. The energy transfer rate is determined by the dominant *nonlinear interaction* in the system. For example, in neutral fluid which is described by the Navier-Stokes equation, the nonlinear term $\mathbf{u} \cdot \nabla \mathbf{u}$ where $\mathbf{u}$ is the velocity field gives the energy transfer rate $\varepsilon \sim ku^3$ where k is the wave number. With the estimate $u \sim \sqrt{kE}$ where E is the power spectrum density, we immediately get $E \sim \varepsilon^{2/3} k^{-5/3}$, i.e. the slope of the power spectrum is $-5/3$ in log-log scale. This is the famous Kolmogorov's $-5/3$ law.

As mentioned before, plasma turbulence is very different from turbulence in neutral fluids, because of the more complex physical model that describes a plasma. A plasma is a multi-scale system, owning distinguishing physics at different scales. From large to small, these scales are the MHD scale at which the plasma is described by the one-fluid MHD model, the ion scale at which the ion kinetic effect is dominant, and the electron scale at which the electron kinetic effect is dominant. At different scales, the dominant nonlinear interaction varies potentially, resulting in power spectra of different slopes. From this point of view, the three-part description of the turbulence spectrum is improper for plasma turbulence because we actually expect a spectrum with more than three regions. In Figure 1.6, the "inertial range" is dominated by MHD physics with a spectral slope around $-5/3$ and below the inertial range there is the sub-ion range dominated by ion kinetic physics with a steeper spectrum (the vertical dashed line marks the ion inertial length). But if we go down to smaller scales i.e. below the electron inertial length which is not shown in this figure, we expect to see a new segment with a different slope because in this range the electron physics dominates.

In this dissertation, we focus on turbulence in the solar wind, where MHD turbulence is of

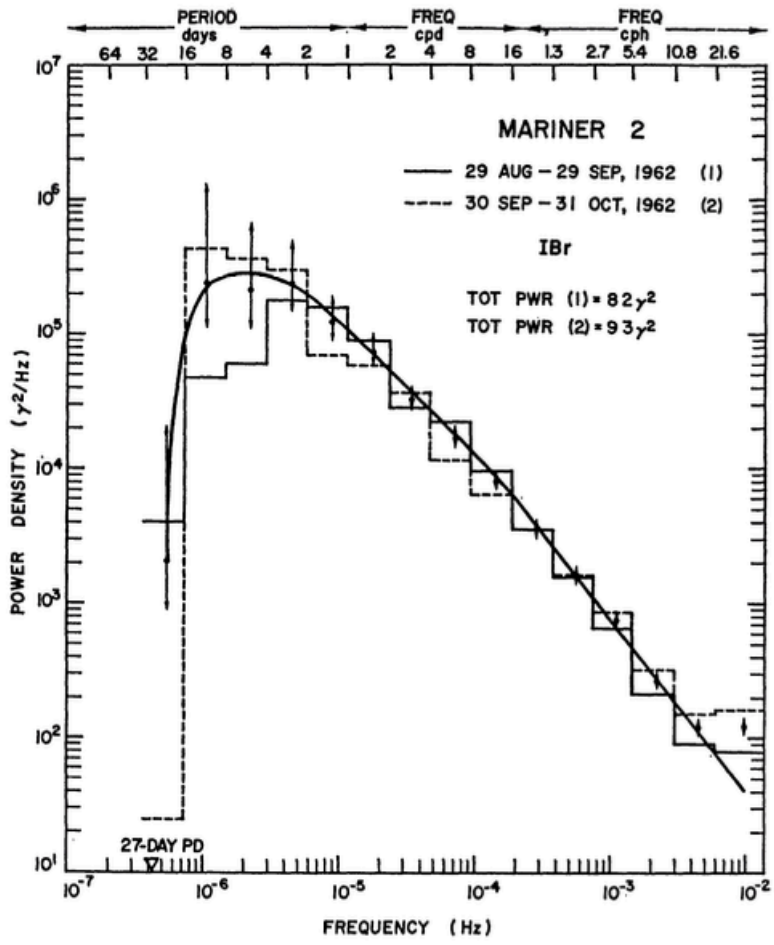

Figure 1.7: Spectrum of B_r measured by Mariner 2. (Coleman, 1968).

most interest. The study of fluctuations in the solar wind started in 1960s, when man-made satellites started to collect data in the solar wind. Figure 1.7 shows the power spectrum density of the radial magnetic field using Mariner 2 data (Coleman, 1968). It is the first measured power spectrum of solar wind fluctuations. From this figure, we clearly see nearly-straight line segments in log-log scale, indicating that the fluctuations are fully-developed turbulence. Another important feature of the solar wind fluctuations can be observed in Figure 1.8, produced by Belcher & Davis Jr (1971). Figure 1.8 shows a 24-hour magnetic field and plasma observation made by Mariner 5. Top three panels are three components of magnetic field and velocity fluctuations and bottom panel shows the magnitude of magnetic field and proton number density. We can see from this figure that the magnetic field and

velocity fluctuations are highly correlated while the polarity of the radial magnetic field is negative. In addition, $|\mathbf{B}|$ and N remain nearly constant, meaning that the plasma is nearly incompressible. These two features indicate that the fluctuations are highly *Alfvénic*. More precisely, these fluctuations are mainly *spherically polarized Alfvén waves* propagating *outward* from the Sun. The origin of these Alfvén waves is believed to be in the low solar atmosphere at open magnetic field regions (e.g. Osterbrock, 1961; Kuperus et al., 1981; Cranmer & Van Ballegooijen, 2005). Study of the origin and propagation of Alfvén waves inside the solar atmosphere is beyond the scope of this dissertation whose focus is on the evolution of the Alfvén waves and the Alfvénic turbulence inside the solar wind that is already accelerated.

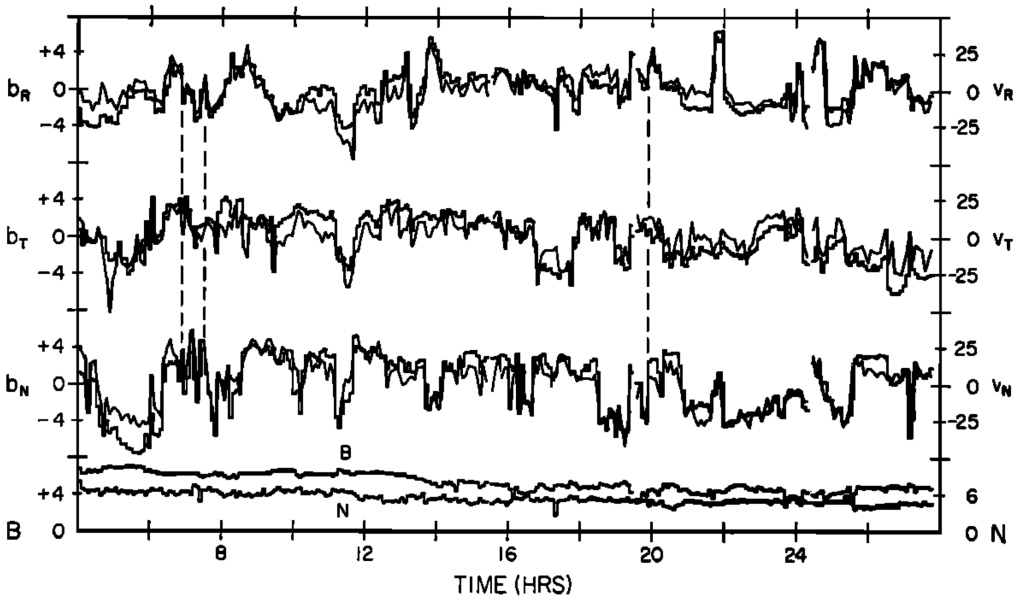

Figure 1.8: Magnetic field and plasma data from Mariner 5. Top three panels are the three components of magnetic field and velocity fluctuations. Bottom panel shows magnetic field magnitude and proton number density. (Belcher & Davis Jr, 1971).

Following the early observational works reviewed in the prior paragraph, numbers of theories on the propagation of Alfvén waves in the solar wind were developed subsequently, including WKB theories (Alazraki & Couturier, 1971; Belcher, 1971; Hollweg, 1974) and non-WKB theories (Heinemann & Olbert, 1980; Barkhudarov, 1991; Velli, 1993). The WKB

theories, in which the wave length is much smaller than the scale length of the solar wind inhomogeneity so that there is little wave reflection, reveal the radial evolution of the Alfvén wave amplitude under the effect of the background solar wind profile. The non-WKB theories show that the linear coupling between the outward and inward Alfvén waves leads to a frequency-dependent reflection of the waves. Bavassano et al. (1982), using Helios 1 & 2 magnetic field data, showed that the power spectra of the MHD turbulence inside the trailing edge of the solar wind steepen toward Kolmogorov's $-5/3$ prediction or Iroshnikov-Kraichnan's $-3/2$ prediction (Iroshnikov, 1964; Kraichnan, 1965), indicating that nonlinear process is taking effect. Note that, Iroshnikov-Kraichnan's theory assumes that the dominant nonlinear interaction is that exists between two counter-propagating Alfvén wave packets and thus with a strong background magnetic field the nonlinear energy transfer rate is weakened because the background field shortens the interaction time between the two wave packets. As a result, with a strong background magnetic field, the Alfvénic turbulence is expected to have a shallower power spectrum compared with the pure hydrodynamic case. Since the 1980s, efforts were made to derive models that properly describe the MHD turbulence evolution in the solar wind (e.g. Tu et al., 1984; Zhou & Matthaeus, 1990; Zank et al., 1996) and these models are successful in explaining some of the observed features of the MHD turbulence such as the steepening of the power spectra but they are not fully self-consistent and usually bear some arguable assumptions. Thus, direct numerical simulations were also carried out in order to reproduce the observed turbulence properties in a more self-consistent manner (e.g. Roberts et al., 1992; Grappin & Velli, 1996).

In the last three decades, more space missions, e.g. Ulysses, WIND, etc., provide researchers with more and more data, which greatly enhanced our understanding of the solar wind turbulence. Especially, Ulysses, which is a polar orbiter of the Sun and moves between 1.35 AU to 5.4 AU, allows better studies of the radial evolution of the turbulence inside the high speed stream. In addition, missions like WIND and ACE continuously collect data at 1 AU for over two decades and thus established a huge data set suitable for statistical analysis of the solar wind turbulence. Indeed, a large number of studies were carried out

using these data. However, there are still some unresolved problems left. In this dissertation, we aim to tackle the question that how the large-scale structures in the solar wind, i.e. the stream interaction regions and heliospheric current sheets, affect the turbulence evolution. The method we adopt is mainly MHD simulations but we also carry out a statistical study using the satellite data.

1.4 Parker Solar Probe

Parker Solar Probe (PSP) was launched on August 12th, 2018. Within 6 years, it will lower the perihelion of its orbit, with assistance of Venusian gravity, to around 8.86 solar radii, or around 0.04 AU from the surface of the Sun (photosphere) (Figure 1.9). It is the first human-made satellite that travels to such a close distance to the Sun and will start a new era of solar physics research.

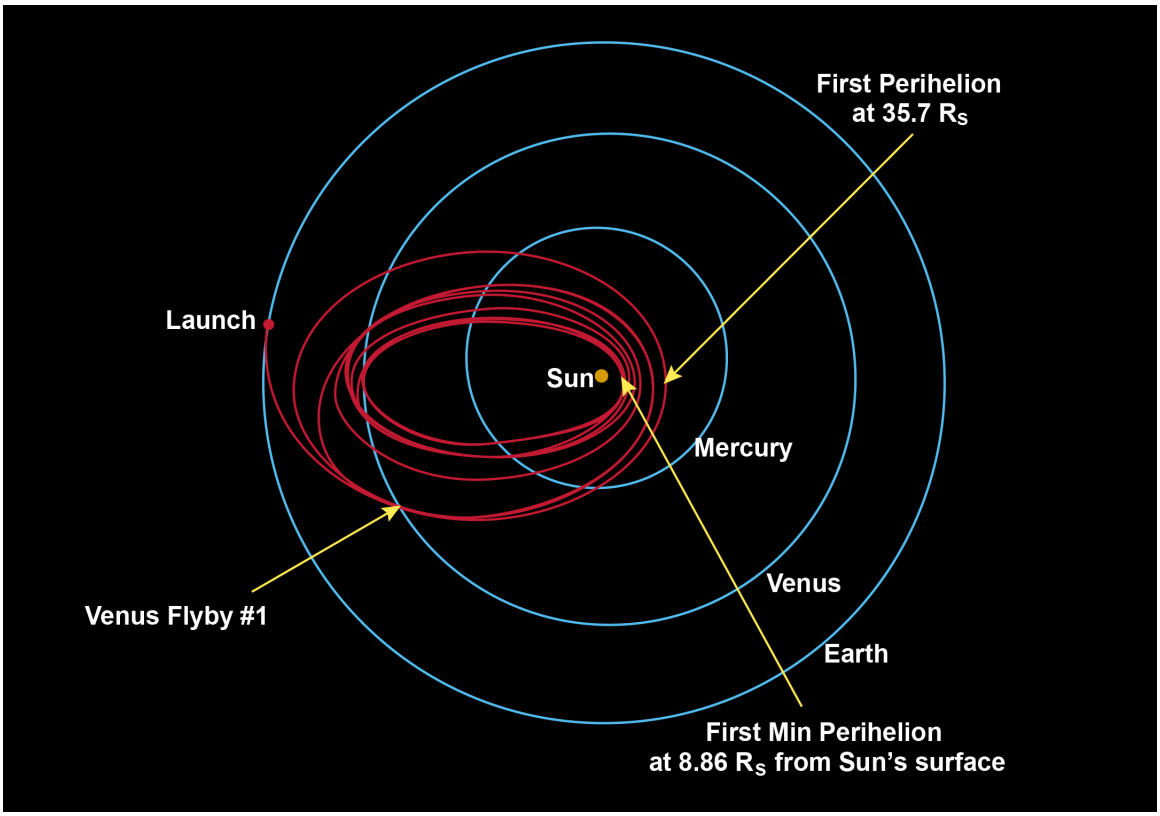

Figure 1.9: Orbits of Parker Solar Probe.

PSP has three main scientific objectives: (1) Trace the flow of energy that heats and accelerates the solar corona and solar wind. (2) Determine the structure and dynamics of the plasma and magnetic fields at the sources of the solar wind. (3) Explore mechanisms that accelerate and transport energetic particles. These are three of the fundamental problems left in the field of solar physics. To answer these questions, PSP has four instrument suites onbard: (1) Fields Experiment (FIELDS); (2) Integrated Science Investigation of the Sun (ISIS); (3) Wide-field Imager for Solar PRobe (WISPR); (4) Solar Wind Electrons Alphas and Protons (SWEAP) Investigation. These instruments are able to provide comprehensive data set of the solar wind and solar atmosphere, including white light images (by WISPR), magnetic and electric fields (by FIELDS), high energy particles (by ISIS), and distribution functions of ions and electrons (by SWEAP). In particular, combined measurements of FIELDS and SWEAP is very suitable for study of turbulence in the young solar wind. Among the first results of PSP data, many interesting findings on solar wind turbulence were made. For example, Chen et al. (2020) confirmed that there is an increase in the wave energy level and the dominance of outward propagating Alfvén waves as we get closer to the Sun. de Wit et al. (2020) and McManus et al. (2020) illustrated that the *magnetic switchbacks*, which are found to be ubiquitous in young solar wind (e.g. Bale et al., 2019), may have significant impact on turbulence properties.

As PSP is continuously producing new data at lower and lower orbits, it is worth examining the data in more detail. In this dissertation, we present some preliminary results using PSP data and propose to carry out more studies in the future.

1.5 Outline

The dissertation is organized as follows. In Chapter 2, we present our studies concerning the magnetic reconnection. We first discuss the marginal stability of linear tearing instability inside the Sweet-Parker type currents and then show results of the nonlinear simulations of the recursive tearing instability with the Hall effect. In the last part of Chapter 2, we present linear analysis of the three-dimensional tearing instability with Hall effect and guide field.

Chapter 3 contain studies of the solar wind turbulence. We first illustrate the numerical method, i.e. the expanding-box-model (EBM), adopted for our simulations and then show the simulation results of how the stream interaction regions affect the Alfvénic turbulence in the solar wind. Subsequently, we present simulations and a superposed-epoch analysis using OMNI data of the turbulence properties around heliospheric current sheets. In the last part of Chapter 3, we introduce the instruments and data of PSP and present preliminary results on turbulence in the young solar wind using PSP data. In Chapter 4, we conclude this dissertation and propose future studies.

CHAPTER 2

Magnetic Reconnection and the Tearing Instability

In this chapter, we discuss the following topics related to tearing mode instability. In Section 2.1[1], we discuss how the background flow inside a current sheet stabilizes the tearing instability. In Section 2.2[2] we show simulations on how the nonlinear recursive tearing is affected by a finite ion inertial length. In Section 2.3 we present linear stability calculation of oblique tearing modes under the influence of a guide field and the Hall effect. In Section 2.4 we conclude this chapter.

2.1 Marginal Stability Analysis of Sweet-Parekr Type Current Sheets at Low Lundquist Numbers

2.1.1 Introduction

One long-standing problem in the study of tearing instability is how a current sheet is stabilized at low Lundquist numbers. It was found through 2D MHD simulations that only when a current sheet becomes very long and thin it becomes tearing unstable and the critical aspect ratio is $a/L \sim 100$, i.e. corresponding to a Lundquist number $S = 10^4$ for a Sweet-Parker type current sheet (Biskamp, 1986). Besides, as mentioned in Chapter 1, stabilization of the microscopic current sheets is a possible mechanism that stops the fast recursive reconnection. Bulanov et al. (1978) proposed that, unlike static current sheets which are always unstable (albeit to the very slow, for macroscopic current layers, tearing

[1]This section is a version of (Shi et al., 2018)

[2]This section is a version of (Shi et al., 2019)

instability), the inhomogeneous outflow in the current sheet can have a stabilizing effect, leading to a Lundquist number threshold for stability.

More recently a 2D linear MHD simulation by Ni et al. (2010) confirmed that, though the effect of flows is negligible when S is large, its importance increases with decreasing S. In their simulations, initial random perturbations grow linearly at first but then saturate. They determine a critical Lundquist number $S \sim 2000$ at which the random perturbation only grows by a factor of 5. The simulation by Ni et al. (2010) is periodic in the outflow direction but employs a "viscous buffer region" at the outer boundaries where viscosity is very large to damp out perturbations: the need to have vanishing boundary conditions and associated damping regions might therefore influence the stability criterion significantly. Indeed, realistic background configurations are periodic neither in the outflow nor inflow directions, rather the flow is accelerated into a jet diverging from the sheet at the background Alfvén speed.

In this study, we carry out linear MHD simulations and linear stability analysis of 2D Sweet-Parker type current sheets at low Lundquist numbers ($S \leq 10^4$). We use open boundary conditions in both the inflow and outflow directions in the simulations. Our result shows that the inhomogeneous outflow stretches the magnetic islands forming and growing in the current sheet while at the same time evacuating them from the simulation domain. Both stretching and evacuation play a stabilizing role. The stretching effect decreases the growth rate and changes the linear instability from an exponential behavior typical of the static instability, to one in which growth is only exponential over a limited time-interval and then gradually saturates due to the decrease of the effective wave number. The evacuation of magnetic islands limits the growing period to several Alfvén crossing times before the magnetic islands are ejected out of the current sheet and hence limits the total growth of the initial perturbations.

The following section describes our numerical method; Section 2.1.3 describes the numerical results. Sections 2.1.4 and 2.1.5 then describe SP stability while Section 2.1.6 shows numerical results for a different background configuration. Section 2.1.7 summarizes this

part of work.

2.1.2 Numerical Method and Simulation Setup

The governing equations for analysis of the resistive instability are given by the linearized resistive MHD equations (and the adiabatic equation for closure - this decouples the dynamic instability from potential thermodynamic effects):

$$\frac{\partial \rho_1}{\partial t} + \mathbf{u_0} \cdot \nabla \rho_1 + \rho_0 \nabla \cdot \mathbf{u_1} + \mathbf{u_1} \cdot \nabla \rho_0 + \rho_1 \nabla \cdot \mathbf{u_0} = 0 \tag{2.1a}$$

$$\begin{aligned} \frac{\partial \mathbf{u_1}}{\partial t} + \mathbf{u_0} \cdot \nabla \mathbf{u_1} + \mathbf{u_1} \cdot \nabla \mathbf{u_0} + \frac{1}{4\pi\rho_0}[\nabla \mathbf{b_1} \cdot \mathbf{B_0} - \mathbf{B_0} \cdot \nabla \mathbf{b_1} + \nabla \mathbf{B_0} \cdot \mathbf{b_1} - \mathbf{b_1} \cdot \nabla \mathbf{B_0}] + \\ \frac{\rho_1}{\rho_0} \mathbf{u_0} \cdot \nabla \mathbf{u_0} = -\frac{1}{\rho_0} \nabla p_1 \end{aligned} \tag{2.1b}$$

$$\frac{\partial \phi_1}{\partial t} - \mathbf{u_0} \times \mathbf{b_1} - \mathbf{u_1} \times \mathbf{B_0} - \eta \nabla^2 \phi_1 = 0 \tag{2.1c}$$

$$\frac{\partial T_1}{\partial t} + \mathbf{u_0} \cdot \nabla T_1 + (\kappa - 1)(\nabla \cdot \mathbf{u_1}) T_0 + \mathbf{u_1} \cdot \nabla T_0 + (\kappa - 1)(\nabla \cdot \mathbf{u_0}) T_1 = 0. \tag{2.1d}$$

The variables with subscript "0" are the stationary background fields and those with subscript "1" are the perturbed fields which are evolved by the code. $\mathbf{B_0}$ is the background magnetic field and $\mathbf{u}$ is the velocity. ρ, T are density and temperature respectively and $p_1 = \rho_0 T_1 + \rho_1 T_0$ is the perturbed pressure. The adiabatic index $\kappa = 5/3$ and ϕ_1 is the perturbed magnetic flux function from which the perturbed magnetic field $\mathbf{b_1}$ is obtained

$$\mathbf{b_1} = \frac{\partial \phi_1}{\partial y} \hat{e}_x - \frac{\partial \phi_1}{\partial x} \hat{e}_y$$

The simulation domain is a 256×256 rectangular box whose x/y axis is along/across the current sheet. As mentioned in the introduction, the Lundquist number is defined with the half-length of the box L:

$$S = \frac{L V_{Au}}{\eta} \tag{2.2}$$

In our simulations, the length of the box is fixed to be 2 ($-1 \leq x \leq 1$) which means all the lengths are normalized to the half length of the current sheet. As we are studying Sweet-Parker type current sheets, the half width of the current sheet scales with S as:

$$\frac{a}{L} = S^{-\frac{1}{2}} \tag{2.3}$$

so a changes with the Lundquist number in our simulations. As a result, the width of the simulation domain is also changing according to the Lundquist number in order to maintain proper range and resolution in y direction ($\max(|y|) \sim 10a$). Derivatives are calculated using the 6th order Compact Finite Difference (CFD) scheme (Lele, 1992). At the boundaries, projected characteristics are applied to keep the boundaries open (Landi et al., 2005). We use a 4th order Runge-Kutta method to advance in time.

The background velocity and magnetic fields are given by:

$$\mathbf{B_0} = B_0(y)\hat{e}_x \tag{2.4a}$$

$$\mathbf{u_0} = \Gamma x\hat{e}_x - \Gamma y\hat{e}_y \tag{2.4b}$$

where Γ is a constant controlling how fast the outflow is accelerated and the inflow is decelerated. For Sweet-Parker type current sheets, the outflow speed is the upstream Alfvén speed so we have

$$\Gamma = \frac{V_{Au}}{L} = \tau_A^{-1} \tag{2.5}$$

where τ_A is the Alfvén crossing time of the current sheet. The plot of $\mathbf{u_0}$ is shown in the left panel of Figure 2.1. ρ_0 is uniform and set as $1/4\pi$ for non-dimensionalization so that the local Alfvén speed is simply

$$V_A(y) = B_0(y) \tag{2.6}$$

$T_0(x, y)$ is calculated by

$$T_0(x, y) = \bar{T}_0 - \frac{1}{2}(u_{0x}^2 + u_{0y}^2 + B_0^2) \tag{2.7}$$

so that the 0th order momentum equation is satisfied. $\bar{T}_0$ is a constant and set to be 2 in the simulations. Note that self-consistency requires that $\nabla \times (\mathbf{u_0} \cdot \nabla \mathbf{u_0} - \frac{1}{4\pi\rho_0}\mathbf{B_0} \cdot \nabla \mathbf{B_0}) = 0$, which is satisfied by Eq (2.4).

The self-consistent equilibrium magnetic field $B_0(y)$, by solving the 0th-order induction equation, is

$$B_0(y) = \frac{\bar{B}_0}{0.54} \exp[-(\frac{y}{\sqrt{2}a})^2] \int_0^{y/\sqrt{2}a} e^{s^2} ds \tag{2.8}$$

shown as the blue curve in the right panel of Figure 2.1. For this equilibrium, the amplitude of B_0 has a maximum and then decreases toward 0 far from the center of the sheet. In other words, because of the background inflow, the magnetic field is concentrated near the midplane of the current sheet and we use the peak value $\bar{B}_0$ (set as 1) as the characteristic ("upstream") magnetic field in this case. In Section 2.1.3 – 2.1.5, we adopt this equilibrium field for the simulations and the linear stability analysis. In Section 2.1.6, we also show simulation results based on the widely-used Harris current sheet field

$$B_0(y) = \bar{B}_0 \tanh(\frac{y}{a}) \tag{2.9}$$

shown as the orange curve in the right panel of Figure 2.1 where $\bar{B}_0$ (set as 1) is the asymptotic value of B_0. Note that this configuration, in the presence of flows, is not strictly speaking an equilibrium. We consider it mainly for comparison with previous works (e.g. Bulanov et al., 1978).

Note that both L and V_{Au} are fixed to be 1 thus the Lundquist number is determined solely by the resistivity η in the code. Except for the runs shown in Section 2.1.5, we initiate the simulations with white noise, i.e. perturbations of the magnetic flux ϕ_1 uniformly distributed in k space with random phases peaking near the midplane of the current sheet.

2.1.3 Simulation Results

In this section we describe simulation results of the runs with the self-consistent background fields. Figure 2.2 left column shows the evolution of the perturbed magnetic flux function ϕ_1 in the run $S = 10^4$ ($a = 0.01$). From the top to bottom panels, we observe that magnetic

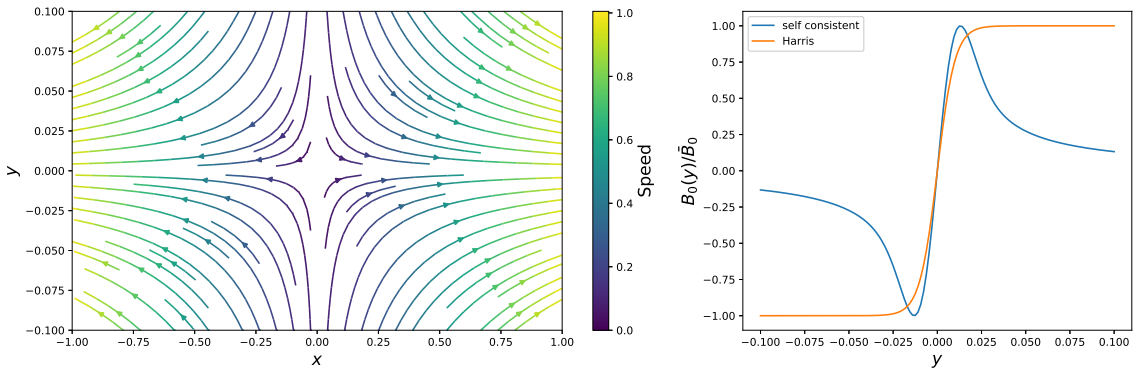

Figure 2.1: The background fields in the simulations with $S = 10^4$. Left: Streamlines of the background flow $\mathbf{u_0}$. Right: Two types of $B_0(y)$ used in the simulations.

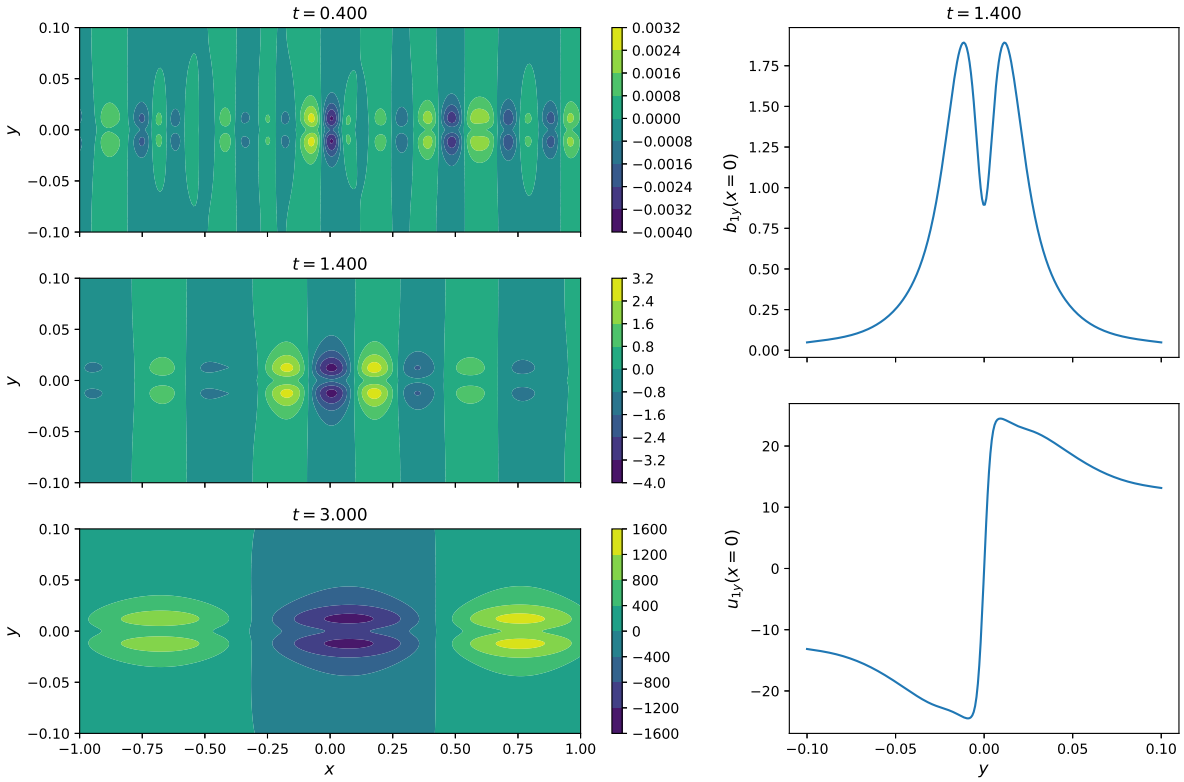

Figure 2.2: Left column: Snapshots of the perturbed magnetic flux function ϕ_1 in the $S = 10^4$ run. Right column: Profiles of b_{1y} and u_{1y} along y-axis at $t = 1.4$.

islands form and grow in amplitude. At the same time, they are stretched along the outflow direction and the islands near the left and right boundaries of the simulation box are ejected out of the domain. The right column of Figure 2.2 shows the profiles of b_{1y} and u_{1y} along the y-axis at $t = 1.4$. As will be shown in Section 2.1.4, these are essentially identical to the eigenfunctions which may be calculated from the linear theory by incorporating the expanding wavelength assumption

$$k(t) = k_0 \exp(-\Gamma t); \tag{2.10}$$

This ansatz was first proposed by Bulanov et al. (1978) to transform the problem into a 1D eigenvalue calculation for each value of k for the tearing mode in a current sheet with a linearly accelerating outflow $u_{0x} = \Gamma x$. Note, however, that in the 2D current sheet, it is impossible to strictly define a purely monochromatic wave because of the lack of periodicity along x. In any case, the 1D assumption takes the stretching effect of the background flow properly into account: imagine two points separated by one wavelength $\lambda(t)$ along the flow

$$x_2(t) = x_1(t) + \lambda(t) \tag{2.11}$$

After time dt, the distance between the two points becomes

$$\begin{aligned} \lambda(t+dt) &= x_2 - x_1 + [u_{0x}(x_2) - u_{0x}(x_1)]dt \\ &= \lambda(t) + \frac{du_{0x}}{dx}\lambda(t)dt \end{aligned} \tag{2.12}$$

which means

$$\frac{1}{\lambda}\frac{d\lambda}{dt} = \frac{du_{0x}}{dx} \tag{2.13}$$

and we easily get Eq (2.10). The result shown in Figure 2.2 is qualitatively consistent with the time-dependent wave number assumption: we will discuss this in more detail in Section 2.1.4.

We calculate the perturbed magnetic and kinetic energies inside the simulation domain

$$E_k = \int \frac{1}{2}(u_{1x}^2 + u_{1y}^2), \quad E_b = \int \frac{1}{2}(b_{1x}^2 + b_{1y}^2) \tag{2.14}$$

as functions of time. These are shown in Figure 2.3: from top-left to bottom-right the panels display runs for $S = 10^4, 10^3, 300$ and 100 respectively. One immediate result from Figure

2.3 is that the growth rate of the energy in the perturbed fields decreases with decreasing Lundquist number. At $S \sim 100$, the perturbed energy starts to decrease with time. Another feature observed in Figure 2.3 is that the energy in the x-component of the fields dominates over the y-component energy. This is very clear for runs $S = 10^4, 10^3$ and 300 where the ratios E_{kx}/E_{ky} and E_{bx}/E_{by} tend to increase with time. This phenomenon can also be explained qualitatively by the stretching effect of the inhomogeneous outflow. Consider the 1st order magnetic field $\mathbf{b_1}$, which must be divergence free:

$$\frac{\partial b_{1x}}{\partial x} + \frac{\partial b_{1y}}{\partial y} = 0 \tag{2.15}$$

If the perturbations are approximated by a mode with a time-dependent wave number (Eq (2.10)), we can estimate

$$\frac{\partial b_{1x}}{\partial x} \sim k_0 b_{1x} \exp(-\Gamma t) \tag{2.16}$$

and

$$\frac{\partial b_{1y}}{\partial y} \sim \frac{b_{1y}}{\delta} \tag{2.17}$$

where δ is the thickness of the inner layer of the tearing mode (Pucci & Velli, 2013) and is approximately constant with time. We then get

$$\frac{b_{1y}}{b_{1x}} \sim (k_0 \delta) \exp(-\Gamma t) \tag{2.18}$$

which means that the growth of b_{1y} is slower than that of b_{1x}. We can apply the same analysis to $\mathbf{u_1}$ assuming that the incompressible modes dominate.

In practice, b_{1y}, as the reconnecting component of the field, is the more interesting quantity. Figure 2.4 shows the growth of b_{1y} in several runs. The upper panel shows the amplitude of b_{1y} as function of time for runs with different S. Here we use the maximum of $|b_{1y}|$ inside the whole simulation domain to represent the amplitude of b_{1y}. For $S < 300$, $|b_{1y}|$ does not grow with time. For the runs with $S > 300$, $|b_{1y}|$ grows after an initial transient phase and then the growth gradually slows down until reaching a maximum. The two dots on each curve mark the start and the end of the growth phase. The saturation time corresponds roughly to the time when most of the magnetic islands are ejected out. We use the ratio

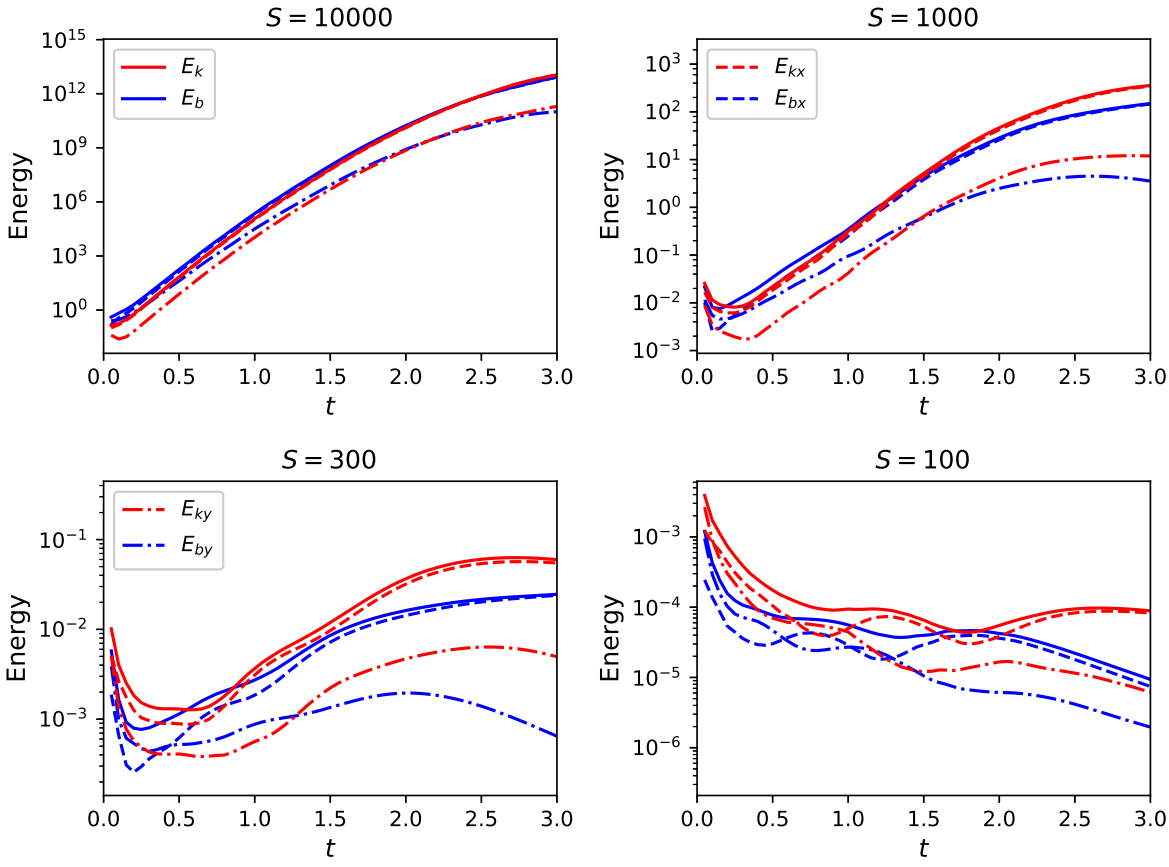

Figure 2.3: Energy of the perturbed velocity and magnetic fields as functions of time for different S. Blue lines are magnetic energy and red lines are kinetic energy. Dashed lines are the energy in x components, dashed-dotted lines are the energy in y components and solid lines are the total energy.

between the amplitudes of b_{1y} at the two points to measure the total growth of $|b_{1y}|$ during a simulation, which is shown as the blue dots in the lower panel of Figure 2.4 as a function of Lundquist number. The orange dots in the same panel are the total growth of b_{1y} estimated through the linear theory which will be discussed in next section. At $S = 1000$, $|b_{1y}|$ grows by a factor of 17 while at $S = 10^4$ it grows by a factor of $\sim 3.5 \times 10^5$. If we somewhat arbitrarily choose the criterion that $|b_{1y}|$ grows by a factor of 10^2 in order to perturb the current sheet strongly, the critical Lundquist number needs to be ~ 2000. Here "strongly perturb the current sheet" means that the amplitude of the perturbation becomes large enough to trigger fast nonlinear evolution (Tenerani et al., 2015, 2016).

2.1.4 Linear Stability Analysis of the 2D Current Sheets

If we use the same background flow as used in the simulations (Eq (2.4b)) and include the expanding effect of the outflow on wavelengths by using a time-dependent wave vector as given by Eq (2.10), assuming that v and b are functions of y only (rigorously they should be functions of both y and t), of the form

$$\begin{pmatrix} u_{1y} \\ b_{1y} \end{pmatrix} = \begin{pmatrix} -iv(y) \\ b(y) \end{pmatrix} \exp\left[ik(t)x + \int_0^t \gamma(k(t'))dt'\right] \tag{2.19}$$

we can reduce Eq (2.1) to a set of ordinary differential equations

$$y(v''' - k^2 v') - (\gamma+1)v'' + (\gamma-1)k^2 v = k\frac{L}{a}[B_0(y)(b'' - k^2 b) - B_0''(y)b] \tag{2.20a}$$

$$(\gamma+1)b - yb' = k\frac{L}{a}B_0(y)v + \frac{1}{S}\frac{L^2}{a^2}(b'' - k^2 b) \tag{2.20b}$$

In deriving Eq (2.20) we have also assumed incompressibility and adopted the following normalizations: length to the half thickness of the current sheet a, magnetic field to the upstream magnetic field $\bar{B}_0$, speed to the upstream Alfvén speed V_{Au}, time to Alfvén time $\tau_A = L/V_{Au}$ where L is the half length of the current sheet. S is defined as LV_{Au}/η and we study Sweet-Parker type current sheets so that $a/L = S^{-1/2}$. Eq (2.20) is a 1D eigenvalue problem with the boundary conditions that v and b vanish at infinity. We numerically solve

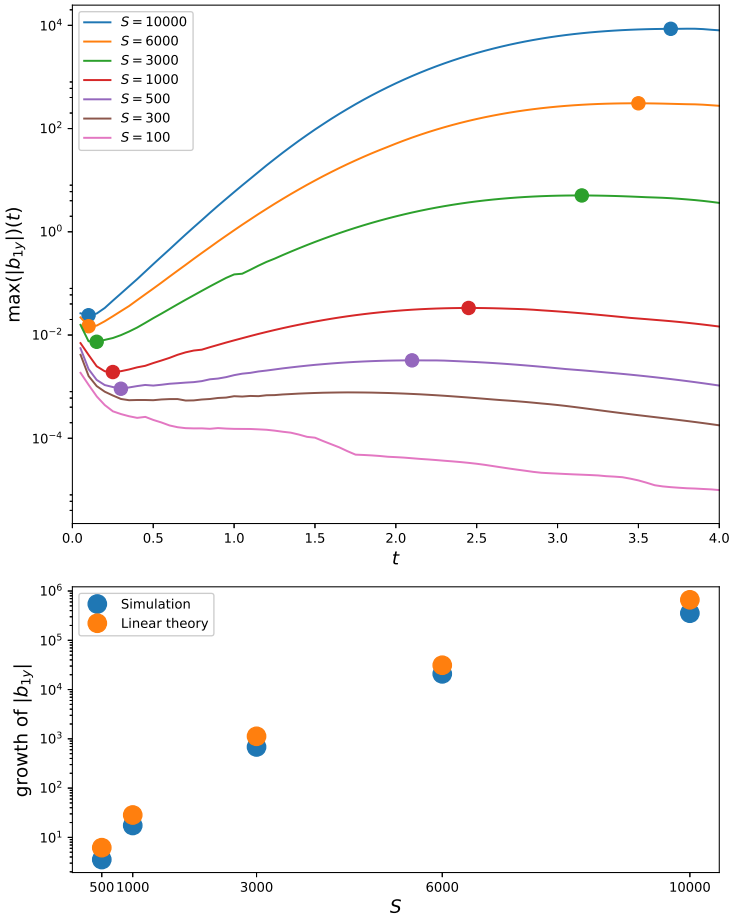

Figure 2.4: Upper panel: Maximum amplitude of b_{1y} in the simulation domain as functions of time for several runs. The two dots on each curve mark the start and the end of the growth phase. Lower panel: Blue dots: growth of $|b_{1y}|$ during the growth phase of the simulations (the ratio between $\max(|b_{1y}|)$ values at the two dots on each curve in the upper panel) as a function of S. Orange dots: growth of $|b_{1y}|$ predicted by the linear theory. See $G(S)$ (Eq (2.26)) and the discussion in Section 2.1.4.

this eigenvalue problem (see Appendix A) and present the result in Figure 2.5. The upper panel of Figure 2.5 is the dispersion relation $\gamma(k)$. The shape of the $\gamma(k)$ curves is similar to that of the dispersion relation of classic tearing mode: there is a fastest growing mode k_f for each Lundquist number and the growth rate decreases for larger or smaller k. Unlike the tearing mode in static current sheets whose growth rate is never negative, now part of the $\gamma(k)$ curve goes below the $\gamma = 0$ line. For $S \lesssim 70$ the whole curve is below $\gamma = 0$ which means that in this configuration of the background fields, the tearing mode does not grow at all for $S \lesssim 70$.

The stabilizing effect of the background flow can be understood by looking at Eq (2.20). In Eq (2.20), the most important term that determines γ is $(\gamma+1)v''$. In the same equation for the tearing mode inside a static current sheet, the term becomes $\gamma v''$. That is to say

$$\gamma \sim \gamma_s - 1 \tag{2.21}$$

where γ is the growth rate with the presence of flow and γ_s is the growth rate without the flow. The difference $1(\Gamma)$ comes from the time-derivative of k in deriving Eq (2.20). This means that in the current sheet with the background flow, stretching of the magnetic islands due to the inhomogeneous outflow slows down their growth. Compared with the equations derived by (Bulanov et al., 1978) (who takes into account only the outflow), Eq (2.20) displays two major differences: (1) the coefficient in front of v'' changes from $\gamma+2$ to $\gamma+1$. (2) y-convection terms appear ($y(v''' - k^2 v'$) and yb'). In Bulanov's equation, the constant $2(\Gamma)$ consists of one Γ which comes from dk/dt (expansion of the wavelength) and another one Γ coming from du_{0x}/dx (expansion of the fluid volume) so their model is even more stable than Eq (2.20). However, when the inflow is included, the du_{0x}/dx is cancelled out by du_{0y}/dy because of incompressibility. In fact, the background configuration considered by (Bulanov et al., 1978) is not self-consistent because their $\mathbf{u_0} = \Gamma x \hat{e}_x$ is compressible while they still assumed a uniform density. The newly-included y-convection terms, especially the term $y(v''' - k^2 v')$, though not important at large S, affects the calculated γ at low S ($\lesssim 10^3$) when $y(v''' - k^2 v')$ becomes comparable to $(\gamma+1)v''$. We also solved Eq (2.20) without the two y-convection terms (not shown here) and it turns out that the growth rate becomes larger,

i.e., the y-convection terms somewhat contribute to the stabilization of the current sheet. But as will be discussed further below, at very low S the linear analysis method becomes invalid so we are unable to evaluate exactly how much stabilization the y-convection brings.

In the middle panel of Figure 2.5 we compare the eigenfunctions calculated through Eq (2.20) with the profiles taken from the simulation for $S = 10^4$. The blue lines are the calculated eigenfunctions at $ka = 0.15$, i.e., the wavelength $\lambda \approx 0.4$ and the orange lines are u_{1y} and b_{1y} along the y axis taken from the $S = 10^4$ run at $t = 1.4$ (right column of Figure 2.2) when the wavelength of the dominant mode is ≈ 0.4. The amplitudes of the eigenfunctions and the cuts from the simulation are adjusted to be the same. We can see that the shapes of the eigenfunctions by the linear theory are very close to the profiles taken from the linear simulation, confirming the validity of the linear theory in this case.

Based on the linear theory, we are able to explain the saturation phenomenon observed in Figure 2.4. For a mode with wave number $k(t)$ at time t, the instantaneous growth rate is $\gamma(k(t))$. As time increases, $k(t)$ decreases and thus the instantaneous growth rate moves along the $\gamma - k$ curve toward left. After $k(t)$ passes the fastest-growing wave number k_f, the growth rate starts to decrease and eventually goes to 0 (even below 0). To verify this theory, we first estimate the dominant mode, i.e. the mode whose amplitude is the largest, at a certain time and compare it with the simulation result. We assume that the initial perturbations are uniformly distributed in k-space. At time t, the wave number $k = k(t)$ corresponds to the initial wave number $k_0 = k(t)e^t$ (in our normalization $\Gamma = 1$). At any time $0 \le t' \le t$ this mode corresponds to

$$k' = k_0 e^{-t'} = k(t)e^{t-t'} \tag{2.22}$$

and the instantaneous growth rate at t' is

$$\gamma' = \gamma(k') = \gamma[k(t)e^{t-t'}] \tag{2.23}$$

In order to get the amplitude of the mode $k(t)$, we integrate along the $\gamma - k$ curve from k_0 to $k(t)$:

$$|b_{1y}|(t, k(t)) = \exp\Big[\int_0^t \gamma(k\, e^{t-t'})dt'\Big] \tag{2.24}$$

and then we are able to find the wavenumber $k_d(t)$ whose amplitude is the largest. In the left panel of Figure 2.6, the orange curve shows the estimated dominant wave number through Eq (2.24) for $S = 10^4$ and the blue dots show the dominant wave number calculated from the simulation $S = 10^4$. In analyzing the simulation result, we first cut $b_{1y}(x, y, t)$ along x axis, i.e. the midplane of the current sheet, and then multiply it by a Tukey window to remove the effect of non-periodicity along x before we apply Fourier transform to it. The steps in the blue dots are due to the resolution in k space when we do Fourier transform. We shift the orange curve by $\Delta t = 0.1$ because of the initial transient phase in the simulation. We see that the curve and the dots almost overlap for $t \gtrsim 1.0$. The large difference between them for $t \lesssim 0.5$ may be a result of the initial transient phase in the simulation. As we have the amplitude of b_{1y} as a function of time from the simulation, we are able to calculate the instantaneous growth rate at a given time by

$$\gamma(t) = \frac{1}{|b_{1y}|}\frac{d|b_{1y}|}{dt} \tag{2.25}$$

and then relate it with the calculated dominant wave number at the same time to get a $\gamma - k$ curve, which is shown in the right panel of Figure 2.6. Again the blue dots are the simulation result and the orange curve is the dispersion relation given by the linear theory (the curve taken from Figure 2.5). The theory and the simulations agree with each other very well, verifying the physical picture that γ moves along the $\gamma - k$ curve.

We estimate the total growth of $|b_{1y}|$ using the dispersion relation shown in Figure 2.5 by doing the integral along the $\gamma - k$ curves:

$$G(S) = \exp\left[\int_0^{t_c} \gamma(k_0 e^{-t'}|S)dt'\right] \tag{2.26}$$

where $t = 0$ is at the right zero point of the $\gamma - k$ curve and t_c is when $k_0 \exp(-t_c) = \pi/L$, i.e., when the wavelength reaches the length of the current sheet (generally very close to the left zero point of the curve). Note that Eq (2.26) is actually an estimate of the upper limit of the total growth of $|b_{1y}|$ because we integrate through the whole positive part of each $\gamma - k$ curve, thus the estimate is larger than the real growth. The calculated $G(S)$ is shown as the orange dots in the lower panel of Figure 2.4. We can see that it is in accordance with

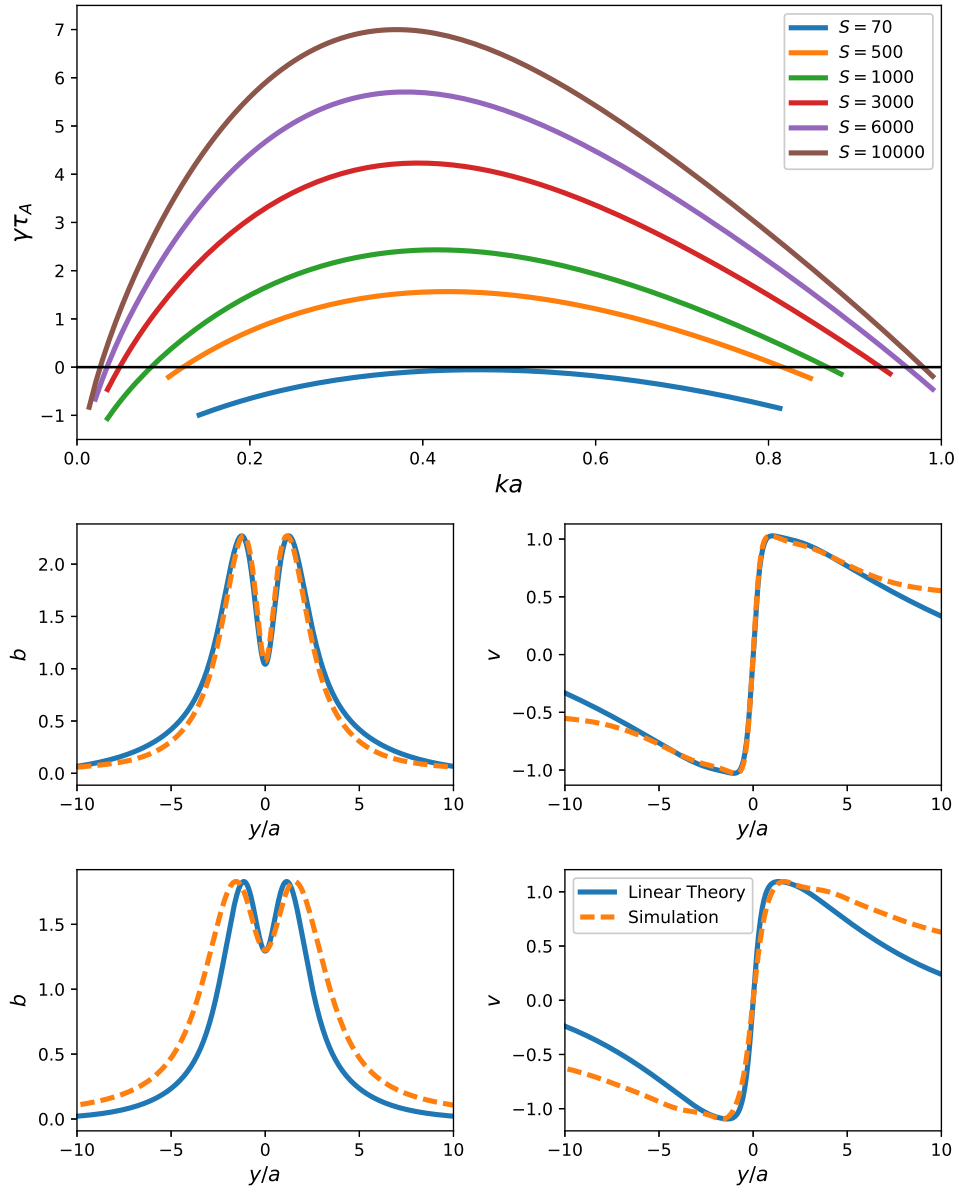

Figure 2.5: Linear stability analysis based on Eq (2.20). Upper panel: Dispersion relation $\gamma - k$ for different S. Middle panel: Blue solid line: eigenfunctions calculated through linear analysis for $S = 10^4$ and $ka = 0.15$. Orange dashed line: profiles of u_{1y} and b_{1y} taken from the simulation when $ka \approx 0.15$ (right column of Figure 2.2, $t = 1.4$). The amplitudes of the linear result and the simulation result are adjusted to be the same. Lower panel: same as middle panel but $S = 500$ and $ka = 0.20$ ($t \approx 1.4$ in the simulation).

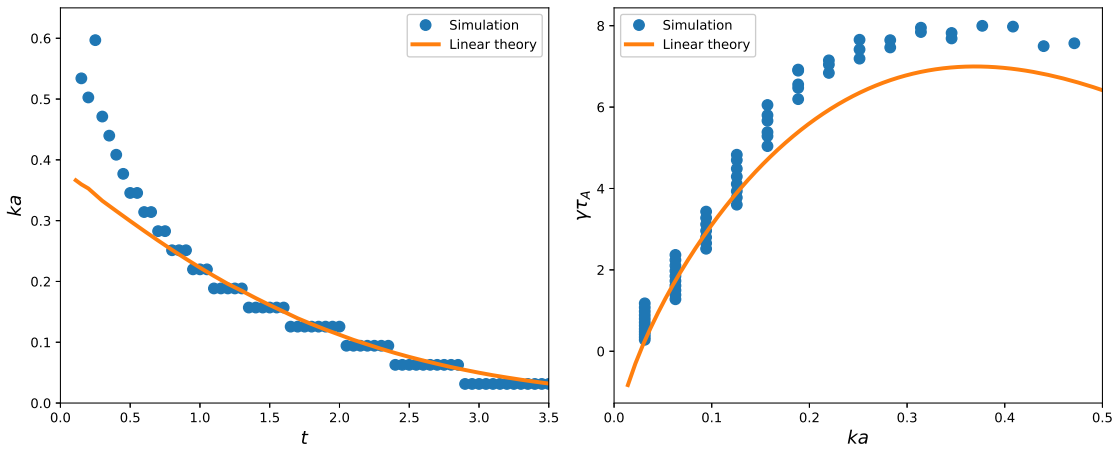

Figure 2.6: Left panel: Dominant wave number as a function of time. Blue dots are calculated from the simulation $S = 10^4$ and the orange curve is the estimate through the linear theory. The steps in the blue dots are due to the finite resolution in k when we apply Fourier transform. The orange curve is shifted in time by $\Delta t = 0.1$ because the simulation has an initial transient phase whose duration is ~ 0.1. Right panel: Dispersion relation $\gamma - k$. Blue dots are calculated from the simulation and the orange curve is the linear theory.

the simulation though a little bit larger and in general the theory result and the simulation result differ by a factor of smaller than 2.

Although the linear stability analysis based on the $k = k_0 \exp(-\Gamma t)$ assumption works quite well for $S \gtrsim 10^3$, we must point out that, for small Lundquist numbers, this assumption becomes invalid because of the small growth rate ($\gamma \lesssim \tau_A^{-1}$), i.e., when the growth time scale for a magnetic island becomes larger than the time scale for it to be ejected out of the current sheet. Actually, when $\gamma < \Gamma(= \tau_A^{-1})$, we cannot assume that the functions v and b in Eq (2.20) are independent of time anymore. Note that in Eq (2.20) k is a function of time so mathematically the assumption Eq (2.19) is not rigorous. Stated otherwise, we are unable to pose a 1D eigenvalue problem for a 2D Sweet-Parker type current sheet at very small Lundquist numbers. In the lower panel of Figure 2.5, we compare the simulation result with the eigenfunctions for $S = 500$ and $ka = 0.20$. Clearly the simulation result deviates from the eigenfunctions. There is no doubt that as S becomes smaller the difference between the simulation and the approximate 1D linear theory will become larger. The linear theory predicts a threshold $S_c \approx 70$ below which b_{1y} does not grow while from the upper panel of Figure 2.4 we see that the threshold is at least ≈ 300.

2.1.5 The Effect of the Initial Perturbation

In this section we discuss the stability of the current sheet in terms of initial conditions, i.e. in terms of the initial perturbation. Our simulation is linear so that the amplitude of the initial noise is arbitrary. In Section 2.1.3 we chose the criterion for an unstable current sheet to be that $|b_{1y}|$ grows by a factor of 10^2 which gives a critical Lundquist number ~ 2000. However, that is not a universal criterion, because depending on the initial state, we must allow $|b_{1y}|$ to grow sufficiently that the sheet is strongly affected, i.e. nonlinear evolution is triggered, at times comparable to their evacuation from the domain.

Because the configuration of the current sheet in this study is fully 2D and the simulation is open-boundary, it is natural to propose that the shape of the initial perturbation also affects the stability. To be more specific, where the initial perturbation is excited on the

current sheet is important because the generation location of a magnetic island determines how long the island grows before it is ejected out of the current sheet. Here the location refers to the distance to $x = 0$, i.e. the location along the outflow. Based on the $S = 10^4$ run, we carried out three more runs with identical background configuration but for each run we modulate the initial perturbation by multiplying it with a gaussian function:

$$f(x|x_c) = \frac{1}{2}\big[\exp(-\frac{(x-x_c)^2}{2\sigma^2}) + \exp(-\frac{(x+x_c)^2}{2\sigma^2})\big] \tag{2.27}$$

where $x_c = 0.0$, 0.4 or 0.8 and $\sigma = 0.1$. The 3 modulation functions are plotted in the left panel of Figure 2.7. Through the modulation functions we are able to localize the initial perturbation around $\pm x_c$. We calculate the amplitudes b_{1y} as functions of time for each of the three runs and present the results in the right panel of Figure 2.7. The red dashed line shows the result of the original run without modulation, i.e. the $S = 10^4$ curve in the upper panel of Figure 2.4. We see that the curve of the $x_c = 0.0$ run almost overlaps with the original run, indicating that in the simulation where the initial perturbation is uniformly distributed along the current sheet, the dominant magnetic islands are those generated near the center of the current sheet, as clearly seen in the left column of Figure 2.2. In the $x_c = 0.4$ run, the growth rate of $|b_{1y}|$ is almost the same as the $x_c = 0.0$ run at short times ($t \lesssim 1.0$) but later the growth rapidly stops. As a result, the total growth of $|b_{1y}|$ in this run is a factor of $\sim 1.5 \times 10^3$ rather than the factor 3.5×10^5 of the $x_c = 0.0$ run. For $x_c = 0.8$, there is nearly no growth phase for $|b_{1y}|$. These results agree with the idea that the evacuation time of the magnetic island is a key factor in determining how much the island can grow. Assuming that a magnetic island is generated at $x = x_c$, we can estimate the evacuation time of the magnetic island

$$\begin{aligned} \tau_e(x_c) &= \int_{x_c}^{1} \frac{dx}{u_{0x}(x)} = \int_{x_c}^{1} \frac{dx}{x} \\ &= \ln(\frac{1}{x_c}) \end{aligned} \tag{2.28}$$

We then get $\tau_e(0.4) = 0.92$ and $\tau_e(0.8) = 0.22$ which agree with the simulation results.

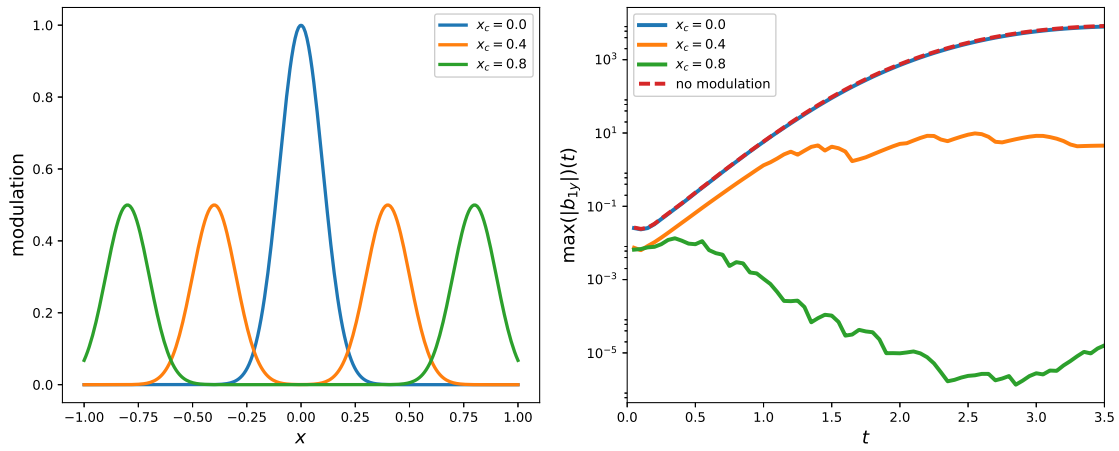

Figure 2.7: Left: Modulation functions multiplied to the initial perturbations in the three runs with the identical configurations as the run $S = 10^4$ shown in Figure 2.2. Right: Amplitudes of b_{1y} as functions of time in the three runs with the modulation functions shown in the left panel. The red dashed line is the original run without modulation, i.e. the $S = 10^4$ curve in the upper panel of Figure 2.4.

2.1.6 Simulation Results with the Harris Current Sheet Model

We carry out the same simulations as those in Section 2.1.3 but change B_0 to the Harris current sheet field (Eq (2.9)) and present the results in Figure 2.8 and 2.9. We also carry out the simplified 1D linear stability analysis with the Harris current sheet field, shown in Figure 2.10 where the dashed line is the result for a static Harris current sheet and is plotted to show the stabilizing effect of the background flow (see Eq (2.21) and the discussion in Section 2.1.4). Note that we are still assuming the background fields are stationary though technically speaking the velocity field Eq (2.4b) and the Harris magnetic field Eq (2.9) do not satisfy the induction equation. Indeed the 0th order fields should vary with time and their evolution will hence affect the evolution of the 1st order quantities. In this section, however, we ignore the non-self-consistency of the background fields to illustrate the dependence of the current sheet stability on different background magnetic fields. In reality, this implies that our results are physically significant only for growth rates large enough ($\gamma\tau_A > 1$) where the evolution of the background fields is negeligible.

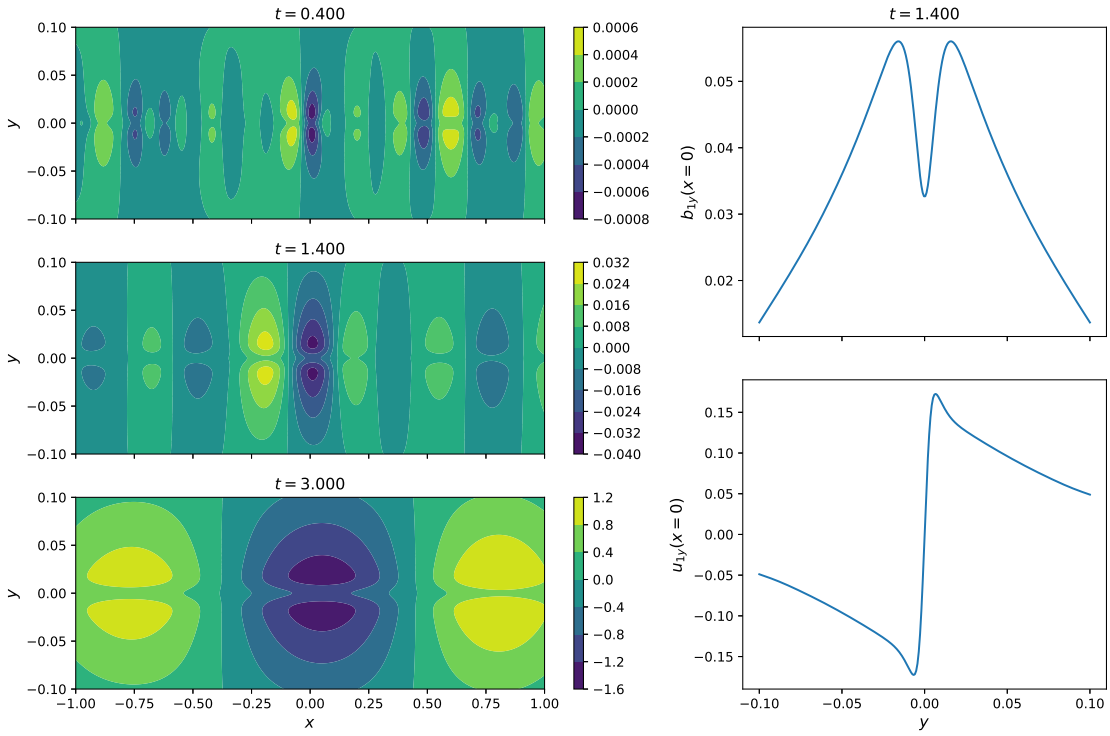

Figure 2.8: Left column: Snapshots of the perturbed magnetic flux function ϕ_1 in the $S = 10^4$ run with a Harris current sheet field. Right column: Profiles of b_{1y} and u_{1y} along y-axis at $t = 1.4$.

Compared with the self-consistent B_0 case, the growth rate with $B_0(y) = \bar{B}_0 \tanh(y/a)$ is smaller. By comparing Figure 2.8 with Figure 2.2, we see that the magnetic islands are much thinner with the self-consistent field because of the more concentrated B_0 and that is why the growth rate with the self-consistent B_0 is larger. The growth of $|b_{1y}|$ is also much smaller than before: at $S = 1000$, $|b_{1y}|$ grows by a factor of 1.9 (17 for self-consistent field) while at $S = 10^4$ it grows by a factor of 400 (3.5×10^5 for self-consistent field). If we adopt the same criterion for an unstable current sheet as in Section 2.1.3 that $|b_{1y}|$ grows by a factor of 10^2, the critical Lundquist number is at least ~ 6000 (2000 for self-consistent field). Despite of the quantitative differences, the qualitative properties we discuss in Section 2.1.3, 2.1.4 and 2.1.5, i.e. the expanding wavelength and the finite growth time effect, are also applicable here.

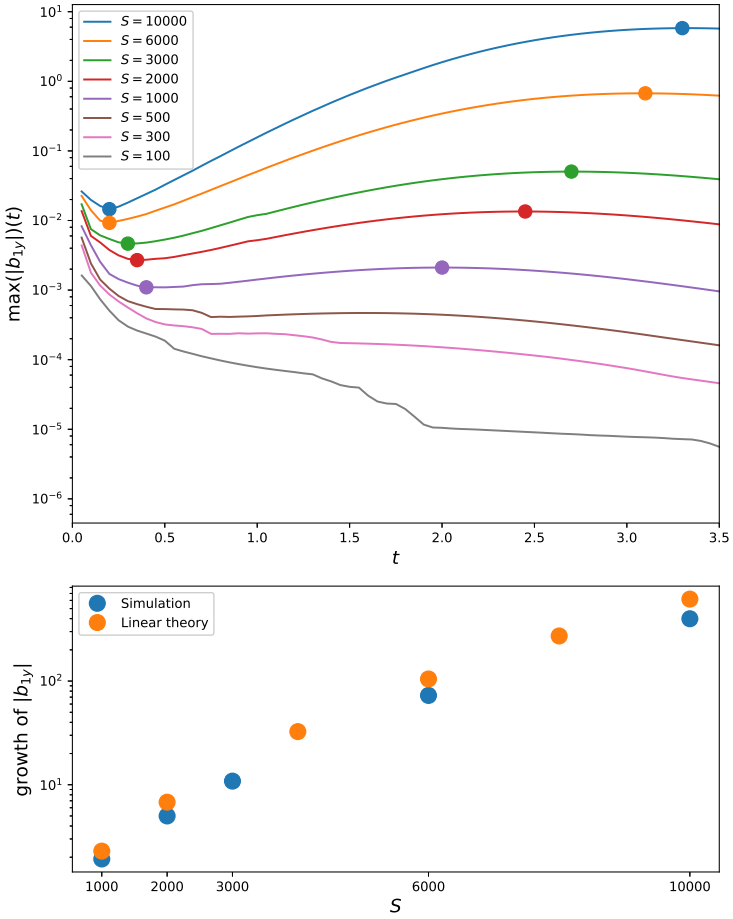

Figure 2.9: Same as Figure 2.4 except for the use of the Harris current sheet field.

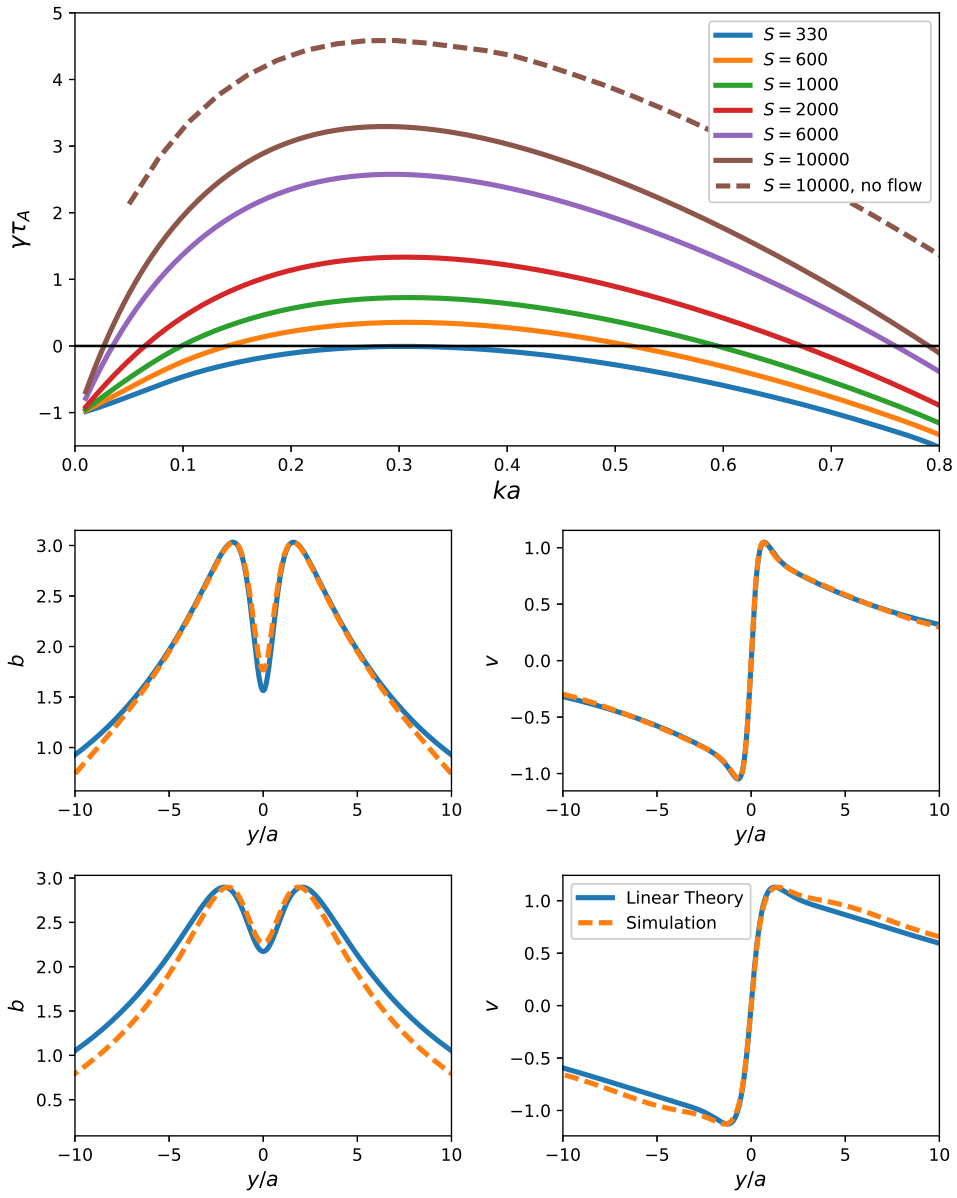

Figure 2.10: Linear stability analysis based on Eq (2.20) and $B_0 = \tanh(y/a)$. Upper panel: Dispersion relation $\gamma - k$ for different S. Middle panel: Blue solid line: eigenfunctions calculated through linear analysis for $S = 10^4$ and $ka = 0.15$. Orange dashed line: profiles of u_{1y} and b_{1y} taken from the simulation when $ka \approx 0.15$ (right column of Figure 2.8, $t = 1.4$). The amplitudes of the linear result and the simulation result are adjusted to be the same. Lower panel: same as middle panel but $S = 500$ and $ka = 0.20$ ($t \approx 1.4$ in the simulation).

2.1.7 Summary

In this study, we have explored the tearing instability inside 2D Sweet-Parker type current sheets at low Lundquist numbers using both 2D linear open-boundary MHD simulations and a simplified 1D linear stability analysis. We find that in the linear stability analysis, the assumption of a time-dependent wave number $k = k_0 e^{-\Gamma t}$ proposed by (Bulanov et al., 1978) works quite well for $S \gtrsim 10^3$. As predicted by the linear theory, the simulations show that the inhomogeneous background outflow stretches the growing magnetic islands and the stretching slows down the island growth. On the other hand, because of the finite size of the current sheet, the magnetic islands are evacuated out of the current sheet within a finite time (several Alfvén times) and thus they cannot grow infinitely (as would happen in a periodic current sheet). In the simulations initialized with white noise we clearly observe a saturation phase after the growing phase, corresponding to the time when most of the magnetic islands are ejected out. As a consequence, the excitation location of the initial perturbation is an important factor in determining how much perturbations can grow.

We estimate through the simulations the critical Lundquist number above which the current sheet can be viewed as "strongly perturbed". The result is dependent on the shape of the background magnetic field $B_0(y)$ we use. Generally, the Harris current sheet field is more stable than the self-consistent background field (Eq (2.8)). Based on the criterion that $|b_{1y}|$ grows by a factor 10^2 during the growth phase, the Lundquist number threshold can be ~ 2000 or ~ 6000 depending on which $B_0(y)$ is used. We may say that under this specific criterion the threshold S_c is several thousands. However, no universal criterion which is independent of context can be defined, since amplitude and localization of fluctuations in the initial current are fundamental to the subsequent evolution.

We find that the flow structure of the SP sheet adequately accounts for the low S stabilization without the need of other factors, such as proposed by (Loureiro et al., 2013). Their suggested instability threshold, given by

$$\frac{\delta}{a} = f \tag{2.29}$$

where δ is the thickness of the inner layer, a is the thickness of the current sheet, and $f \simeq 1/3$ is a constant, yields a critical S compatible with findings of some simulations. On the other hand, the scaling of the stabilization criterion with current sheet aspect ratio appears to go in the wrong direction. Indeed, consider a current sheet whose aspect ratio is

$$\frac{a}{L} \sim S^{-\alpha}. \tag{2.30}$$

The asymptotic scaling of δ then becomes (see e.g. (Tenerani et al., 2016))

$$\frac{\delta}{a} \sim S^{-\frac{1}{4}(1-\alpha)} \tag{2.31}$$

and the threshold Lundquist number S_c from the criterion above would become

$$S_c = (\frac{1}{f})^{\frac{4}{1-\alpha}} \tag{2.32}$$

For a Sweet-Parker type current sheet ($\alpha = 1/2$) and $f = 1/3$, Eq (2.32) gives $S_c \approx 6.5 \times 10^3$, close to 10^4. However, S_c given by Eq (2.32) is an increasing function of α, which means that the thinner a current sheet the more stable it would be, contrary to all numerical and physical intuition. The point is that at low Lundquist number ($< 10^4$) asymptotic scalings really do not work in the first place. On the other hand, we have demonstrated that velocity fields indeed provide the right criteria for stability.

In terms of astrophysical structures, such as for example coronal magnetic fields or prominence eruptions, fluctuations are always present, propagating from other coronal regions or from the photosphere. As shown by Tenerani et al. (2016), at very high Lundquist numbers 2D current sheets tend to disrupt in a quasi self-similar way, in which case flurrys of smaller scale current sheets are generated iteratively. At each step, the Lundquist number decreases, and finally they will cross the critical S at which further disruption is quenched. However, at those scales where S becomes small enough, kinetic effects, explored in (Pucci et al., 2017), become fundamental. We will address this question in the following section.

2.2 Fast Recursive Reconnection and the Hall effect: Hall-MHD simulations

2.2.1 Introduction

In Section 2.1 we discussed the stabilizing effect of the inhomogeneous background flow inside a current sheet. This effect may serve as a mechanism that stops the recursive reconnection process in which the Lundquist number of the high order current sheets decreases gradually (see Tenerani et al., 2015). However, as the recursive reconnection proceeds, it is possible that the thickness of the microscopic current sheets approaches the ion inertial length d_i well before the Lundquist number reaches the threshold S_c required for stabilization so that kinetic effect becomes important before the current sheets are stabilized. It has been shown by collisional-PIC and Hall-MHD simulations that when the thickness of a current sheet approaches the ion inertial length, the reconnection rate is enhanced significantly due to the Hall effect (Daughton et al., 2009; Shepherd & Cassak, 2010). Here we carry out a series of Hall-MHD simulations to investigate how recursive reconnection is altered once the Hall term takes effect. We show that, as d_i increases from values smaller to greater than the tearing mode inner, or singular, layer thickness, reconnection transitions from a plasmoid-generating dominant pattern to a Hall-dominant pattern. We also show that, during the nonlinear stage, the structure around the X-point, the reconnection rate, the energy dissipation and the power spectra of various quantities are all significantly modified by the Hall effect.

This section is organized as follows: In Section 2.2.2 we describe the numerical setup of the simulations, including the numerical model and the choice of parameters. In Section 2.2.3 we show the simulation results and in Section 2.2.4 we summarize this work.

2.2.2 Numerical Setup

The code we use is a 2.5D Hall-MHD code based on the following equation set:

$$\frac{\partial \rho}{\partial t} = -\mathbf{u}\cdot\nabla\rho - (\nabla\cdot\mathbf{u})\rho \tag{2.33a}$$

$$\frac{\partial \mathbf{u}}{\partial t} = -\mathbf{u}\cdot\nabla\mathbf{u} - \frac{1}{\rho}\nabla p + \frac{1}{\rho}\mathbf{j}\times\mathbf{B} \tag{2.33b}$$

$$\frac{\partial \psi}{\partial t} = \left(\mathbf{u}\times\mathbf{B} - \frac{d_i}{\rho}\mathbf{j}\times\mathbf{B}\right)_z + \eta\nabla^2\psi \tag{2.33c}$$

$$\frac{\partial B_z}{\partial t} = \left[\nabla\times\left(\mathbf{u}\times\mathbf{B} - \frac{d_i}{\rho}\mathbf{j}\times\mathbf{B}\right)\right]_z + \eta\nabla^2 B_z \tag{2.33d}$$

$$\frac{\partial p}{\partial t} = -\mathbf{u}\cdot\nabla p - \kappa(\nabla\cdot\mathbf{u})p \tag{2.33e}$$

where $\mathbf{j} = \nabla\times\mathbf{B}$ is the current density and ψ is the z component (the out-of-plane component) of the magnetic vector potential such that

$$B_x = \frac{\partial\psi}{\partial y}, \quad B_y = -\frac{\partial\psi}{\partial x} \tag{2.34}$$

and $\nabla\cdot\mathbf{B} = 0$ is conserved automatically. $\kappa = 5/3$ is the adiabatic index. The code is double-periodic and derivatives are calculated by spectral method. Explicit 3rd order Runge-Kutta method is used for time integral and Courant-Friedrichs-Lew condition determines the time step.

The initial condition is a pressure-balanced Harris current sheet:

$$\mathbf{B_0} = B_0\tanh(\frac{y-y_c}{a_0})\hat{e}_x \tag{2.35a}$$

$$\rho_0 = \rho_\infty + \frac{B_0^2}{2T_0}\mathrm{sech}^2(\frac{y-y_c}{a_0}) \tag{2.35b}$$

where the asymptotic density ρ_∞, the temperature T_0 and the asymptotic magnetic field B_0 are constants:

$$\rho_\infty = 1, \quad T_0 = 1, \quad B_0 = 1 \tag{2.36}$$

a_0 is the thickness of the initial current sheet and is set to be

$$a_0 = 0.02 \tag{2.37}$$

The domain size is $L_x \times L_y = 8 \times 0.8$ and because of the periodicity along y, a double Harris current is used so in practice $L_y = 0.4$. The grid points are distributed uniformly with total number $n_x \times n_y = 4096 \times 2048$, i.e. the resolution is $\Delta x = 1.95 \times 10^{-3}$, $\Delta y = 3.91 \times 10^{-4}$. Random noise on modes $N = 1 - 128$ (i.e. $\mathbf{k_N} = \frac{N}{L_x}\hat{e}_x$) is added to the center of the initial current sheet. Note that "random" here means that the phase of each mode is generated randomly but for all the simulations in this work the initial perturbations are exactly the same. The resistivity is $\eta = 1 \times 10^{-5}$, i.e. the Lundquist number $S = 10^5$.

7 runs are carried out with the ion inertial length d_i to be the only varying parameter:

$$d_i = [0, 1, 2, 3, 4, 5, 10] \times 10^{-3} \tag{2.38}$$

and we will refer to them as Run 0-5 and Run 10 for convenience hereinafter. Note that, the critical thickness of the current sheet to trigger the "ideal tearing" is estimated to be

$$a \sim S^{-1/3} = 0.0215 \tag{2.39}$$

and the inner layer thickness of the tearing mode is estimated to be

$$\delta \sim S^{-1/2} = 3.16 \times 10^{-3} \tag{2.40}$$

Eqs. (2.39 & 2.40) help guide the choice of a_0 and d_i: $a_0 = 0.02$ allows ideal tearing to be triggered and as d_i varies from values below to above δ we expect to observe the transition from a plasmoid dominated regime to the Hall regime when an inner layer is formed with a thickness on the order of d_i. Run 10 is an extreme case where d_i is on the scale of a_0 for comparison.

2.2.3 Results

2.2.3.1 Time Evolution and Structure of the Current Sheet

The left and middle columns of Figure 2.11 show the out-of-plane current density in Run 0, i.e. the MHD case. Left column shows the time evolution of J_z inside the domain $x \in [2.0, 3.0]$ and $y \in [0.15, 0.25]$ where one X-point appears but note that there are multiple

X-points formed along the current sheet. The evolution is similar to what is observed in the simulations by Tenerani et al. (2015). The initial perturbation grows into a sequence of X-points which evolve nonlinearly into secondary current sheets stretched along the outflow direction ($t = 3.2$ and $t = 5.6$). During the dynamic lengthening, the thickness of the secondary current sheet is observed to be nearly constant and is $a_1 \approx 0.002$, close to the predicted inner layer thickness of the tearing mode. At time $t = 5.6$, secondary tearing is triggered after which the secondary current sheet breaks into a series of small current sheets and plasmoids ($t = 6.4$). This process continues recursively until the end of the simulation at $t = 9$. The middle column of Figure 2.11 shows the hierarchic structure of J_z at $t = 7.20$. Top panel is the whole simulation domain. Middle and bottom panels are blow-ups as marked by the boxes and arrows. It is clearly seen from the bottom panel that at $x \approx 2.70$ a tiny plasmoid is being generated out of a micro current sheet whose thickness is on grid scale: $a_n \approx \Delta y < 0.001$. The right column shows the time-averaged power spectra in this run and will be discussed in Section 2.2.3.3.

Figure 2.12 is the similar plot with Figure 2.11 for Run 1, i.e. $d_i = 0.001$. The evolution is similar with Run 0 at $t \leq 5$: a secondary current sheet is formed and stretched along x direction with thickness $a_1 \approx 0.0016$. Then the secondary current sheet breaks into small plasmoids at $t \approx 5$, earlier than Run 0 as expected: tearing instability has larger growth rate with Hall term (Pucci et al., 2017). Very soon after the break up of the secondary current sheet, a single X-point configuration, which is a typical structure of Hall-reconnection, is formed (between $t = 5.2$ and $t = 5.6$). But instead of a steady X-point structure, plasmoids are consecutively generated at the X-point. The bottom-left panel and the middle column of Figure 2.12 clearly show a chain of wedges on each side of the X-point at $t = 7.2$ and these wedges are the ejected plasmoids. As shown in the bottom panel of the middle column, there is one plasmoid being generated and ejected toward the left at $x \approx 2.52$. Figure 2.13 and Figure 2.14 are plots similar to those shown in Figure 2.11 but for Run 2 and Run 5, respectively. As d_i increases, the Hall-reconnection stage is triggered earlier and the plasmoid generation is suppressed. In Run 2 we can still see generation of plasmoids (see the second

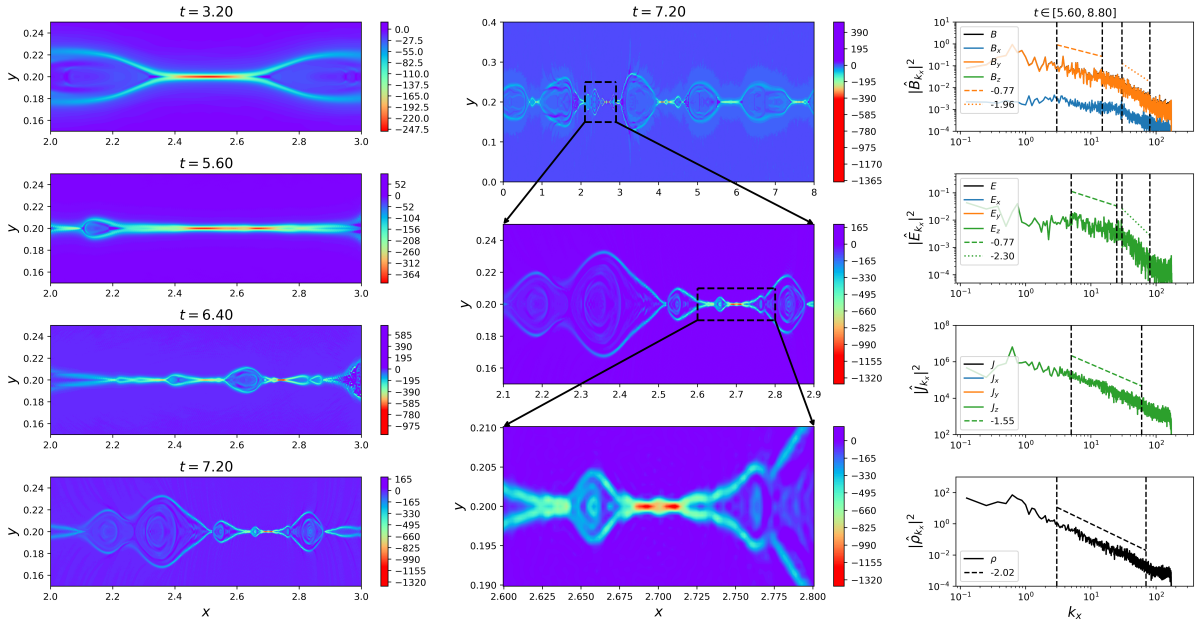

Figure 2.11: Out-of-plane current density J_z and the power spectra in Run 0. Left column: time evolution of J_z inside the domain $x \in [2.0, 3.0]$ and $y \in [0.15, 0.25]$. Middle column: the hierarchic structure of the current sheet (color is J_z) at $t = 7.20$. Top panel is the whole simulation domain. Middle and bottom panels are blow-ups as marked by the boxes and arrows. Right column: time-averaged power spectra of the magnetic field $\mathbf{B}$, the electric field $\mathbf{E}$, the current density $\mathbf{J}$ and the density ρ calculated at the central line of the current sheet $y = 0.2$ in log-log scale. The blue, orange and green lines represent the x, y and z components of the vector fields respectively and the black lines are the sum of the 3 components in the first three panels. The dashed and dotted lines are linear fits for the spectra of B_y, E_z, J_z and ρ. The k_x ranges for the fits are marked by the vertical dashed lines and the slopes of the fits are written in the legends. The time period for averaging the spectra is written at the top of the column.

panel on the left column and the bottom panel on the middle column of Figure 2.13) while for Run 5 there is no plasmoid observed.

By comparing the middle-bottom panels of Figure 2.12-2.14, which show the simulation domains of the same size (0.2×0.02), we observe that the opening angle of the exhaust

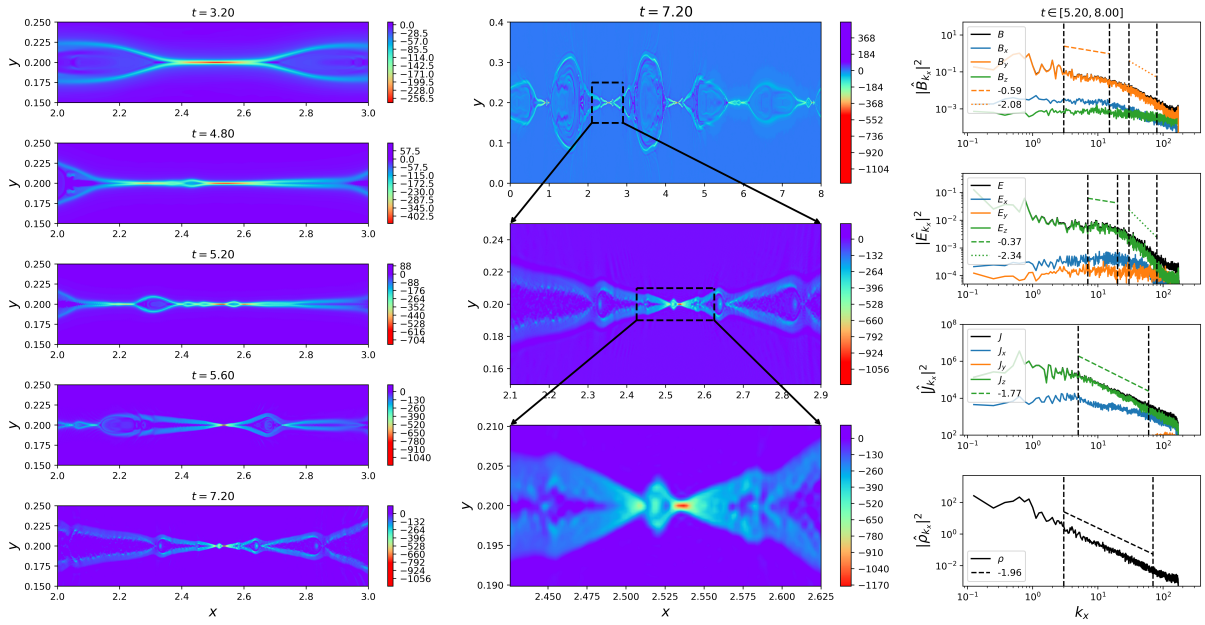

Figure 2.12: Out-of-plane current density J_z and the power spectra in Run 1. Left column: time evolution of J_z inside the domain $x \in [2.0, 3.0]$ and $y \in [0.15, 0.25]$. Middle column: the hierarchic structure of the current sheet (color is J_z) at $t = 7.20$. Top panel is the whole simulation domain. Middle and bottom panels are blow-ups as marked by the boxes and arrows. Right column: time-averaged power spectra of the magnetic field $\mathbf{B}$, the electric field $\mathbf{E}$, the current density $\mathbf{J}$ and the density ρ calculated at the central line of the current sheet $y = 0.2$ in log-log scale. The blue, orange and green lines represent the x, y and z components of the vector fields respectively and the black lines are the sum of the 3 components in the first three panels. The dashed and dotted lines are linear fits for the spectra of B_y, E_z, J_z and ρ. The k_x ranges for the fits are marked by the vertical dashed lines and the slopes of the fits are written in the legends. The time period for averaging the spectra is written at the top of the column.

increases and the size of the X-point shrinks as d_i enlarges. In Figure 2.15, we show the opening angle of the exhaust and the half length of the current sheet at the X-point as functions of d_i. The two quantities are calculated for each of Run 1-5 and for Run 10, when the X-point structure is steady. The opening angle increases almost linearly with d_i from

about 10 degrees for $d_i = 0.001$ to about 28 degrees for $d_i = 0.01$. The half-length of the current sheet decreases with d_i quite fast for $d_i \leq 0.003$ and then begins to converge, possibly because the resolution $\Delta x \approx 0.002$ is approached.

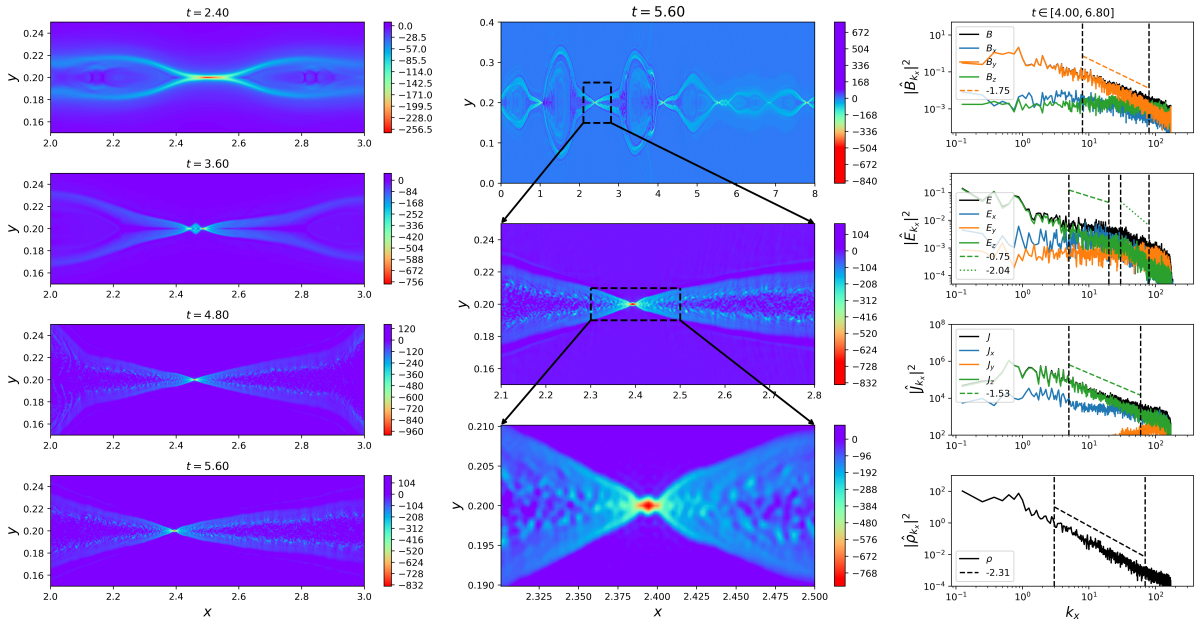

Figure 2.13: Out-of-plane current density J_z and the power spectra in Run 2. Left column: time evolution of J_z inside the domain $x \in [2.0, 3.0]$ and $y \in [0.15, 0.25]$. Middle column: the hierarchic structure of the current sheet (color is J_z) at $t = 5.60$. Top panel is the whole simulation domain. Middle and bottom panels are blow-ups as marked by the boxes and arrows. Right column: time-averaged power spectra of the magnetic field $\mathbf{B}$, the electric field $\mathbf{E}$, the current density $\mathbf{J}$ and the density ρ calculated at the central line of the current sheet $y = 0.2$ in log-log scale. The blue, orange and green lines represent the x, y and z components of the vector fields respectively and the black lines are the sum of the 3 components in the first three panels. The dashed and dotted lines are linear fits for the spectra of B_y, E_z, J_z and ρ. The k_x ranges for the fits are marked by the vertical dashed lines and the slopes of the fits are written in the legends. The time period for averaging the spectra is written at the top of the column.

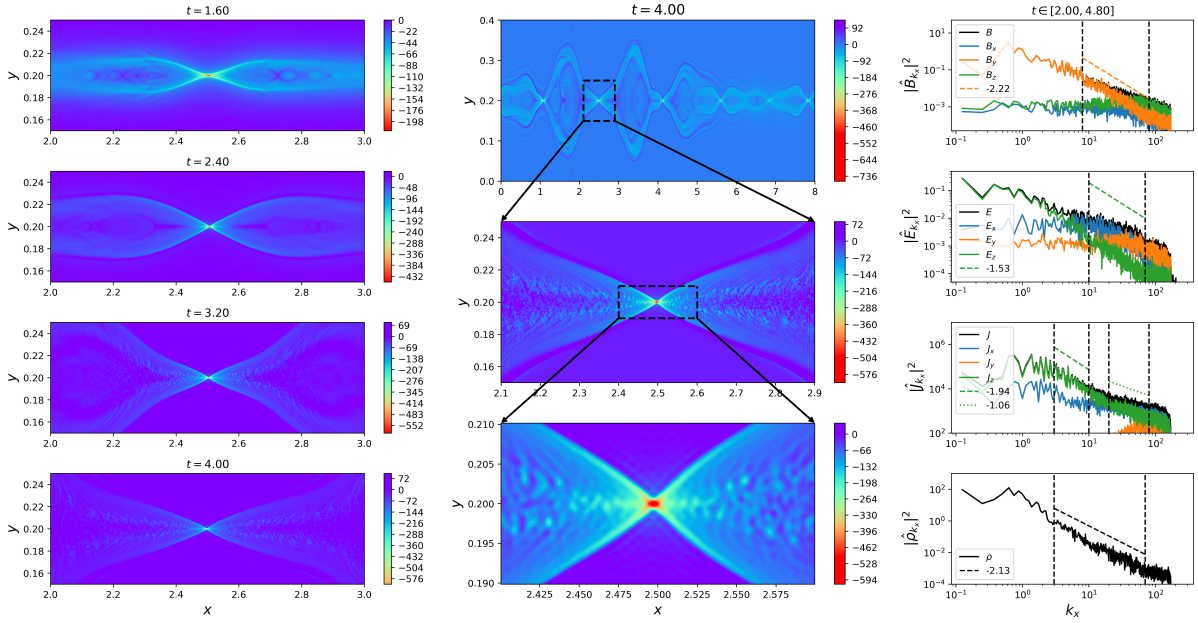

Figure 2.14: Out-of-plane current density J_z and the power spectra in Run 5. Left column: time evolution of J_z inside the domain $x \in [2.0, 3.0]$ and $y \in [0.15, 0.25]$. Middle column: the hierarchic structure of the current sheet (color is J_z) at $t = 4.00$. Top panel is the whole simulation domain. Middle and bottom panels are blow-ups as marked by the boxes and arrows. Right column: time-averaged power spectra of the magnetic field $\mathbf{B}$, the electric field $\mathbf{E}$, the current density $\mathbf{J}$ and the density ρ calculated at the central line of the current sheet $y = 0.2$ in log-log scale. The blue, orange and green lines represent the x, y and z components of the vector fields respectively and the black lines are the sum of the 3 components in the first three panels. The dashed and dotted lines are linear fits for the spectra of B_y, E_z, J_z and ρ. The k_x ranges for the fits are marked by the vertical dashed lines and the slopes of the fits are written in the legends. The time period for averaging the spectra is written at the top of the column.

2.2.3.2 Reconnection Rate and Dissipation

In Figure 2.16 we plot in the top panel the reconnected magnetic flux ψ as a function of time for all runs. The curves from right to left correspond to Run 0,1,2,3,4,5 and 10

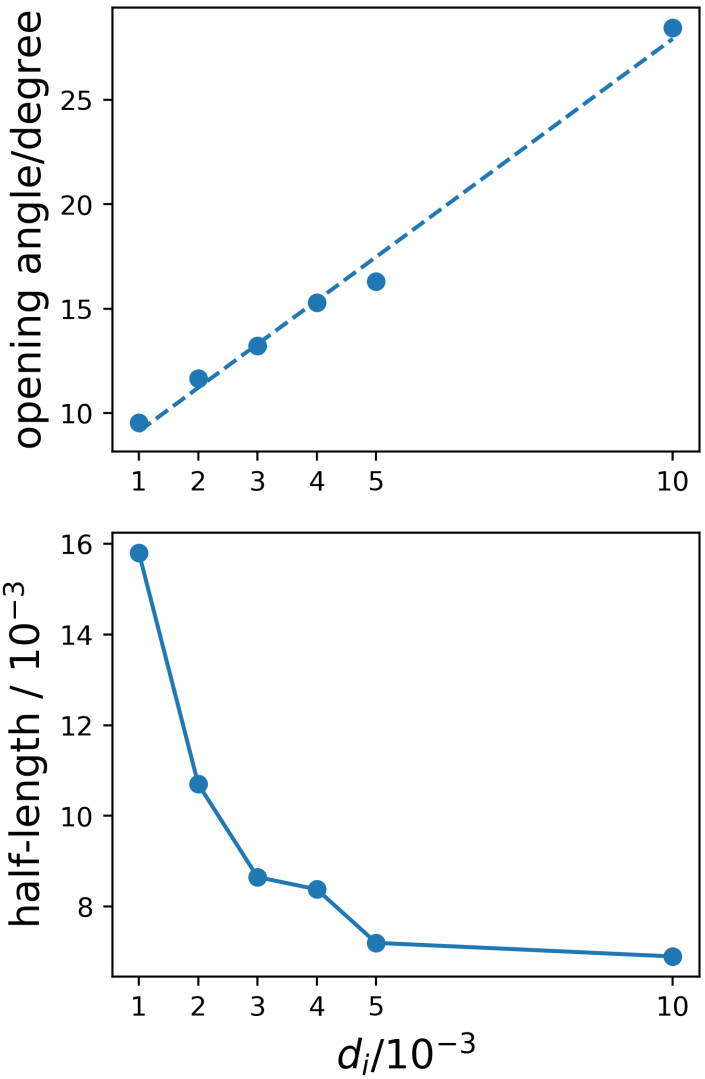

Figure 2.15: Top: opening angle of the exhaust as a function of d_i. Bottom: half-length of the current sheet at the X-point as a function of d_i.

respectively. For each run, we confine the calculation to be within the area $x \in [2.0, 3.0]$ and $y \in [0.15, 0.25]$. As the code evolves the z-component of the vector potential ψ instead of the in-plane magnetic field, the reconnected magnetic flux is easily acquired by recording the value of ψ at the X-point, defined as the point at which ψ peaks. The time at which we begin to record ψ is $t = 0.8$ after the dominant X-point in this area is formed. All runs go through a slowly-growing initial phase with slightly different reconnection rate which increases with d_i

and the initial phase corresponds to the evolution of the first tearing. For Run 1-5 and 10, fast reconnection is triggered simultaneously with the formation of the Hall-like configuration, e.g. at $t \sim 5$ for Run 1 and $t \sim 4$ for Run 2. The larger d_i, the earlier the fast-reconnection phase is entered. Then the reconnection rate remains steady during the fast-reconnecting stage. However, for Run 0, i.e. the MHD case, the process is different from the other runs. First, the reconnection rate increases when the secondary tearing happens, i.e. when the secondary current sheet breaks up at $t \sim 6$, instead of the formation of a Hall-like structure. Second, the reconnection does not maintain a steady rate throughout the fast-reconnection stage. At $t \lesssim 8$, the reconnection rate increases once again due to the third or higher-order tearing (see bottom panel on the middle column of Figure 2.11). The dashed lines in the top panel of Figure 2.16 are linear fits of the $\psi(t)$ curves and the slopes of the fitted lines are written in the legend. In the middle panel we plot the reconnection rate calculated from the linear fits as a function of d_i. For Run 1-5, the reconnection rate increases with d_i roughly linearly and its value is around $0.03 - 0.05$. For Run 10, the reconnection rate is 0.058, lower than the linear extrapolation of Run 1-5 as shown by the dashed line, indicating a convergence of the reconnection rate as d_i increases. The reconnection rates of these runs are consistent with previous Hall-reconnection simulations (Ma & Bhattacharjee, 2001). The triangles correspond to the two reconnection rates before and after the second acceleration of the reconnection in Run 0. Note that the fastest reconnection rate in the MHD case is even larger than that of the $d_i = 0.001$ run. If the resolution of the simulation is good enough to resolve smaller-scale current sheets, the reconnection rate is supposed to increase further. In the bottom panel of Figure 2.16 we plot the reconnection rate as a function of the opening angle for Run 1-5 and 10. This plot indicates that as the opening angle of the exhaust increases, the reconnection rate goes up when the opening angle is small but does not go up all the way: there is a maximum reconnection rate allowed in the system. Liu et al. (2017) discussed this problem by a simple model where the micro-scale diffusion region is embedded inside the large-scale MHD region. As the exhaust opens up, the magnetic field right upstream of the diffusion region is reduced because of the balance between the magnetic pressure gradient force and the magnetic tension force in the MHD-scale upstream

region. As a consequence, the outflow speed and the reconnection rate are also reduced. In their estimate, the opening angle corresponding to the maximum reconnection rate is $\alpha = 2 \times \arctan(0.31) = 0.60 = 34^o$ which is not reached by our simulations but from the bottom panel of Figure 2.16 we can see the trend of a saturated reconnection rate as the opening angle increases toward 30^o.

In the top panel of Figure 2.17 we show the time evolution of the dissipation rate averaged over the whole simulation domain:

$$D = \langle \eta J^2 \rangle = \frac{1}{n_x n_y} \int \eta J^2 = \frac{1}{n_x n_y} \int \mathbf{J} \cdot \mathbf{E}' \tag{2.41}$$

where

$$\mathbf{E}' = \mathbf{E} + \mathbf{u_e} \times \mathbf{B} \tag{2.42}$$

is the electric field in electron frame. The evolution of the dissipation rate is different from that of the reconnected magnetic flux (top panel of Figure 2.16). The reconnection rate increases abruptly when either the second tearing or the Hall-reconnection is triggered while the dissipation rate increases more smoothly with time due to the averaging over the whole domain. In addition, the dissipation rate at the end of the simulation decreases with d_i for $d_i \geq 0.003$: as d_i increases, the total time of reconnection shortens due to the finite magnetic flux in the simulation domain and faster reconnection rate, leading to the decrease of the amplitude of the current density at the end of the simulation. In the middle panel we show the ratio between the Hall-current dissipation rate

$$D_{xy} = \langle \eta \left(J_x^2 + J_y^2 \right) \rangle \tag{2.43}$$

and the total dissipation rate D as a function of time for each run. For the MHD case this ratio remains 0 as there is no Hall current while for $d_i \neq 0$, the significance of the Hall-current dissipation grows with time once the Hall-reconnection stage initiates and the ratio tends to saturate. Even for $d_i = 0.001$, the Hall-current dissipation accounts for $\sim 40\%$ of the total dissipation at the end of the simulation. As d_i increases, this ratio converges to $\sim 55\%$, i.e. the dissipation by the Hall current becomes more important than that of the out-of-plane current. We also check the ratio between the parallel dissipation rate $\eta J_\parallel^2$ and the total

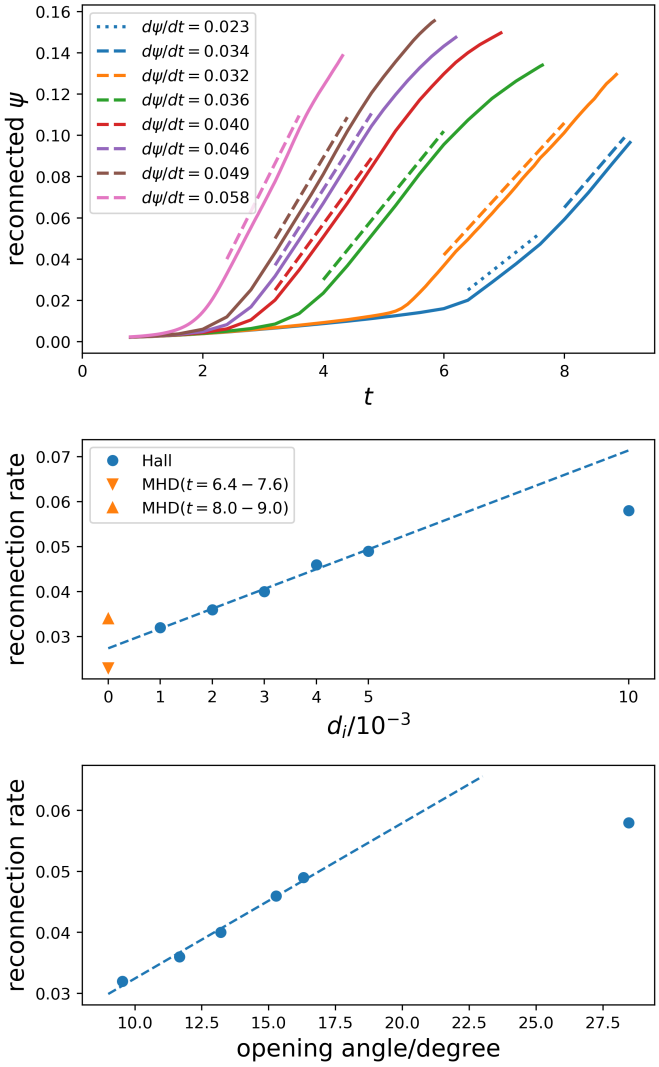

Figure 2.16: Top: reconneced magnetic flux at the X-point as a function of time. Dashed lines are linear fits whose slopes are shown in the legend. Blue, orange, green, red, purple, brown and pink lines (from right to left) are Run 0, 1, 2, 3, 4, 5, 10 respectively. Middle: reconnection rate calculated by the linear fits as a function of d_i. Note that for Run 0 there are two growth rates corresponding to the two fast-growing stages as shown in the top panel. Bottom: reconnection rate as a function of the opening angle for Run 1-5 and 10.

dissipation rate where $J_{\parallel} = \mathbf{J} \cdot \mathbf{B}/B$ and show this ratio in the bottom panel. It evolves similarly with the Hall-dissipation ratio and converges to a value $\sim 45\%$ as d_i increases.

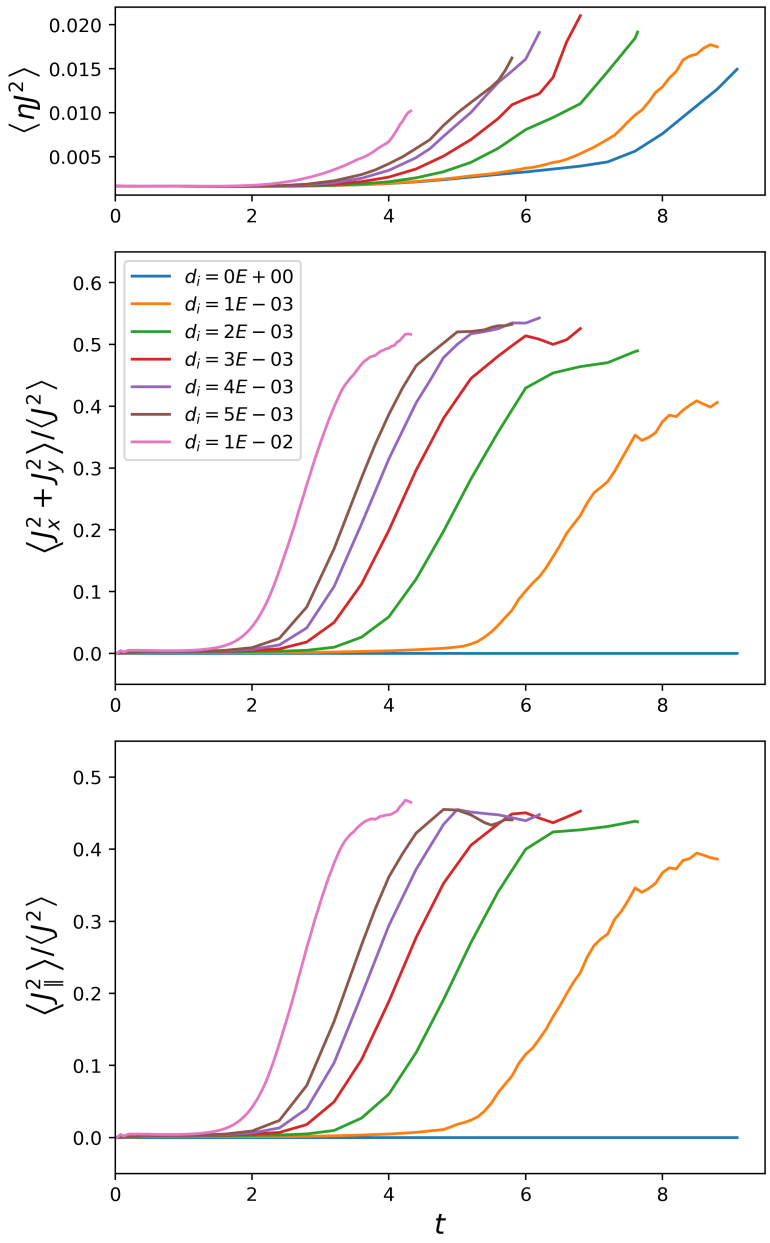

Figure 2.17: Top: dissipation rate ηJ^2 averaged over the whole simulation domain. Middle: the ratio between the Hall-current dissipation rate $\eta \left(J_x^2 + J_y^2\right)$ and the total dissipation rate ηJ^2. Bottom: the ratio between the parallel dissipation rate and the total dissipation rate.

2.2.3.3 Power Spectra

It is expected that the nonlinear recursive generation of plasmoids leads to an energy cascade from large to small scales, leading to well-developed power-law spectra. The development of turbulence with an extended inertial range is important both to energization (Lu et al., 2019) and scattering of particles (Giacalone et al., 2000). In the MHD case, a phenomenological model based on the recursive tearing mode developed by Tenerani & Velli (2020) leads to a spectrum $|B_y(k_x)|^2 \propto k_x^{-4/5}$. In the kinetic regime, i.e. below the ion inertial length, the power spectra of the turbulence generated are different due to the presence of kinetic mechanisms, as discussed below. We inspect the power spectra of various quantities: the magnetic field **B**, the electric field **E**, the current density **J** and the density ρ. The right columns of Figure 2.11-2.14 are the spectra for Run 0, 1, 2, 5 respectively. The spectra are calculated at the central line of the current sheet $y = 0.2$ and are averaged over the time periods of steady and fast reconnection. The time periods for averaging the spectra are written at the top of the columns. The blue, orange and green lines are the x, y and z components of the vector fields respectively. The black lines in the top three panels are the sum of the 3 components. Note that in some panels the total power spectrum is covered by the dominant component, e.g. in Run 0 (Figure 2.11) E_z overlap with the total power of **E** as E_x and E_y are exactly 0 in this run. We fit the powers of B_y, E_z, J_z and ρ over k ranges marked by the vertical dashed lines where obvious exponential relations exist. The fits are shown by the dashed and dotted lines whose slopes are written in the legends.

We first look at the power spectra of **B** in Figure 2.11-2.14. At the center of the current sheet, the dominant component is B_y as shown by the orange lines. We see that the power spectra peak around $k_x \approx 0.6 - 0.8$ in all of the runs shown in Figure 2.11-2.14. This peak corresponds to the 5-6 large-scale plasmoids in all these runs as shown in the top panels on the middle columns of Figure 2.11-2.14. Note that the number of the large plasmoids is a nonlinear effect related probably to the initial condition and the domain size rather than the fastest-growing linear mode. For Run 0 and Run 1, a clear two-segment power spectrum of B_y is seen with the break point at $k_x \approx 20$, i.e. $\lambda \approx 0.05$. This value of λ is close to the length

of the third-order current sheets in Run 0 (see the panel $t = 6.40$ on the left column of Figure 2.11) and the length of the current sheet at the X-point in Run 1, which is around $0.03 - 0.04$ (see the bottom panel of Figure 2.15). Below the break point, the spectral index (defined as the absolute value of the slope) is smaller than 1 while above the break point the spectral index is very close to 2. Especially, in Run 0 the slope of B_y spectrum below the break point is approximately $-4/5$, the value estimated by Tenerani & Velli (2020), indicating that in the low-k_x range the spectra are controlled by the recursive plasmoid generation. In high-k_x range the -2 slope is mainly due to the discontinuities near the boundaries of the plasmoids. For Run 2, the B_y spectrum becomes smooth. Although we can still see that the slope of the spectrum changes with k_x, we are unable to find a break point. For Run 5, the B_y spectrum is almost a straight line with a slope -2.22. The change of the shape of B_y spectra is related to the formation of the X-point structure due to the Hall effect. As d_i increases, the recursive growth of plasmoids is suppressed. As a result, the shallow part of the B_y spectrum, which represents the recursive generation of plasmoids, is gradually taken over by the steeper spectrum indicating more discontinuities/shocks produced in the Hall cases. The second panels on right columns of Figure 2.11-2.14 show the power spectra of $\mathbf{E}$ and we calculate the spectral indices for E_z, the out-of-plane electric field. For Run 0 and Run 1, E_z is dominant and the power spectrum of E_z consists of two segments like B_y though the high-k part of E_z spectrum is steeper than B_y with slopes around -2.3. For Run 2, E_z still shows a two-segment power spectrum while B_y does not. For Run 5, E_z power spectrum is almost a straight line with slope -1.53, flatter than that of B_y. We also notice that, as d_i increases, the energy in the Hall electric field E_x (the blue lines) exceeds the energy in E_z at small scales (see Figure 2.13 and 2.14). In Run 5, E_x dominates the electric energy at scales $k_x > 5$, i.e. the Hall electric field is the major contributor to the electric energy at scales $\lambda < 0.2$. The third panels of Figure 2.11-2.14 show the power spectra of the current density $\mathbf{J}$ and we calculate the spectral indices for J_z. We see that J_z dominates the power of $\mathbf{J}$ in all runs except at quite small scales in Run 2 and Run 5. For Run 0-2, the J_z power spectra are similar with spectral indices around $1.5 - 1.8$ while for Run 5, the J_z power spectrum has a break point at $k_x \sim 10 - 20$ below which the spectral index is around 2 and above

which the spectral index is around 1. The bottom panels of Figure 2.11-2.14 show the power spectra of the density ρ and we see that the 4 runs are very similar with slopes around -2, indicating that the Hall effect does not change the compressional properties significantly in this d_i range. For comparison, we plot the spectra for Run 10 in Figure 2.18. We see that **B**, **E** and **J** show similar power spectra with Run 5 though E_z spectrum is steeper and it is hard to calculate the spectral index for J_z at large scales due to the strong oscillation. The density has a significantly steeper power spectrum in Run 10 with slope -2.75, indicating a stronger damping of the compressible fluctuations in this run.

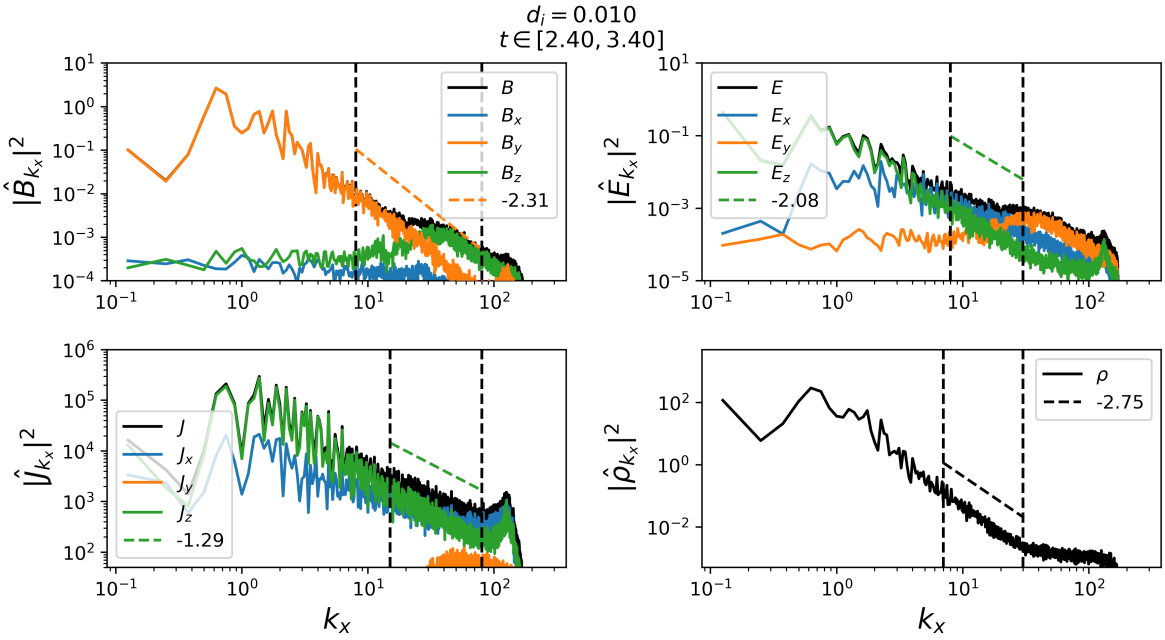

Figure 2.18: Power spectra averaged from $t = 2.4$ to $t = 3.4$ for Run 10 in log-log scale. The spectra are calculated at the central line of the current sheet $y = 0.2$. From top-left to bottom-right panels are the magnetic field **B**, the electric field **E**, the current density **J** and the density ρ. The blue, orange and green lines are the x, y and z components of the vector fields respectively. The black lines are the sum of the 3 components in panels for **B**, **E** and **J**. The dashed lines are the fits for B_y, E_z, J_z and ρ over k_x ranges marked by the vertical dashed lines. The slopes of the fits are shown in the legends.

2.2.4 Summary

In this section, we have carried out a series of 2.5D Hall-MHD simulations to study the transition from resistive-MHD reconnection to Hall-reconnection. We show that as the ion inertial length increases from 0 to above the inner-layer thickness of the ideal tearing mode, the evolution and the structure of the current sheet change significantly. For $d_i = 0$ (or $d_i \ll \delta_{TI}$ where δ_{TI} is the inner layer thickness of the tearing mode), the reconnection is purely plasmoid-dominant, consistent with the recursive reconnection picture (e.g. Shibata & Tanuma, 2001; Tenerani et al., 2015). When $d_i \gg \delta_{TI}$, the reconnection evolves into the Hall-dominant regime soon after the first tearing: a single X-point with exhaust opened up. When $d_i \lesssim \delta_{TI}$, we see an intermediate state: an X-point with finite length is formed and plasmoids continue to be generated and ejected out from the X-point. The steady-nonlinear reconnection rate for Hall reconnection is around $0.03 - 0.06$, increasing with d_i and with a trend toward a maximum value around 0.06 in our simulations. The resistive-MHD case is also able to give fast nonlinear reconnection rate (0.034) and this rate increases with time as higher-order tearing happens. The Hall effect changes the energy dissipation significantly. The Hall current system accounts for a large portion (40%) of the total dissipation even in our Run 1 where the reconnection is the intermediate plasmoid+Hall state and as d_i increases this portion converges to a value $\gtrsim 50\%$. Last, the Hall term changes the power spectra of various quantities a lot, especially the electromagnetic fields **B** and **E**. For instance, the reconnecting magnetic field component B_y shows two-segment power spectra with slopes around $-0.6 \sim -0.8$ at small k_x and slopes around -2 at large k_x in Run 0 and 1 while in Run 2-5 and 10 its power spectra are one-segment and become steeper as d_i increases. This change of the spectra is related to the suppression of the recursive plasmoid generation and the formation of Petschek-like X-points as the Hall effect becomes stronger.

In the Hall-MHD model, temperature anisotropy is absent but it is known to develop in ion scale current sheets (Drake et al., 2009). This temperature anisotropy may facilitate the formation of slow shocks so that the structure of the reconnection becomes Petschek-like more easily (Liu et al., 2011). Besides, the formed temperature anisotropy may lead to the

growth of various instabilities, e.g. fire-hose instability capable of perturbing the outflow regions (Hietala et al., 2015).

Cassak et al. (2010) propose that "bistability" exists in Hall-MHD reconnection: the Sweet-Parker and Hall solutions are both stable. However, their result is not applicable to many astrophysical environments where the resistivity is so small that the Sweet-Parker current sheet cannot form in the first place. Huang et al. (2011) observe the bounce between the Hall-like X-point and the Sweet-Parker-like long current sheet in their simulations of two coalescing magnetic islands. However, in our simulations we do not observe such a phenomenon. In our Run 1 we see a stable status where plasmoids are generated out of the X-point continuously but we do not see the transition from the X-point structure back to a long current sheet. The reason may be that our initial configuration is a pressure-balanced Harris current sheet rather than two coalescing magnetic islands. In the simulations by Huang et al. (2011), the large coalescing islands may possibly "squeeze" the current sheet in between and destroy the opened-up exhaust of the Hall-like structure.

In the solar wind and the solar corona, the relation between d_i, a_0 and δ_{TI} may be similar to the setup in this work (see Pucci et al., 2017). Thus our study may help us understand the reconnection process in these environments. However, the simulations in this study are 2.5D and it is necessary to extend this work to 3D, which will be part of our future work.

2.3 Oblique Tearing Modes with the Guide Field and Hall Effect

2.3.1 Introduction

In this section, we discuss the linear stability problem of a current sheet in a three-dimensional configuration. As mentioned in Chapter 1, the linear theory of the fast tearing instability, in two-dimensional MHD regimes, was advanced greatly in the last two decades (e.g. Tajima & Shibata, 2002; Loureiro et al., 2007; Pucci & Velli, 2013). Pucci et al. (2017) extended the ideal tearing theory to include the Hall effect and the modifications it introduces to the critical aspect ratio for triggering the ideal tearing mode. Baalrud et al. (2012) studied the

oblique tearing mode in the case of a strong guide field. They showed that, in the constant-ψ regime, i.e. the large-k_x regime where k_x is the parallel wave number, the fastest growing modes are no longer the parallel modes but modes with finite k_z where k_z is the wave number along the guide field direction.

In this study, we carry out a linear analysis of the tearing mode instability in a generalized configuration. We allow a guide field with arbitrary strength and include the Hall effect. We numerically solve the linear eigenvalue problem for oblique tearing modes. We show that, although a guide field results in a resonant surface departing from the parallel direction in the constant-ψ regime, the overall fastest growing mode in the (k_x, k_z) plane is still parallel, i.e. the same as in the case without guide field. With the Hall effect, the guide field generates a dispersive $\omega(k_z)$ where ω is the oscillation frequency. This section is organized as follows. In Section 2.3.2, we present the linear equation set that is solved. In Section 2.3.3 we show the numerical solutions of the linear equation set. In Section 2.3.4, we conclude this study and discuss possible future works.

2.3.2 Linear MHD equation set for oblique tearing mode

We start from the three-dimensional MHD equation set with Hall term and resistive term. The background flow is assumed to be 0 everywhere $\mathbf{U} \equiv 0$ and the background density is assumed to be uniform $\rho_0 \equiv 1$. The background magnetic field is of the form

$$\mathbf{B_0} = B_x(y)\hat{e}_x + B_z(y)\hat{e}_z \tag{2.44}$$

where B_z is the guide field and the background pressure $P = P(y)$ such that

$$P(y) + \frac{1}{2}\left[B_x^2(y) + B_z^2(y)\right] = Const \tag{2.45}$$

The above configuration is a solution to the Hall-MHD equation set. In this study, we will restrict the background magnetic field to be a Harris current sheet plus a uniform guide field

$$B_x(y) = B_0 \tanh\left(\frac{y}{a}\right), B_z(y) = B_g \tag{2.46}$$

with $B_0 \equiv 1$, $a \equiv 1$, and B_g being a varying parameter.

We write perturbations in the form:

$$\mathbf{u} = \mathbf{u}(y)e^{\gamma t + i\mathbf{k}\cdot\mathbf{x}}, \quad \mathbf{b} = \mathbf{b}(y)e^{\gamma t + i\mathbf{k}\cdot\mathbf{x}} \tag{2.47}$$

where $\mathbf{k} = k_x\hat{e}_x + k_z\hat{e}_z$. We assume incompressibility

$$\nabla \cdot \mathbf{u} = 0 \tag{2.48}$$

The equation set for $\mathbf{u}$ and $\mathbf{b}$ is written as (taking curl of the 1st-order momentum equation to get rid of pressure p_1^T)

$$\gamma\nabla \times \mathbf{u} = \nabla \times (\mathbf{B}\cdot\nabla\mathbf{b} + \mathbf{b}\cdot\nabla\mathbf{B}) \tag{2.49a}$$

$$\gamma\mathbf{b} = \mathbf{B}\cdot\nabla\mathbf{u} - \mathbf{u}\cdot\nabla\mathbf{B} + \frac{1}{S}\nabla^2\mathbf{b} - \gamma d_i\nabla\times\mathbf{u} \tag{2.49b}$$

Here $S = aV_A/\eta$ is the Lundquist number. We adopt the method by (Cao & Kan, 1991) to simplify the equation, i.e. we rotate the coordinate system with respect to the y-axis such that the new $\tilde{x}$ axis is aligned with the wave vector:

$$\mathbf{k} = k\hat{e}_{\tilde{x}} \tag{2.50}$$

where $k = \sqrt{k_x^2 + k_z^2}$. Then the problem becomes essentially 2D because $\partial_{\tilde{z}} \equiv 0$. In the new coordinate system we get the new form of the background magnetic field

$$\tilde{B}_{\tilde{x}}(y) = B_x(y)\cos\theta + B_z(y)\sin\theta \tag{2.51a}$$

$$\tilde{B}_{\tilde{z}}(y) = -B_x(y)\sin\theta + B_z(y)\cos\theta \tag{2.51b}$$

where $\theta = \arctan(k_z/k_x)$. The closed equation set for $(u_{\tilde{x}}, b_y, b_{\tilde{z}})$ is

$$\gamma\left(u_y'' - k^2u_y\right) = k\left[\tilde{B}_{\tilde{x}}b_y'' - \left(\tilde{B}_{\tilde{x}}'' + k^2\tilde{B}_{\tilde{x}}\right)b_y\right] \tag{2.52a}$$

$$\begin{aligned}\frac{1}{S}\left(b_y'' - k^2b_y\right) =& \gamma b_y + k\tilde{B}_{\tilde{x}}u_y \\ & - id_ik\left(-k\tilde{B}_{\tilde{x}}b_{\tilde{z}} + \tilde{B}_{\tilde{z}}'b_y\right)\end{aligned} \tag{2.52b}$$

$$\frac{1}{S}\left(b_{\tilde{z}}'' - k^2 b_{\tilde{z}}\right) = \left(\gamma + \frac{k^2\tilde{B}_{\tilde{x}}^2}{\gamma}\right) b_{\tilde{z}} - \frac{k\tilde{B}_{\tilde{x}}\tilde{B}_{\tilde{z}}'}{\gamma} b_y + \tilde{B}_{\tilde{z}}' u_y - i d_i \frac{\gamma}{k}\left(u_y'' - k^2 u_y\right) \tag{2.52c}$$

where we have replaced ib_y with b_y and prime means ∂_y. $u_{\tilde{x}}$ and $b_{\tilde{x}}$ can be derived from the divergence-free conditions of $\mathbf{u}$ and $\mathbf{b}$ and the equation for $u_{\tilde{z}}$ is

$$\gamma u_{\tilde{z}} = i\left(k\tilde{B}_{\tilde{x}} b_{\tilde{z}} - \tilde{B}_{\tilde{z}}' b_y\right) \tag{2.53}$$

Note that Eq (2.52) is general, i.e. we can arbitrarily choose functions $B_x(y)$ and $B_z(y)$ but in this study we use Eq (2.46).

It is immediately seen that in the case $d_i = 0$, Eq (2.52) is purely real, i.e. there are no propagating modes since the solution of γ is real. If $d_i > 0$, in general γ is complex, meaning that the modes are propagating. But there is a special case $\tilde{B}_{\tilde{z}}' = 0$ when $b_{\tilde{z}}$ has an exactly $\pi/2$ phase-difference with u_y and b_y and thus by doing the transformation $ib_{\tilde{z}} \to b_{\tilde{z}}$, Eq (2.52) becomes purely real and so for γ. This is the case when a mode is parallel ($k_z = 0$) and the guide field is uniform, e.g. the case considered by Pucci et al. (2017). In reality, when $k_z = 0$, a uniform B_z has no effect on Eq (2.52) as only B_z' enters the equation.

Last, we need to specify the boundary condition in order to solve the eigenvalue problem. Far from the center of the current sheet, we have all the derivatives of $\tilde{B}_{\tilde{x}}$ and $\tilde{B}_{\tilde{z}}$ in Eq (2.52) to be 0 and it is easy to find that the solutions decay exponentially with distance as $\exp(-k|y|)$. This is the same boundary condition as the classic 2D tearing mode.

2.3.3 Results

We use the boundary-value-problem (BVP) solver implemented in the Python library SciPy (Virtanen et al., 2020) to solve Eq (2.52). The solver adopts a 4th order collocation algorithm with the control of residuals (ref. Kierzenka & Shampine, 2001; Ascher et al., 1994) and is able to solve the eigenvalue and eigen-functions simultaneously. Unlike previous works, e.g. (Baalrud et al., 2012), which use (k, θ) to denote the wave vector, we present our results in (k_x, k_z) space. In this study, we fix $S = 10^4$, a value large enough for astrophysical

applications (corresponding to $S_L = 10^8$ for a Sweet-Parker current sheet) and not too large so that it is not very expensive to solve Eq (2.52). The domain used for solving the equation is $y \in [-15, 15]$.

We first consider the MHD case, i.e. $d_i = 0$, for which the problem is purely real. In Figure 2.19, we show the dispersion relation $\gamma - k_z$ at two fixed k_x: $k_x = 0.12$ in top panel and $k_x = 0.5$ in middle panel. $k_x = 0.12$ corresponds approximately to the fastest-growing parallel mode. In each panel, different curves represent different guide field strength B_g. Dark to light colors correspond to small (0) to large (100) B_g as written in the legend. From top panel ($k_x = 0.12$), we observe that γ in general declines as k_z increases and increasing B_g speeds up the decline of γ with k_z. The fastest growing mode is always the parallel one ($k_z = 0$). On the contrary, the middle panel ($k_x = 0.5$) shows very different results from the top panel. For small B_g ($B_g \lesssim 1$), $\gamma - k_z$ is monotonically decreasing. As B_g increases ($B_g \gtrsim 2$), the $\gamma - k_z$ curve transits from monotonic to concave and the fastest growing mode is no longer the parallel one but instead located at the new resonant surface. In the bottom panel of Figure 2.19 we show k_z of the fastest growing mode ($k_{z,m}$) at $k_x = 0.5$ (peaks of curves in the middle panel) as a function of $1/B_g$. It is observed that $k_{z,m}$ is proportional to B_g^{-1}, consistent with the prediction of the resonant surface:

$$\mathbf{k} \cdot \mathbf{B_0} = 0 \tag{2.54}$$

which gives

$$k_z = -\frac{k_x B_x}{B_g} \tag{2.55}$$

We need to stress that, although a strong guide field leads to an increase in $\max(\gamma(k_z))$ at a fixed k_x in the constant-ψ regime, the increase is limited to a small amount. As can be seen from the bottom panel of Figure 2.19, as $B_g \to \infty$, $\max(\gamma(k_z))$ increases from about 3.7×10^{-3} to about 3.88×10^{-3}, i.e. only by $\sim 5\%$. Furthermore, the increase of $\max(\gamma(k_z))$ only happens in the constant-ψ regime (large k_x) but not at the most unstable k_x, as shown in the top panel of Figure 2.19. Thus, a strong guide field B_g cannot change the fastest growing mode in the (k_x, k_z) plane: it is still the most unstable parallel mode. Note that a

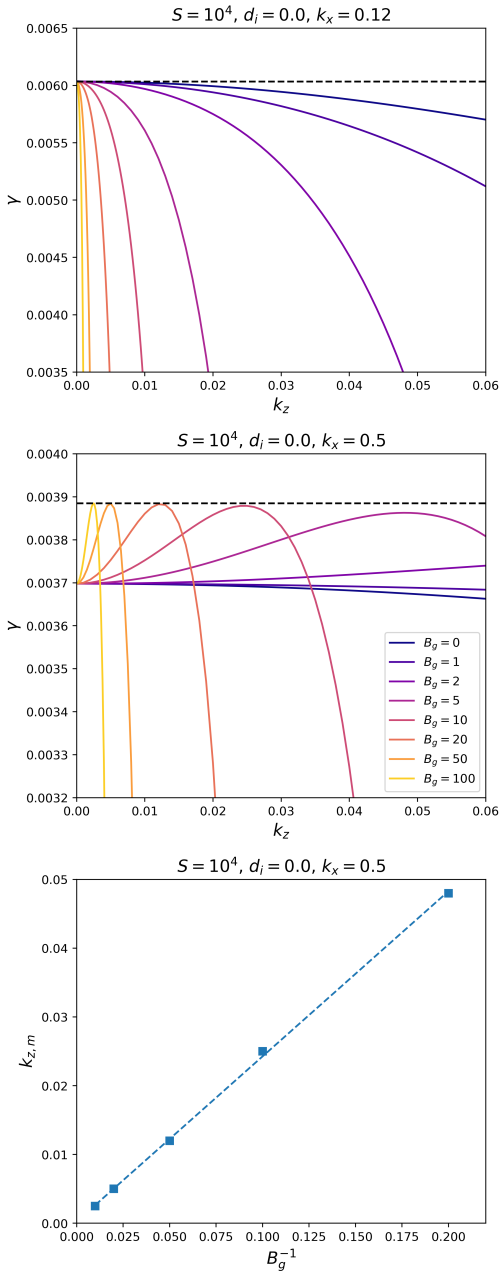

Figure 2.19: Results for $S = 10^4$ and $d_i = 0$. Top and middle panels: $\gamma - k_z$ curves at $k_x = 0.12$ and at $k_x = 0.5$. Colors represent guide field strength. Bottom panel: k_z of the fastest growing mode at $k_x = 0.5$ as a function of B_g^{-1}.

uniform B_g has no influence on the parallel modes. To support this conclusion, in Figure 2.20, we plot $\gamma - k_x$ curves at $k_z = 0.002$ in the top panel and at $k_z = 0.01$ in the middle

panel. Colors represent different B_g and the black dashed curve is $k_z = 0$, i.e. parallel modes, for reference. At a fixed k_z, although a strong guide field raises the $\gamma - k_x$ curve slightly in the constant-ψ regime, it lowers the curve significantly at smaller k_x. With increasing B_g, the fastest growing k_x is shifted toward the right, i.e toward larger values, while the peak growth rate declines rapidly. In bottom panel of Figure 2.20, we plot $\gamma - k_x$ curves for a fixed $B_g = 20$ but varying k_z. It can be seen by comparing the middle and bottom panels that increasing k_z with constant B_g has a nearly identical effect to increasing B_g with constant k_z. This is because in Eq (2.52), in the case of a uniform guide field, all terms containing B_g are of the form $k_z B_g$. From this plot, we can see that, the maximum growth rate $\max(\gamma(k_x))$ as a function of k_z is monotonically decreasing, supporting the conclusion that the fastest-growing mode in the 2D (k_x, k_z) plane is always the most unstable parallel mode even with a strong guide field B_g. Unless the current sheet is very short along x such that k_x is limited to the constant-ψ regime or the system size along z is finite, we do not expect the most unstable mode to be oblique.

We then consider the case with finite ion inertial length. In this case, γ in Eq (2.52) is complex and we decompose it into real and imaginary parts $\gamma - i\omega$ where γ is the growth rate and ω is the oscillation frequency. We set $d_i = 1.0$, i.e. equal to the current sheet thickness. In Figure 2.21 we plot $\gamma - k_z$ (top panel) and $\omega - k_z$ (bottom panel) curves for different guide field strength at $k_x = 0.5$. Compared with the middle panel of Figure 2.19, the growth rate is larger with a finite d_i as already reported by (Pucci et al., 2017). Similar to the MHD case, the increase of $\max(\gamma(k_z))$ has an asymptotic value as B_g increases. Thus, the conclusion made in the MHD case is not modified. The behavior of ω is rather interesting. For weak guide field, ω is almost a linear function of k_z. Especially, for $B_g = 0$, $\omega - k_z$ is exactly a straight line, i.e. the modes are non-dispersive along z direction. As B_g increases, similar to γ, $\omega(k_z)$ is no longer monotonic but shows a decline with k_z after reaching a peak value. In bottom panel of Figure 2.21, we mark the peak of each individual curve by a square and the black dashed line is the linear fit of the five squares. The extrapolation of the dashed line goes exactly through the origin with a slope $\omega/k_z = 0.62$, indicating that the maximum

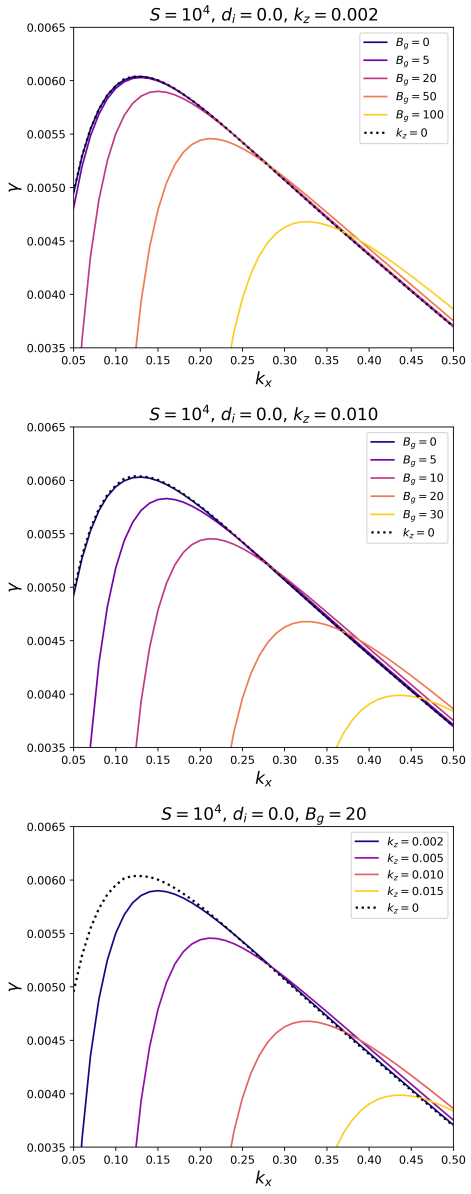

Figure 2.20: Results for $S = 10^4$ and $d_i = 0$. Top and middle panels: $\gamma - k_x$ curves at $k_z = 0.002$ and at $k_z = 0.01$. Colors represent different B_g. Bottom panel: $\gamma - k_x$ curves for $B_g = 20$ and varying k_z. The dashed curve in each panel is $k_z = 0$, i.e. parallel modes, for reference.

ω, i.e. the mode with fastest phase speed along x as k_x is fixed, has a phase speed along z which is independent of B_g when B_g is large. We have verified that the slope of the dashed line is an increasing function of k_x (not shown here). Note that, the k_z corresponding to

max $(\omega(k_z))$ does not necessarily correspond to max $(\gamma(k_z))$. In addition, ω and γ drop to 0 at exactly the same k_z which is proportional to $1/B_g$ as can be read from Figure 2.21.

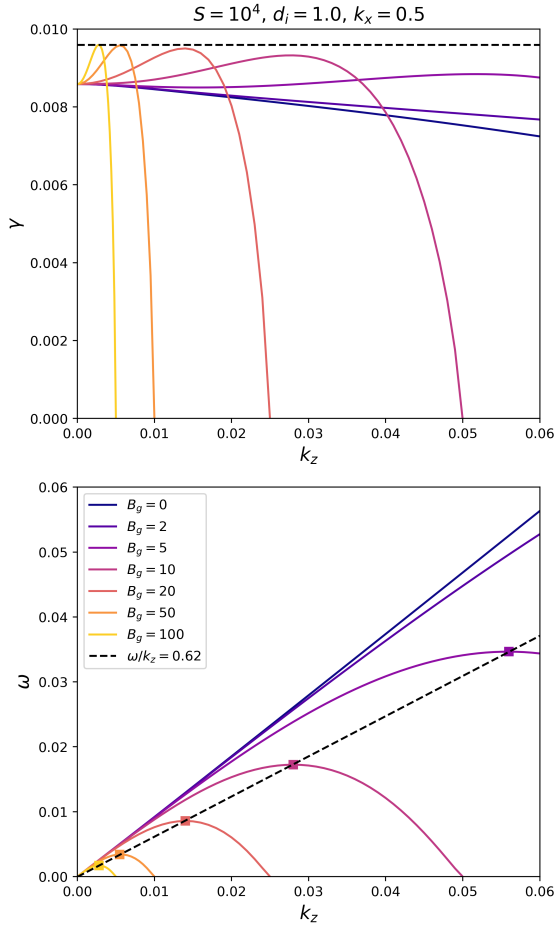

Figure 2.21: $\gamma - k_z$ and $\omega - k_z$ curves for $S = 10^4$, $d_i = 1.0$ and $k_x = 0.5$. Colors represent guide field strength B_g. Here γ and ω are the real and imaginary parts of the complex γ in Eq (2.52).

In Figure 2.22, we show the eigen-functions solved from Eq (2.52) for $S = 10^4$, $d_i = 1.0$ and $k_x = 0.5$. Top row is u_y, middle row is b_y and bottom row is $b_{\tilde{z}}$. Note that the range of abscissa is smaller for $b_{\tilde{z}}$ because the inner layer of $b_{\tilde{z}}$ is much thinner than those of the other two quantities (Pucci et al., 2017). Blue and orange curves in each panel are real and imaginary parts respectively. Column (a) is for $k_z = 0$ and thus B_g can be any value. Column (b) is for $k_z = 0.06$ and $B_g = 0$. Column (c) is for $k_z = 0.06$ and $B_g = 5$. The main

point of Figure 2.22 is that, with Hall effect, the eigen-functions of the oblique mode show strong oscillation along y, as can be seen from column (b). The oscillation is caused by the term $b_y''/S \sim -id_i k \tilde{B}_z' b_y$ in Eq (2.52b) from which we can estimate a wave number along y to be

$$k_y \sim (1-i)\sqrt{\frac{1}{2} S k d_i B_x' \sin\theta} \tag{2.56}$$

in the sense that $b_y \sim \exp(k_y y)$. With a guide field, as shown in column (c), the eigen-functions become asymmetric in y as expected (Baalrud et al., 2012). In addition, by comparing column (b) and (c), we see that the strong guide field suppresses the y-oscillation. The phenomenon of y-oscillation was not reported by the previous study on oblique tearing mode with finite ion inertial length (Cao & Kan, 1991). The reason was unknown but it might be that Cao & Kan (1991) carried out linear simulations to solve the problem and the resolution (not stated in (Cao & Kan, 1991)) was not enough. Recently, Akçay et al. (2016) carried out two-fluid simulations of the oblique tearing mode and in their simulations this oscillation was seen (see their Figure 4).

2.3.4 Summary

In this study, we carried out linear stability calculation of the oblique tearing mode with both guide field and Hall effect. We derived the generally-applicable linear equation set for tearing mode instability. We show that, although a guide field leads to a non-parallel resonant surface $k_z \propto 1/B_g$ in the constant-ψ regime, the most unstable mode in the (k_x, k_z) space is not changed: it is still the fastest-growing parallel mode. The increase in $\max(\gamma(k_z))$ at a fixed k_x due to the guide field is limited to a small fraction. The $\max(\gamma(k_x))$ is a monotonically decreasing function of k_z, i.e. increasing the wave number along the guide field direction always lowers the largest growth rate of the tearing mode. With the Hall effect, the presence of a guide field turns the linear $\omega - k_z$ relation, i.e. non-dispersive propagation along the guide field, into a non-monotonic curve. Moreover, at a certain k_x, if B_g is large enough, the peak of the $\omega(k_z)$ curve has a ω/k_z value independent of B_g, i.e. the fastest x-propagating mode has a phase speed along the guide field independent of the guide field strength. Last,

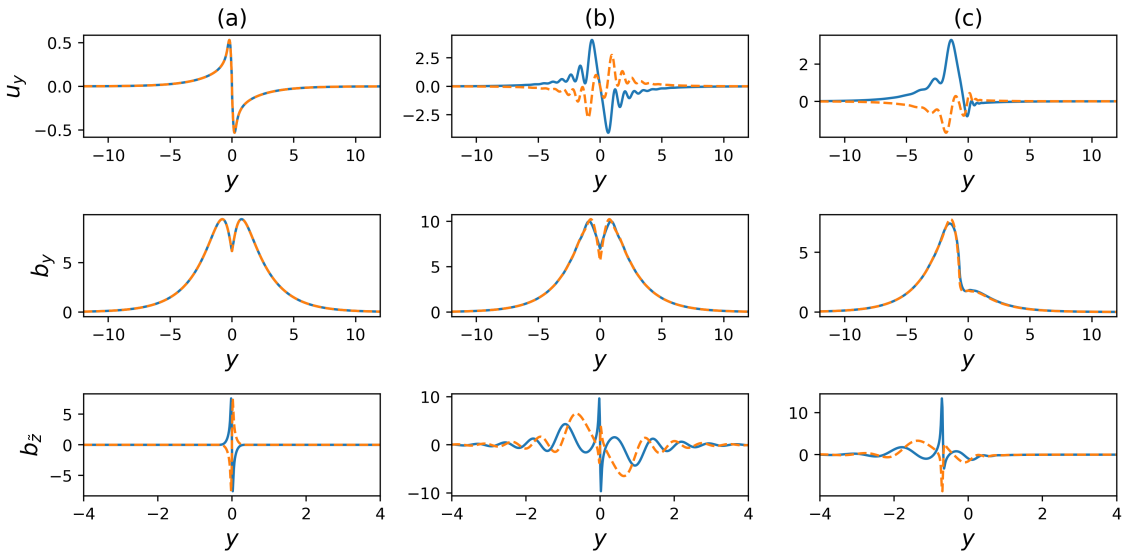

Figure 2.22: Solution of eigen-functions u_y (top row), b_y (middle row) and $b_{\tilde{z}}$ (bottom row) for $S = 10^4$, $d_i = 1.0$ and $k_x = 0.5$. Blue and orange curves are real and imaginary parts of each eigen-function. Left column (a) is for $k_z = 0$ and arbitrary B_g, middle column (b) is for $k_z = 0.06$ and $B_g = 0$, right column (c) is for $k_z = 0.06$ and $B_g = 5$.

with the Hall effect, the oblique tearing mode has a propagating component cross the current sheet (y direction) and this component is suppressed by a strong guide field.

2.4 Conclusion

In this chapter, we studied three problems related to tearing instability. The first one is how tearing instability is stabilized by the inhomogeneous background flow at low Lundquist numbers. We show that the background outflow stretches the growing magnetic islands and the stretching effect slows down the island growth. In addition, the magnetic islands are evacuated out of the current sheet within several Alfvén times and thus can only grow for a finite time. We estimate that the critical Lundquist number for the initial perturbation to grow by a factor no larger than 10^2 is $10^3 - 10^4$, consistent with nonlinear MHD simulations. In the second part of this chapter, we present nonlinear Hall-MHD simulations of reconnecting current sheet. We show that, as the scale of the current approaches ion inertial

length d_i from above, the recursive reconnection process is changed significantly. When d_i is much smaller than the inner layer thickness of the tearing mode δ_{TI}, the reconnection is purely plasmoid dominant. When d_i is much larger than δ_{TI} the reconnection becomes Hall-dominant where a single X-point is formed without plasmoid generation. When $d_i \lesssim \delta_{TI}$, an intermediate state is observed where a finite-size X-point is formed with plasmoids continuously ejected out from the X-point. In the last part of this chapter, we present results of linear stability analysis of tearing instability in a three-dimensional configuration with guide field and Hall effect. We show that the most unstable tearing mode is not changed by a strong guide field and is always the fastest growing parallel mode.

These works deepen our understanding of the fundamentals of tearing instability. However, there are still many questions that remain unsolved. For example, how does recursive reconnection proceed in a three-dimensional configuration with or without a guide field? To answer this question, high resolution 3D MHD simulations are necessary, which will be part of our future research.

CHAPTER 3

Turbulence in the Solar Wind

In this chapter, we present studies conducted on solar wind turbulence. In Section 3.1[1] we show simulation results on how stream interaction regions in the solar wind change the properties of Alfvénic fluctuations. In Section 3.2 we extend the simulations in Section 3.1 to include the heliospheric current sheet. We also carry out a superposed-epoch analysis using OMNI data on the turbulence properties around the current sheets at 1 AU. In Section 3.3 we present preliminary results of a statistical analysis of Parker Solar Probe data from its first four orbits. In Section 3.4, we conclude this chapter.

3.1 Propagation of Alfvén Waves in the Expanding Solar Wind with the Fast-slow Stream Interaction

3.1.1 Introduction

As discussed in Chapter 1, in the 1980s, with the Helios data, it was found that the energy spectra of the turbulence steepen toward the well-known Kolmogrov's 5/3 law or Iroshnikov-Kraichnan's 3/2 law (Iroshnikov, 1964; Kraichnan, 1965), indicating nonlinear processes in the evolution of the fluctuations (Bavassano et al., 1982). As inward propagating Alfvénic fluctuations are required for a nonlinear cascade in incompressible turbulence, understanding the generation and the propagation of the inward propagating Alfvén waves is crucial. Roberts et al. (1987a,b) analyzed the Voyager and Helios data and concluded that the dominance of the outward propagation weakens as the heliocentric distance increases. They

[1]This section is a version of (Shi et al., 2020)

also proposed that the outward propagating fluctuations are generated near the sun but the sheared streams in the solar wind accounts for the generation of the inward waves. Grappin et al. (1990) and Marsch & Tu (1990) studied the radial evolution and the properties of Alfvénic turbulence spectra and their dependence on various solar wind parameters by analyzing the Helios data by means of Elsässer variables. Roberts et al. (1992) carried out 2D incompressible MHD simulations with large-scale velocity shear and isotropic Alfvénic fluctuations. Their results showed that the velocity shear layer can produce a nonlinear cascade toward smaller scale fluctuations and the normalized cross helicity, i.e. the relative abundance of the outward propagating Alfvén waves, is decreased systematically at all wave numbers by the shear while the kinetic and magnetic energies remain approximately in equipartition. In addition to the sheared streams, the inhomogeneity of the large-scale solar wind structures due to the expansion of the solar wind leads to reflection of the outward propagating Alfvén waves and couples the outward and the inward waves linearly which may account for the decrease of the "Alfvénicity" (e.g. Velli et al., 1991; Velli, 1993).

Although analytical modeling of MHD turbulence has been developed significantly since the 1980s (e.g. Zhou & Matthaeus, 1990; Zank et al., 1996), limitations still exist in the models. First, various approximations must be made to close the moment equations. Whether the closures are physically correct is important and is often debatable. Second, all of the existing models deal with incompressible or nearly-incompressible turbulence while compressible effects may be important in the solar wind, especially in the fast-slow stream interaction regions. Third, the models are based on the two-scale separation method and thus the large-scale structure is not evolved self-consistently. In addition, the source terms generating the turbulence, e.g. the terms related with the velocity shear and the compressional effects, are only phenomenologically derived. Considering the drawbacks of models, it is good to adopt the direct numerical simulations as a method to study the turbulence since the simulation solves the physical system self-consistently and can be fully compressible. However, vast computational capacity is required in order to fully simulate the turbulence evolution inside the heliosphere due to the huge separation of spatial scales. Various methods were devel-

oped therefore with the aim of reducing the computational cost while still including relevant effects due to the global solar wind dynamics. The expanding box model (EBM) (Grappin & Velli, 1996; Tenerani & Velli, 2017), which by tracking a box co-moving with the radial mean flow, neglecting the high-order curvature terms, allows one to simulate the nonlinear evolution of the waves and turbulence and the stream structures with the expansion effect taken into consideration.

In this work, we carry out 2D MHD simulations based on the expanding box model to study the propagation of Alfvén waves and the evolution of the turbulence in the inner heliosphere. Especially, we focus on the effects of the evolving fast-slow stream interaction present in the simulations. The simulation parameters are chosen to be close to the real solar wind conditions. We inspect the radial evolution and the longitudinal variation of some parameters that are important in the MHD turbulence study, i.e. the energy in the Elsässer variables, the normalized cross helicity and the normalized residual energy. We show that all of the parameters are significantly affected by the velocity shear and the compression between the streams. We also investigate the power spectra of the Elsässer variables. This section is organized as follows. In Section 3.1.2, we describe the numerical method that is used in this study and the setup of the simulations. In Section 3.1.3 we present the simulation results. In Section 3.1.4 we summarize this study.

3.1.2 Numerical method

In this section we describe the numerical method, i.e. the corotating expanding box model, in Section 3.1.2.1 & 3.1.2.2 and then present the initial setup and the choice of parameters in Section 3.1.2.3.

3.1.2.1 Expanding Box Model in Conservation Form

The derivation of the expanding box model based on the convective form of the MHD equation is well described in previous papers (e.g. Grappin et al., 1993; Grappin & Velli, 1996). The idea is to break the velocity **U** into two parts: the radial mean flow and the

velocity in the frame of the mean flow:

$$\mathbf{U} = U_0 \hat{e}_r + \mathbf{u} \tag{3.1}$$

where U_0 is the constant radial speed. Simulation domain is a thin box (small radial extent) co-moving with the mean flow and the (normalized) expanding coordinate system $(\tilde{x}, \tilde{y}, \tilde{z})$ transforms from the inertial coordinates by

$$\tilde{x} = x - R(t),\ \tilde{y} = \frac{R_0}{R(t)} y,\ \tilde{z} = \frac{R_0}{R(t)} z \tag{3.2}$$

where $R(t) = R_0 + U_0 t$ such that the derivatives are

$$\frac{\partial}{\partial x} = \frac{\partial}{\partial \tilde{x}},\ \frac{\partial}{\partial y} = \frac{R_0}{R(t)} \frac{\partial}{\partial \tilde{y}},\ \frac{\partial}{\partial z} = \frac{R_0}{R(t)} \frac{\partial}{\partial \tilde{z}} \tag{3.3}$$

Inside the expanding box, the mean flow can be written, by neglecting the high-order curvature terms, as

$$U_0 \hat{e}_r \approx U_0 \left[\hat{e}_x + \frac{y}{R(t)} \hat{e}_y + \frac{z}{R(t)} \hat{e}_z \right] \tag{3.4}$$

Plugging Eq (3.4) into the MHD equation gives the EBM equation set

$$\frac{\partial \rho}{\partial t} = -\nabla \cdot (\rho \mathbf{u}) - \frac{2}{\tau} \rho \tag{3.5a}$$

$$\frac{\partial \mathbf{u}}{\partial t} = -\mathbf{u} \cdot \nabla \mathbf{u} - \frac{1}{\rho} \nabla \left(p + \frac{1}{2} B^2 \right) + \frac{1}{\rho} \mathbf{B} \cdot \nabla \mathbf{B} - \frac{1}{\tau} \begin{pmatrix} 0 & 0 & 0 \\ 0 & 1 & 0 \\ 0 & 0 & 1 \end{pmatrix} \mathbf{u} \tag{3.5b}$$

$$\frac{\partial \mathbf{B}}{\partial t} = \nabla \times (\mathbf{u} \times \mathbf{B}) - \frac{1}{\tau} \begin{pmatrix} 2 & 0 & 0 \\ 0 & 1 & 0 \\ 0 & 0 & 1 \end{pmatrix} \mathbf{B} \tag{3.5c}$$

$$\frac{\partial p}{\partial t} = -\mathbf{u} \cdot \nabla p - \kappa \left(\nabla \cdot \mathbf{u} \right) p - \frac{2\kappa}{\tau} p \tag{3.5d}$$

where κ is the adiabatic index and $\tau = R(t)/U_0$ is the solar wind expansion time. Eq (3.5) is very similar to the normal MHD equation set except for: (1) The velocity field is in the reference frame of the radial mean flow. (2) New terms with the expansion time τ are

introduced by the radial mean flow and they represent the expansion effect. A more detailed discussion of the EBM properties can be found in (Grappin & Velli, 1996).

For the conservation-form of the MHD equation, care must be taken on the expansion terms. The expansion terms for the density and magnetic field equations remain unchanged as in Eq (3.5) but not for the momentum and energy equations. Take the momentum equation as an example. Because the left-hand-side of the momentum equation can be written as

$$\frac{\partial(\rho\mathbf{u})}{\partial t}+\nabla\cdot(\rho\mathbf{u}\mathbf{u})=\left[\rho\left(\frac{\partial\mathbf{u}}{\partial t}+\mathbf{u}\cdot\nabla\mathbf{u}\right)\right]+\left[\frac{\partial\rho}{\partial t}+\nabla\cdot(\rho\mathbf{u})\right]\mathbf{u} \tag{3.6}$$

the expansion term consists of the part that comes from the velocity equation (Eq (3.5b)) and that from the density equation (Eq (3.5a)):

$$E_m=-\frac{1}{\tau}\begin{pmatrix}0&0&0\\0&1&0\\0&0&1\end{pmatrix}\rho\mathbf{u}-\frac{2}{\tau}\rho\mathbf{u}=-\frac{1}{\tau}\begin{pmatrix}2&0&0\\0&3&0\\0&0&3\end{pmatrix}\rho\mathbf{u} \tag{3.7}$$

Similarly, one can show that the expansion term of the energy equation

$$\frac{\partial e}{\partial t}=-\nabla\cdot\left[\left(e+p+\frac{1}{2}B^2\right)\mathbf{u}-(\mathbf{u}\cdot\mathbf{B})\,\mathbf{B}\right] \tag{3.8}$$

where $e=\frac{p}{\kappa-1}+\frac{1}{2}\rho u^2+\frac{1}{2}B^2$, is

$$E_e=-2\frac{\kappa}{\kappa-1}\frac{p}{\tau}-\frac{\rho}{\tau}\left(u_x^2+2u_y^2+2u_z^2\right)-\frac{1}{\tau}\left(2B_x^2+B_y^2+B_z^2\right) \tag{3.9}$$

In summary, *the EBM equation set in conservation form* is

$$\frac{\partial\rho}{\partial t}=-\nabla\cdot(\rho\mathbf{u})-\frac{2}{\tau}\rho \tag{3.10a}$$

$$\frac{\partial(\rho\mathbf{u})}{\partial t}=-\nabla\cdot\left[\rho\mathbf{u}\mathbf{u}+\left(p+\frac{1}{2}B^2\right)\mathbf{I}-\mathbf{B}\mathbf{B}\right]-\frac{1}{\tau}\begin{pmatrix}2&0&0\\0&3&0\\0&0&3\end{pmatrix}\rho\mathbf{u} \tag{3.10b}$$

$$\frac{\partial \mathbf{B}}{\partial t} = \nabla \times (\mathbf{u} \times \mathbf{B}) - \frac{1}{\tau} \begin{pmatrix} 2 & 0 & 0 \\ 0 & 1 & 0 \\ 0 & 0 & 1 \end{pmatrix} \mathbf{B} \tag{3.10c}$$

$$\begin{aligned} \frac{\partial e}{\partial t} &= -\nabla \cdot \left[\left(e + p + \frac{1}{2} B^2 \right) \mathbf{u} - (\mathbf{u} \cdot \mathbf{B}) \, \mathbf{B} \right] \\ &- \frac{1}{\tau} \left[\frac{2\kappa}{\kappa - 1} p + \rho \left(u_x^2 + 2u_y^2 + 2u_z^2 \right) + \left(2B_x^2 + B_y^2 + B_z^2 \right) \right] \end{aligned} \tag{3.10d}$$

with

$$e = \frac{p}{\kappa - 1} + \frac{1}{2} \rho u^2 + \frac{1}{2} B^2 \tag{3.11}$$

3.1.2.2 Corotating Expanding Box

As explained by (Grappin & Velli, 1996), in order to simulate the compression between fast and slow streams, we need to rotate the expanding box coordinates by a small angle α such that the new coordinate system $\mathbf{x}'$ is

$$\begin{pmatrix} x' \\ y' \\ z' \end{pmatrix} = \begin{pmatrix} \cos\alpha & -\sin\alpha & 0 \\ \sin\alpha & \cos\alpha & 0 \\ 0 & 0 & 1 \end{pmatrix} \begin{pmatrix} \tilde{x} \\ \tilde{y} \\ \tilde{z} \end{pmatrix} \tag{3.12}$$

The angle α is constant and is the initial inclination of the interface between the fast and slow streams with respect to the radial direction. The initial condition for the stream structure is

$$\mathbf{u_0} = u_0(y')\hat{e}_{\tilde{x}}, \; \rho_0 = \rho_0(y') \tag{3.13}$$

i.e. the velocity is along the radial direction but varies with y' instead of y so that compression is induced. The temperature of the stream $T_0 = T_0(y')$ such that $p_0 = \rho_0 T_0$ is uniform.

We should point out that, although the coordinates $\mathbf{x}'$ are orthogonal at the beginning, they do not remain orthogonal as the box expands unless $\alpha = 0$, as illustrated in the left panel of Figure 3.1. The black axes show the normal expanding box coordinates with $\hat{e}_x$ aligned with the radial direction and $\hat{e}_y$ along the azimuthal (φ) direction. The solid red

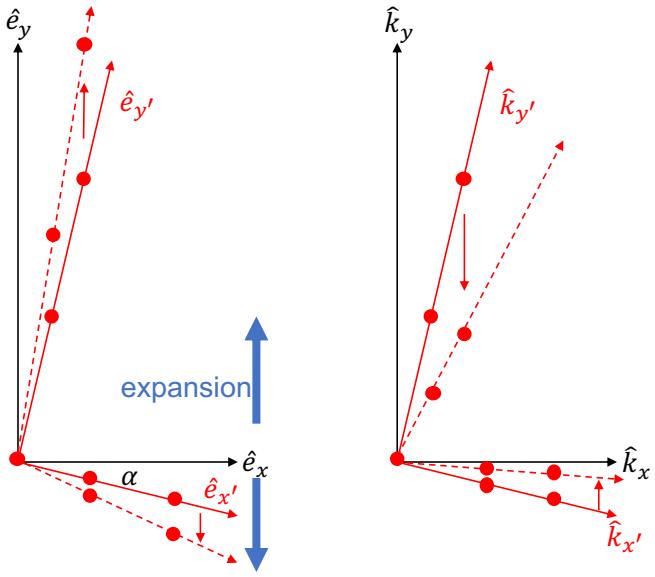

Figure 3.1: Illustration of the deformation of the corotating expanding box coordinates $\mathbf{x}'$ (left) and the wave vector $\mathbf{k}_{\mathbf{x}'}$ (right). Black axes are the normal expanding box coordinates (wave vectors) with $\hat{e}_x$ ($\hat{k}_x$) to be radial. The solid red axes represent the initial state of the corotating coordinates $\mathbf{x}'$ (wave vectors $\mathbf{k}_{\mathbf{x}'}$) which is orthogonal. The red dots represent mesh gridpoints in the simulation domain. The dashed red lines are axes $\hat{e}_{x'}$ ($\hat{k}_{x'}$) and $\hat{e}_{y'}$ ($\hat{k}_{y'}$) after the simulation starts.

axes represent the initial state of the corotating expanding box coordinates $\mathbf{x}'$, an orthogonal coordinate system rotated by an angle α with respect to the radial direction. The red dots represent a few mesh points in the simulation domain. Due to the expansion along the φ direction, both the $\hat{e}_{x'}$ and $\hat{e}_{y'}$ turn away from the radial axis, as shown by the dashed red axes. That is to say, the angle between $\hat{e}_{x'}$ and $\hat{e}_{y'}$ becomes larger than $\pi/2$ after the simulation starts. A positive aspect of this frame is that, if we set the initial magnetic field to be aligned with $\hat{e}_{x'}$

$$\mathbf{B_0} = B_0(y')\hat{e}_{x'} \tag{3.14}$$

it will remain aligned with $\hat{e}_{x'}$ for all time. Thus, in all the simulations we set up $\mathbf{B_0}$ as like Eq (3.14) and we will call $\hat{e}_{x'}$ the parallel direction hereinafter. Note that, although the axes in real space are turned away from the radial direction, the wave vectors are actually turned

toward the radial direction (right panel of Figure 3.1) due to the increase of the grid spacing in y.

The code operates mainly in the Fourier space $(k_{x'}, k_{y'})$. A third-order Runge-Kutta method is used for time integration. Vectors remain defined in the $(\hat{e}_{\tilde{x}}, \hat{e}_{\tilde{y}}, \hat{e}_{\tilde{z}})$ directions although the mesh grid is on (x', y'). At each time step, fluxes are calculated in real space first and then Fourier transformed. Time advance is done in Fourier space and we need the following projection in order to transform the derivatives on $(x',\, y')$ to the derivatives on $(x,\, y)$:

$$\begin{aligned} k_x &= k_{x'} \cos\alpha + k_{y'} \sin\alpha \\ k_y &= \frac{R_0}{R(t)} \left(-k_{x'} \sin\alpha + k_{y'} \cos\alpha\right) \end{aligned} \tag{3.15}$$

$\nabla \cdot \mathbf{B} = 0$ is automatically preserved by this algorithm. Because we are interested in the evolution of turbulence, rather than heating or plasma thermodynamics, we apply a smooth numerical filter to all fields to ensure proper de-aliasing rather than explicit viscosity or resistivity. The filter is defined in Fourier space:

$$\hat{\mathbf{f}}(k_{x'}, k_{y'}) = \mathbf{f}(k_{x'}, k_{y'}) \times T(k_{x'}) \times T(k_{y'}) \tag{3.16}$$

where $\mathbf{f}$ is the field before filtering and $\hat{\mathbf{f}}$ is the field after filtering. The function $T(k)$ is the same as the fourth-order filter of the compact finite difference scheme (Eq (C.2.2) and (C.2.4) of (Lele, 1992)) with constraints $\beta = d = 0$

$$T(k) = \frac{a + b\cos(w) + c\cos(2w)}{1 + 2\lambda\cos(w)} \tag{3.17}$$

where $w = 2\pi k\Delta \in [-\pi,\, \pi]$ is the normalized wave number (Δ is the grid spacing) and $a = (5 + 6\lambda)/8$, $b = (1 + 2\lambda)/2$, $c = -(1 - 2\lambda)/8$ with λ to be a free parameter in the range $[-0.5, 0.5]$ (refer to Fig. 19 of (Lele, 1992) for the shape of $T(k)$). $\lambda = 0.5$ corresponds to no filtering at all. In our simulations we set $\lambda = 0.45$ such that the numerical stability is ensured without too much numerical dissipation.

3.1.2.3 Initial Setup and Parameters

The initial condition consists of the large scale stream structure and the Alfvén waves. As mentioned in Section 3.1.2.2, the stream structure is of the form

$$\mathbf{u_0} = u_0(y')\hat{e}_{\tilde{x}},\ \rho_0 = \rho_0(y'),\ \mathbf{B_0} = B_0(y')\hat{e}_{x'} \tag{3.18}$$

with double-tanh profiles for u_0 and ρ_0:

$$u_0(y') = \begin{cases} \frac{1}{2}\left[(u_f + u_s) + (u_f - u_s)\tanh\left(\frac{y' - \frac{1}{4}L_{y'}}{a}\right)\right], & y' < \frac{L_{y'}}{2} \\ \frac{1}{2}\left[(u_f + u_s) - (u_f - u_s)\tanh\left(\frac{y' - \frac{3}{4}L_{y'}}{a}\right)\right], & y' \geq \frac{L_{y'}}{2} \end{cases} \tag{3.19a}$$

$$\rho_0(y') = \begin{cases} \frac{1}{2}\left[(\rho_f + \rho_s) + (\rho_f - \rho_s)\tanh\left(\frac{y' - \frac{1}{4}L_{y'}}{a}\right)\right], & y' < \frac{L_{y'}}{2} \\ \frac{1}{2}\left[(\rho_f + \rho_s) - (\rho_f - \rho_s)\tanh\left(\frac{y' - \frac{3}{4}L_{y'}}{a}\right)\right], & y' \geq \frac{L_{y'}}{2} \end{cases} \tag{3.19b}$$

and a uniform magnetic field

$$B_0(y') = B_0 \tag{3.20}$$

in all the simulations. The width of the shear region is $a = 0.075L_{y'}$ with $L_{y'}$ to be the size of the simulation domain along $\hat{e}_{y'}$. u_s, u_f, ρ_s, ρ_f are the speeds and densities for the slow and fast streams respectively. For all the runs, the initial location of the simulation domain is

$$R_0 = 30R_s = 0.14\text{AU} \tag{3.21}$$

where R_s is the solar radius and the size of the domain is

$$L_{x'} \times L_{y'} = 10R_s \times \pi R_0 \tag{3.22}$$

i.e. the domain is a half-circle in the ecliptic plane. The initial spiral angle α, if not zero, is set to be

$$\alpha = 0.142 \tag{3.23}$$

so that at 1 AU the spiral angle is around $\pi/4$, in accordance with the observation. The strength of the magnetic field is $B_0 = 250\,\text{nT}$ so that at 1 AU $B_r \approx B_\varphi \approx 5\,\text{nT}$. The densities of the slow and fast streams are $n_s = 360\,\text{cm}^{-3}$ and $n_f = 140\,\text{cm}^{-3}$. The speeds of

the slow and fast streams are $u_s = 340\,\mathrm{km/s}$ and $u_f = 700\,\mathrm{km/s}$ and the mean radial speed is $U_0 = 464\,\mathrm{km/s}$. The thermal pressure is $p_0 = 5\,\mathrm{nPa}$ so that the temperatures of the slow and fast streams are $T_s = 1.0 \times 10^6\,\mathrm{K}$ and $T_f = 2.6 \times 10^6\,\mathrm{K}$. The adiabatic index is $\kappa = 3/2$ instead of $\kappa = 5/3$ to prevent the plasma from cooling down too fast. Note that the radial decay of the temperature due to expansion obeys $T \propto R^{-2(\kappa-1)}$ so that with $\kappa = 3/2$ the temperatures of the slow and fast streams at 1 AU are $T_s = 1.4 \times 10^5\,\mathrm{K}$ and $T_f = 3.6 \times 10^5\,\mathrm{K}$. The normalization units are: $\bar{B} = 250\,\mathrm{nT}$, $\bar{n} = 200\mathrm{cm}^{-3}$ and $\bar{L} = R_s$ which lead to the unit speed $\bar{U} = \bar{B}/\sqrt{\mu_0 m_i \bar{n}} = 385.6\,\mathrm{km/s}$ and unit pressure $\bar{p} = \bar{n} m_i \bar{U}^2 = 49.7\,\mathrm{nPa}$ where m_i is the proton mass.

We add circularly-polarized Alfvénic wave bands on top of the stream structure:

$$\begin{aligned} \mathbf{b_{1,o}} &= \delta b \sum_{N=1}^{N_{max}} \frac{1}{\sqrt{N}} \left[\cos\left(\frac{2\pi N}{L_{x'}} x' + \phi_{N,o} \right) \hat{e}_{y'} + \sin\left(\frac{2\pi N}{L_{x'}} x' + \phi_{N,o} \right) \hat{e}_z \right], \\ \mathbf{u_{1,o}} &= -\frac{\mathbf{b_{1,o}}}{\sqrt{\rho_0(y')}} \end{aligned} \tag{3.24a}$$

$$\begin{aligned} \mathbf{b_{1,i}} &= r_{io} \times \delta b \sum_{N=1}^{N_{max}} \frac{1}{\sqrt{N}} \left[\cos\left(\frac{2\pi N}{L_{x'}} x' + \phi_{N,i} \right) \hat{e}_{y'} + \sin\left(\frac{2\pi N}{L_{x'}} x' + \phi_{N,i} \right) \hat{e}_z \right], \\ \mathbf{u_{1,i}} &= \frac{\mathbf{b_{1,i}}}{\sqrt{\rho_0(y')}} \end{aligned} \tag{3.24b}$$

Here δb is the amplitude of the magnetic perturbation of the outward wave, r_{io} is the ratio between the amplitudes of inward and outward waves, $\phi_{N,o}$ and $\phi_{N,i}$ are the random phases of mode N of outward and inward waves. The slope of the power spectrum of the wave band is -1. In order to make sure $\nabla \cdot \mathbf{b_1} = 0$, $\mathbf{b_1}$ is invariant along y' and $\mathbf{u_1}$ varies with y' due to the non-uniform density. This leads to the inhomogeneity of the Alfvén wave energy along y' direction: the wave energy is larger in the fast stream than the slow stream. Five 2D runs are carried out and they are listed in Table 3.1. By choosing the parameter δb, the total energies in the waves are invariant among the runs. We fix $N_{max} = 16$ in all the simulations. The maximum simulation time is $t = 200$, corresponding to a radial distance $R = 270.9 R_s = 1.26\,\mathrm{AU}$. The resolution is $n_{x'} \times n_{y'} = 2048 \times 4096$. In addition, we also make a 1D run ($L_{y'} = \pi R_0$ and $n_{y'} = 1024$) without adding waves to show the evolution of the stream structure up to $R = 400 R_s$.

Run	Expansion	Corotation	r_{io}	δb
A0	N	N	0.2	0.2
A	Y	N	0.2	0.2
B	Y	Y	0.2	0.2
C	Y	Y	1.0	0.144
D	Y	Y	5.0	0.04

Table 3.1: Parameters of the 2D runs. Here r_{io} is the ratio between the amplitude of the inward waveband and the amplitude of the outward waveband. δb is the amplitude of the outward waveband and the five runs have the same total wave energies. If expansion is present, the radial mean speed $U_0 = 1.2$. If corotation is present, the initial spiral angle $\alpha = 0.142$.

3.1.3 Results

3.1.3.1 1D Run without Waves

In this section we show a 1D test simulation of the stream structure without adding any waves. This run serves as a test of the code. For convenience, we refer to $y'/L_{y'}$ as the normalized "longitude" hereinafter although $\hat{e}_{y'}$ is not exactly along the azimuthal direction $\hat{e}_y$. Figure 3.2 shows the radial evolution of the longitudinal profiles of the radial velocity u_x, the azimuthal velocity u_y, the density ρ, the pressure p and the magnitude of the magnetic field $|B|$ (from top to bottom rows). The left, middle and right columns are snapshots at $R = 30.0R_s$, $218.0R_s$ & $401.1R_s$ respectively. At around 1 AU (middle column), a clear compression region already forms. The flows are deflected away from the interface between fast and slow streams. The density, pressure and magnetic field peak around the compression region. Further out, a forward-backward shock pair, which bounds the compression region, forms as shown in the right column. The results, shown in Figure 3.2, are consistent with (Grappin & Velli, 1996) and may be benchmarked against their Figure 3.

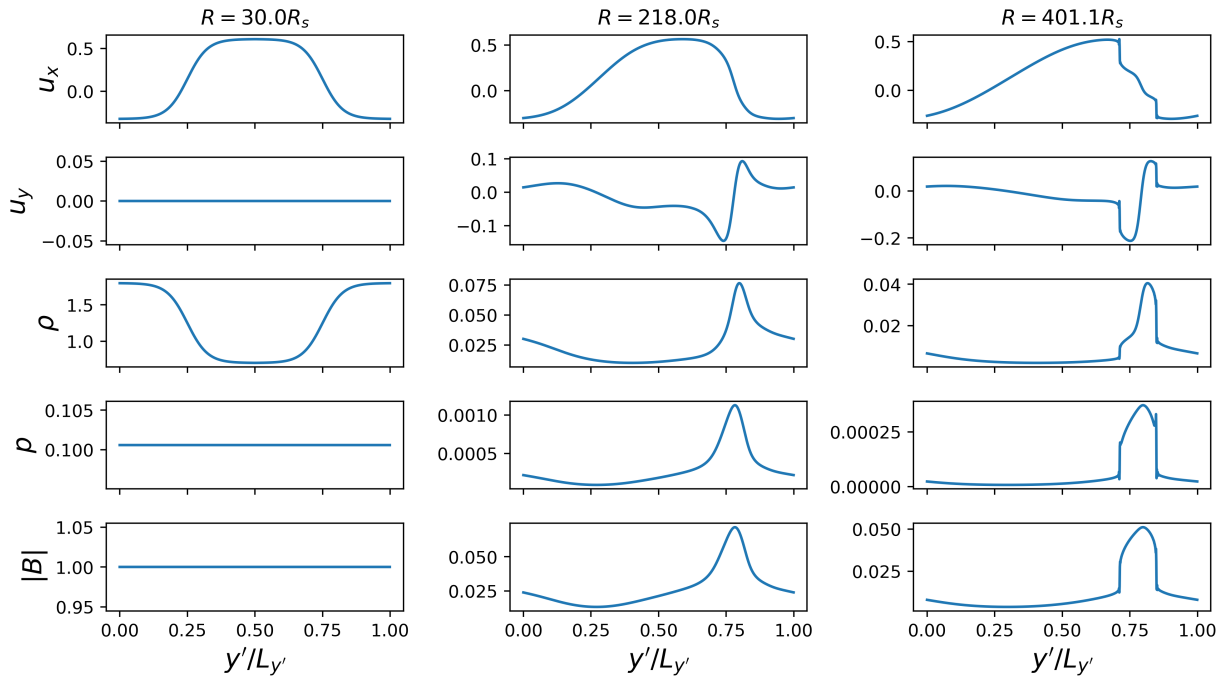

Figure 3.2: 1D simulation of the large-scale stream structure. From top to bottom rows are longitudinal (y') profiles of the radial velocity, the azimuthal velocity, the density, the pressure and the magnitude of magnetic field respectively. From left to right columns are the snapshots at $R = 30.0R_s$, $218.0R_s$, $401.1R_s$.

3.1.3.2 Diagnostics of the Alfvénic turbulence

Before presenting the results of the 2D simulations, we first introduce the diagnostics adopted for the analysis of the simulation data.

The analysis is mainly based on the perturbed Elsässer variables $\mathbf{z_{out}}$ and $\mathbf{z_{in}}$. The procedure to calculate them is described as follows. We first calculate the x'-averaged, i.e. the background, magnetic and velocity fields:

$$\mathbf{B_0}(y') = \frac{1}{L_{x'}} \int_0^{L_{x'}} \mathbf{B}(x', y') dx', \quad \mathbf{u_0}(y') = \frac{1}{L_{x'}} \int_0^{L_{x'}} \mathbf{u}(x', y') dx' \tag{3.25}$$

and then the perturbed magnetic and velocity fields:

$$\mathbf{b_1}(x', y') = \mathbf{B}(x', y') - \mathbf{B_0}(y'), \quad \mathbf{u_1}(x', y') = \mathbf{u}(x', y') - \mathbf{u_0}(y') \tag{3.26}$$

The Elsässer variables are then calculated by

$$\mathbf{z_{out}} = \mathbf{u_1} - \mathrm{sign}(B_{0x})\frac{\mathbf{b_1}}{\sqrt{\rho}}, \quad \mathbf{z_{in}} = \mathbf{u_1} + \mathrm{sign}(B_{0x})\frac{\mathbf{b_1}}{\sqrt{\rho}} \tag{3.27}$$

where $\mathrm{sign}(B_{0x})$ is the sign of the radial background magnetic field. Note that the density is not x'-averaged but the local density. We further project the Elsässer variables defined by Eq (3.27) into three directions: the out-of-plane direction $\hat{e}_z$, the parallel-to-$\mathbf{B_0}$ direction $\hat{e}_{x'}$, and the in-plane perpendicular-to-$\mathbf{B_0}$ direction $\hat{e}_\perp = \hat{e}_z \times \hat{e}_{x'}$. In the analysis hereinafter, we only deal with the z-component and the perpendicular component and exclude the parallel component. At a certain time t, various energies as functions of y' are calculated by integrating along the x' direction, e.g. the outward Elsässer energy:

$$E_{out}(y', t) = \frac{1}{2}\int_{x'} \left(z^2_{out,z} + z^2_{out,\perp}\right) \tag{3.28}$$

The total energy, the normalized cross helicity and the normalized residual energy are then calculated by

$$E^T = E_{out} + E_{in}, \quad \sigma_c = \frac{E_{out} - E_{in}}{E_{out} + E_{in}}, \quad \sigma_r = \frac{E_u - E_b}{E_u + E_b} \tag{3.29}$$

The kinetic and magnetic energies are those in the perturbations $\mathbf{u_1}$ and $\mathbf{b_1}$ and we do not include the parallel component in calculating σ_r. We have verified that including the parallel component in E_u and E_b does not make a significant difference. The normalized density perturbation $\delta\rho/\rho$ is the root-mean-square value of ρ along x' divided by the x'-averaged density ρ_0:

$$\frac{\delta\rho}{\rho}(y', t) = \frac{1}{\rho_0(y', t)}\sqrt{\frac{1}{L_{x'}}\int_{x'} \left[\rho(x', y', t) - \rho_0(y', t)\right]^2} \tag{3.30}$$

Power spectra of $\mathbf{z_{out}}$ and $\mathbf{z_{in}}$ are calculated along $\hat{e}_{x'}$ and $\hat{e}_{y'}$ by applying Fourier transform to the z and perpendicular components of them, e.g. $E_{out,z}\left(k_{x'}, y', t\right) = \left|\mathcal{F}_{x'}\left(z_{out,z}\right)\right|^2$ where $\mathcal{F}_{x'}$ is the Fourier transform in coordinate x'. When we present the spectra, we further average the spectra along the non-Fourier-transformed coordinates to eliminate the strong oscillations. The details of the averaging procedure of the spectra will be discussed later.

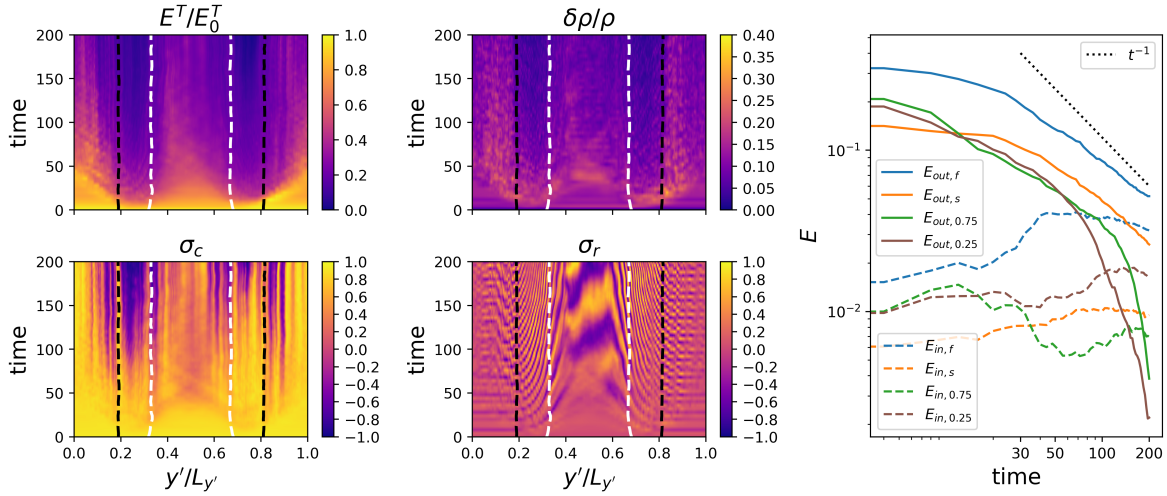

Figure 3.3: Results of Run A0. The left two columns are the $y' - t$ contours of the total Elsässer energy E^T/E_0^T where E_0^T is $E^T(t = 0)$ (top-left), the normalized density perturbation $\delta\rho/\rho$ (top-middle), the normalized cross-helicity σ_c (bottom left) and the normalized residual energy σ_r (bottom middle). White dashed lines mark the longitudes where the x'-averaged radial speed u_{0x} equals 650 km/s and black dashed lines mark the longitudes where the x'-averaged radial speed u_{0x} equals 400 km/s. Right panel shows the time evolution of the Elsässer energies in log-log scale where solid/dashed curves are the outward/inward waves and blue, orange, green and brown represent fast stream ("f"), slow stream ("s"), shear region around $y' = 0.75L_{y'}$ and shear region around $y' = 0.25L_{y'}$. The black dotted line is $E \propto t^{-1}$ for reference.

3.1.3.3 Run A0: no corotation, no expansion, outward-dominant waves

In Run A0, the background fields are radial, i.e. there is no compression and rarefaction. Besides, the expansion effect is turned off. The initial condition consists of the outward-dominant Alfvén wave band. The result of Run A0 is shown in Figure 3.3.

The top-left panel shows the $y' - t$ contour of the total Elsässer energy E^T/E_0^T where E_0^T is $E^T(t = 0)$. The white dashed lines mark y' where u_{0x} equals 650 km/s and the black dashed lines mark y' where u_{0x} equals 400 km/s (the same in the other three contours). We

see that the total Elsässer energy E^T at all longitudes decays with time while in the shear region the energy decays much faster. The right panel of Figure 3.3 shows the time evolution of the Elsässer energies of the outward wave (solid curves) and inward wave (dashed curves) averaged in different regions bounded by the white and black dashed lines in the contours, i.e. the fast stream (blue), the slow stream (orange), the shear region around $y' = 0.75L_{y'}$ (green) and the shear region around $y' = 0.25L_{y'}$ (brown). The black dotted line is $E \propto t^{-1}$ for reference. The evolution of the wave energies inside the fast and slow streams is similar: the outward wave energy decays with time at a rate slower than t^{-1} and the inward wave energy increases with time slightly. Inside the shear regions, the outward wave energy decays slower than t^{-1} first and the decay rate is similar to that of the outward wave inside the fast/slow streams. However, after some time ($t \gtrsim 100$ in the shear region around $y' = 0.75L_{y'}$ and $t \gtrsim 70$ in the shear region around $y' = 0.25L_{y'}$) the wave energy starts to drop very fast. The inward wave energy grows slowly at the beginning, followed by a drop at $t \approx 30$ and then starts to grow again in the two shear regions. Note that in the shear region at $y' \approx 0.75L_{y'}$, the drop of the inward wave energy is stronger than that in the shear region at $y' \approx 0.25L_{y'}$. Here we must point out that the initial configuration, although symmetric in y', does not evolve symmetrically because the y'-gradients of the background fields are of opposite signs while the initial perturbations along y' (e.g. $u_{1y'}$) do not change sign at the two shear regions. This, for example, will lead to an increase of ρ at one shear region and a decrease of ρ at the other one.

The top-middle panel of Figure 3.3 shows the $y' - t$ contour of the relative density fluctuation $\delta\rho/\rho$. The value of $\delta\rho/\rho$ remains small ($\lesssim 0.2$) throughout the simulation. The largest density fluctuation $\delta\rho$ is found to be inside the slow stream near the boundaries of the shear regions, as can be seen from the contour. The bottom-left panel displays the $y' - t$ contour of the normalized cross-helicity σ_c, which decays with distance in all the flow regions. The decay rate is largest inside the shear region at $y' \approx 0.25L_{y'}$ where σ_c almost reaches -1 at the end of the simulation. This can also be seen from the right column of Figure 3.3 which shows that the outward Elsässer energy is one order of magnitude smaller than the

inward energy in the shear region at $y' \approx 0.25L_{y'}$ at the end of the simulation. A notable phenomenon is the stripe structures in the contour of σ_c, showing that σ_c decays much faster within some narrow channels in y' compared to the ambient streams. The evolution of σ_c we find is very similar to that in the incompressible simulation by Roberts et al. (1992) (see their Figure 12). The bottom-middle panel shows the $y' - t$ contour of the normalized residual energy σ_r. Strong oscillations are observed. On average σ_r is 0 but the instant amplitude can be as large as $\simeq 1$. The oscillation of σ_r is strongest inside the shear regions due to the large longitudinal gradient of the relative speed between the counter-propagating waves. A trend of increasing of $|\sigma_r|$ in some regions, e.g. the fast stream and the shear regions, is also seen. This is because of the decrease of $|\sigma_c|$: if $\sigma_c = 0$, the inward and outward waves are of the same amplitude and thus $|\sigma_r|$ will be equal to 1 if the two populations of waves are non-correlated. Actually, we can see that at $y' \approx 0.25L_{y'}$, $|\sigma_r|$ increases at $t \lesssim 150$ and then starts to drop, which is anti-correlated with $|\sigma_c|$.

3.1.3.4 Run A: no corotation, expansion, outward-dominant waves

In this subsection, we present the results of Run A ($\alpha = 0$, $r_{io} = 0.2$ and $\delta b = 0.2$), where the compression between the fast and slow streams is absent but the expansion effect is turned on.

Figure 3.4 shows the contours of the out-of-plane component of the outward Elsässer variable $z_{out,z}$ at three radial distances: $R = 30.0R_s$, $107.1R_s$ & $217.9R_s$. From Figure 3.4, it is clearly seen that the differential radial flow leads to the phase-mixing of the Alfvén waves, the wave vector of which is tilted from $\hat{e}_{x'}$ toward $\hat{e}_{y'}$. The strongest phase-mixing happens in the regions where the velocity shear is the largest (around $y' = 0.75L_{y'}$ and $y' = 0.25L_{y'}$). The dissipation of waves is observed at these regions since the phase-mixing transfers the wave energy to small scales where the numerical dissipation is strong. For other Elsässer variables, i.e. $z_{out,\perp}$, $z_{in,z}$ and $z_{in,\perp}$, similar evolution is also observed.

Figure 3.5 displays the $y' - R$ contours of the total Elsässer energy E^T/E_0^T compensated by R/R_0 where E_0^T is E^T at $t = 0$ (top-left), the relative density fluctuation $\delta\rho/\rho$ (top-

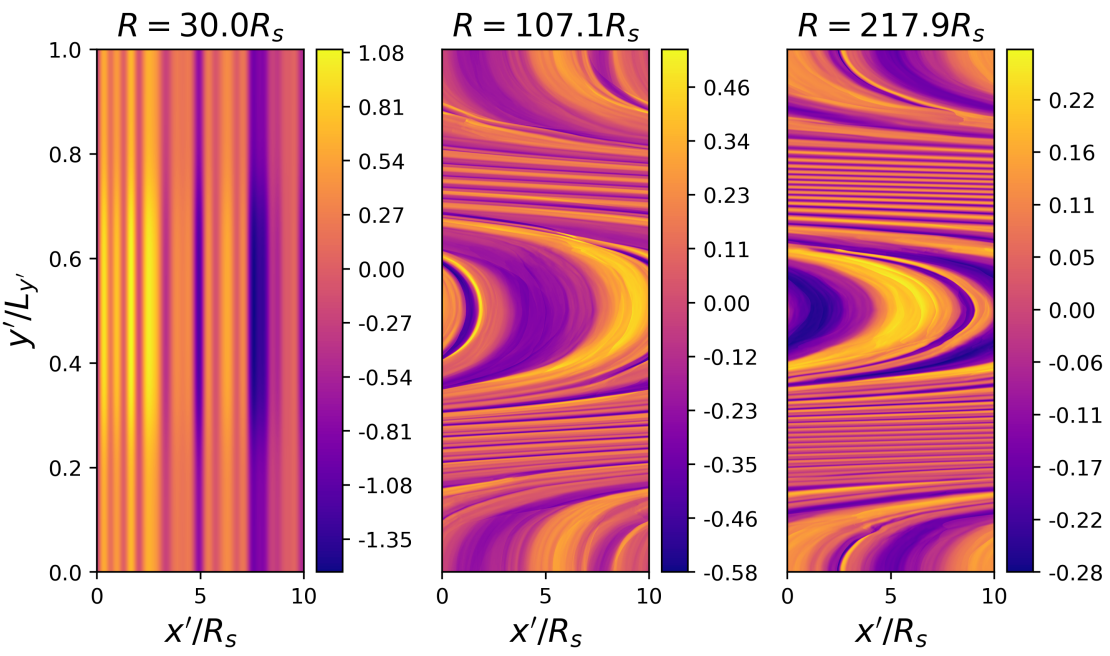

Figure 3.4: Contours of the z-component of the outward Elsässer variable $z_{out,z}$ at $R = 30.0R_s$, $107.1R_s$ & $217.9R_s$ in Run A.

right), the normalized cross-helicity σ_c (bottom-left) and the normalized residual energy σ_r (bottom-right), similar to Figure 3.3 but note that the y-axis is now radial distance instead of time. The white dashed lines mark $y'(R)$ where the x'-averaged radial speed u_{0x} equals 650 km/s and the black dashed lines mark $y'(R)$ where u_{0x} equals 400 km/s. The decay of E^T is in general faster than $1/R$, the WKB prediction of the Alfvén waves in the spherical geometry (Belcher, 1971). Similar to Run A0, it clearly shows a longitudinal variation: inside the fast and slow streams, the decay is slower than in the shear regions. The relative density fluctuation $\delta\rho/\rho$ is smaller than 0.2 most of the time and it is smaller inside the shear regions compared with the fast and slow streams. It is also observed that some density structures are generated near the boundaries between the shear regions and the slow stream and propagate along the y' direction. The most significant one starts at $R \approx 60R_s$ and $y' \approx 0.8L_{y'}$, with amplitude $\delta\rho/\rho \approx 0.35$. Note that in Run A0 we also observe that the density fluctuation is largest near the boundary between the shear region and the slow stream.

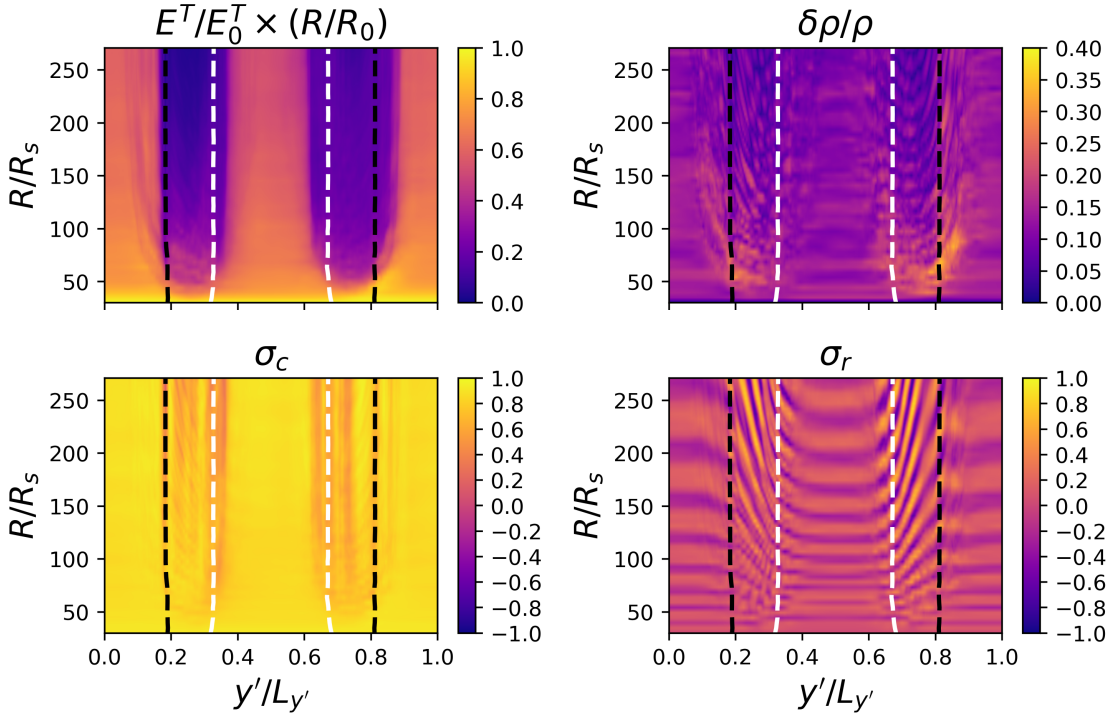

Figure 3.5: $y' - R$ contours of the total Elsässer energy E^T/E_0^T compensated by R/R_0 where E_0^T is $E^T(t=0)$ (top-left), the normalized density perturbation $\delta\rho/\rho$ (top-right), the normalized cross-helicity σ_c (bottom left) and the normalized residual energy σ_r (bottom right) for Run A. White dashed lines mark the longitudes where the x'-averaged radial speed u_{0x} equals 650 km/s and black dashed lines mark the longitudes where the x'-averaged radial speed u_{0x} equals 400 km/s.

It is known from the observations that the normalized cross-helicity decreases with radial distance (e.g. Roberts et al., 1987a,b). The possible mechanisms for the decrease include the generation of inward Alfvén waves due to the velocity shears and the faster decay of outward Alfvén waves with distance compared with the inward waves (Bruno & Bavassano, 1991). In Run A0 we already see that the velocity shear leads to the drop of σ_c. From Figure 3.5, we confirm that σ_c drops with radial distance inside the shear regions, especially near the boundaries of the fast stream. It decreases to values around $0.7 - 0.8$ within $100R_s$ and then decreases slowly to around $0.5 - 0.6$ until the end of the simulation $R = 270.9R_s$. In the fast

and slow streams, σ_c remains almost constant around the initial value 0.92. Compared with Run A0, the contour of σ_c is quite smooth and no stripe-like structures are formed, indicating that the expansion effect slows down the evolution of the wave energies. Last, we look at the residual energy shown in the bottom-right panel. Similar to Run A0, the normalized residual energy fluctuates around 0 and no systematic growth of σ_r is observed. However, the oscillation of σ_r is much weaker in Run A than in Run A0 because the expansion reduces the Alfvén speed so that the relative speed between the outward and inward waves goes down with radial distance.

Figure 3.6 shows the power spectra of the Elsässer variables along the parallel direction $\hat{e}_{x'}$ (in this run it is aligned with the radial direction) at (a) $R = 107.1R_s \approx 0.5\,\mathrm{AU}$ and (b) $R = 217.9R_s \approx 1\,\mathrm{AU}$. Again we divide the domain into four regions: the fast stream, the slow stream and the two shear regions (in Run B-D they are the compression/rarefaction regions). The spectra in different regions are displayed in four subplots at each time. The shear region plotted on the top row is the one at $y' \approx 0.75L_{y'}$. The spectra are averaged in y' inside each region and are multiplied by $k_{x'}^{5/3}$. The blue and orange solid curves are the z and $\perp$ components of the outward Alfvén waves and the dashed curves are of the inward waves. Inside the shear regions, the wave energies are strongly damped and inertial ranges are not observed in the spectra and as the radial distance increases, the spectra are eroded rapidly. In the fast and slow streams, the spectra behave similarly and are more stable compared with the shear regions. Especially, $\mathbf{z_{out}}$ shows clear 3-segment spectra: the large scales with $k_{x'}R_s \lesssim 1$, the intermediate scales with $1 \lesssim k_{x'}R_s \lesssim 20 - 30$ and the small scales which are dominated by the numerical dissipation. At 0.5 AU, the large scales show slopes close to $-5/3$ in both the fast and slow streams while at 1 AU the large-scale part of the $\mathbf{z_{out}}$ spectrum in the fast stream is eroded by the intermediate-scale part and steepening of the spectrum is observed.

Figure 3.7 shows the power spectra of the Elsässer variables along $\hat{e}_{y'}$ direction at four radial distances: $R = 30.0R_s$, $107.1R_s$, $217.9R_s$, $270.9R_s$. The wavenumber $k_{y'}$ is defined by the normalized y', i.e. $y'/L_{y'}$, so that $k_{y'} \in [0, n_{y'}/2]$. The blue and orange lines are the z and

$\perp$ components of the outward Alfvén wave and the dashed lines are those of the inward Alfvén wave. The spectra are averaged in x' and multiplied by $k_{y'}^{5/3}$. At $R = 30.0R_s$, i.e. the initial state, the curves for z-components are covered by those of $\perp$-components as the initial wave band is circularly-polarized. Kolmogorov-like inertial range which spans about one decade forms at 0.5 AU for all the wave components. It maintains throughout the simulation for $E_{out,\perp}$ and $E_{in,\perp}$. But for $E_{in,z}$ the inertial range shortens with radial distance and for $E_{out,z}$ the inertial range becomes shallower than $k_{y'}^{-5/3}$ at 1 AU. This asymmetry between the $\perp$-component and the z-component is due to the uniformity in z-direction which rules out the nonlinear interaction between the waves along $\hat{e}_z$.

3.1.3.5 Run B: corotation, expansion, outward-dominant waves

In this section we present the results of Run B ($\alpha = 0.142$, $r_{io} = 0.2$ and $\delta b = 0.2$). This run has the most realistic setup: expansion, velocity shear and compression/rarefaction are all present and the initial perturbations are outward-dominant Alfvén waves.

Figure 3.8 is a similar plot with Figure 3.5 for Run B. From top-left to bottom right are the corrected total Elsässer energy $E^T/E_0^T \times (R/R_0)$, the normalized density fluctuation, the normalized cross-helicity and the normalized residual energy. The white and black dashed lines mark $u_{0x} = 650\,\mathrm{km/s}$ and $u_{0x} = 400\,\mathrm{km/s}$ respectively. Similar to Run A, The total energy decays faster than the WKB prediction R^{-1}. However, in the fast and slow streams, the radial decay of E^T is significantly faster in Run B than in Run A. Besides, in Run B, beyond $R \approx 200R_s$, a narrow band inside the compression region forms at $y' \approx 0.75L_{y'}$, where the wave energy is much more damped compared with the shear regions in Run A. This might be due to the fact that the compression between the fast and slow streams steepens the velocity profile, enlarging the velocity shear. $\delta\rho/\rho$ and σ_r do not show significant differences between Run A and Run B. Similar to Run A, the decrease of σ_c is more significant in the compression and rarefaction regions than inside the fast and slow streams. In the rarefaction region, mainly in the trailing edge of the fast stream, σ_c drops to around 0.6 very soon at $R \approx 80R_s$ and remains around this value until the end of the simulation. In the compression

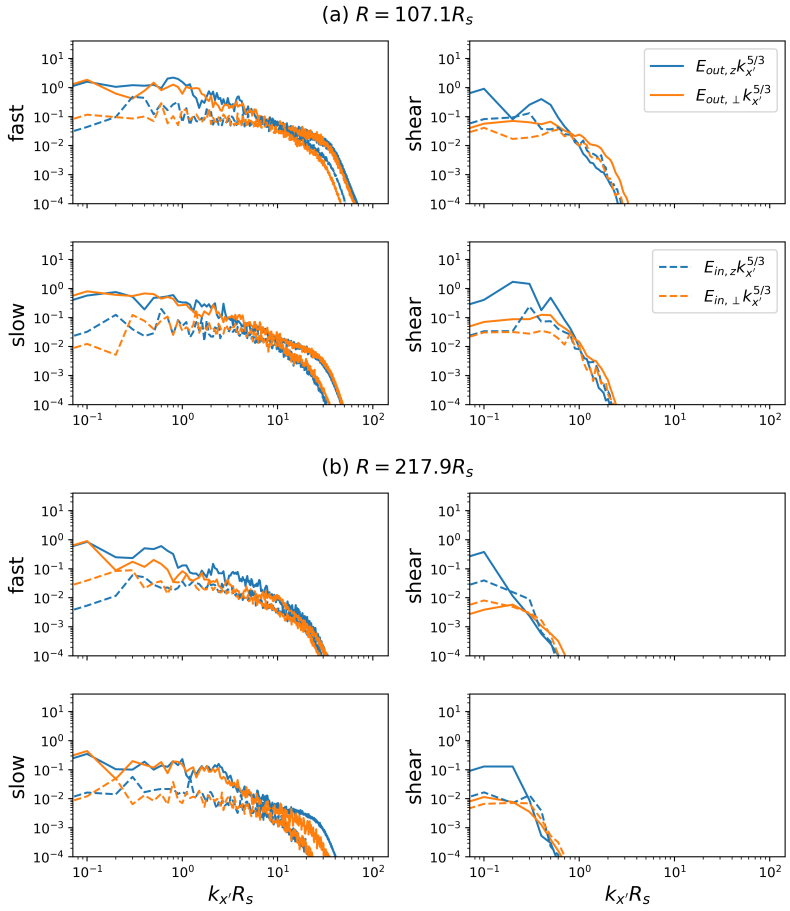

Figure 3.6: Power spectra of the Elsässer variables in Run A at (a) $R = 107.1R_s$ and (b) $R = 217.9R_s$ averaged in different regions: fast stream (top left), slow stream (bottom left), shear region at $y' = 0.75L_{y'}$ (top right) and shear region at $y' = 0.25L_{y'}$ (bottom right). The spectra are calculated along parallel direction $\hat{e}_{x'}$. Blue and orange solid lines are the z-component and in-plane perpendicular-to-$\mathbf{B_0}$-component of the outward Alfvén wave. Blue and orange dashed lines are the two components of the inward Alfvén wave. The spectra are multiplied by $k_{x'}^{5/3}$.

region, however, σ_c remains relatively large (> 0.5) for a long time followed by a fast drop beyond $R \approx 1\,\mathrm{AU}$ and reaches around -0.7 at the end of the simulation $R = 270.9R_s$. The drop of σ_c coincides with the drop of E^T in the compression region (see the top-left panel). In the fast and slow streams, σ_c decreases with distance more slowly, from the initial value

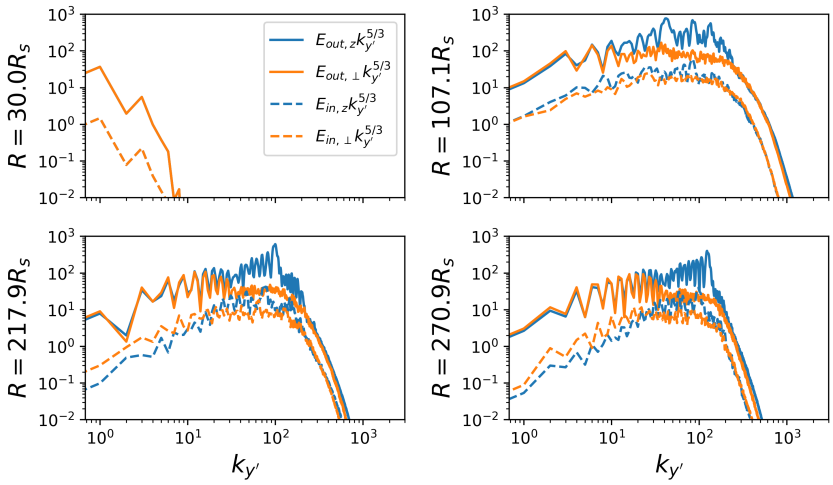

Figure 3.7: Power spectra of the Elsässer variables calculated along $\hat{e}_{y'}$ and averaged in x' in Run A. From top-left to bottom-right are at $R = 30.0R_s$, $107.1R_s$, $217.9R_s$ & $270.9R_s$ respectively. Blue and orange solid lines are the z-component and in-plane perpendicular-to-$\mathbf{B_0}$-component of the outward Alfvén wave. Blue and orange dashed lines are the two components of the inward Alfvén wave. The spectra are multiplied by $k_{y'}^{5/3}$.

0.92 to $\sim 0.7 - 0.8$ at 1 AU. Note that in Run A, σ_c remains almost constant around the initial value 0.92 inside the fast and slow streams, i.e. the velocity shear only reduces the normalized cross-helicity locally in the shear regions. Thus, the compression between the fast and slow streams might play an important role in the radial evolution of σ_c. It not only speeds up the drop of σ_c in the compression region but also speeds up the decrease of σ_c inside the fast and slow streams by steepening the velocity profile at all longitudes.

Figure 3.9 shows the $k_{x'}^{5/3}$-corrected power spectra of $\mathbf{z_{out}}$ and $\mathbf{z_{in}}$ in fast stream, slow stream, the compression region and the rarefaction region at $R = 107.1R_s$ and $R = 217.9R_s$. By comparing Figure 3.9 and 3.6, several differences are observed. First, inside the compression and rarefaction regions (shear regions in Run A), the Elsässer energies are damped in both runs but in Run B the damping is weaker than Run A. Especially, in Run B the wave energy decays with $k_{x'}$ much slower, indicating that the compression and rarefaction transfer energy from large scales to small scales effectively. Second, in Run B, we also observe an

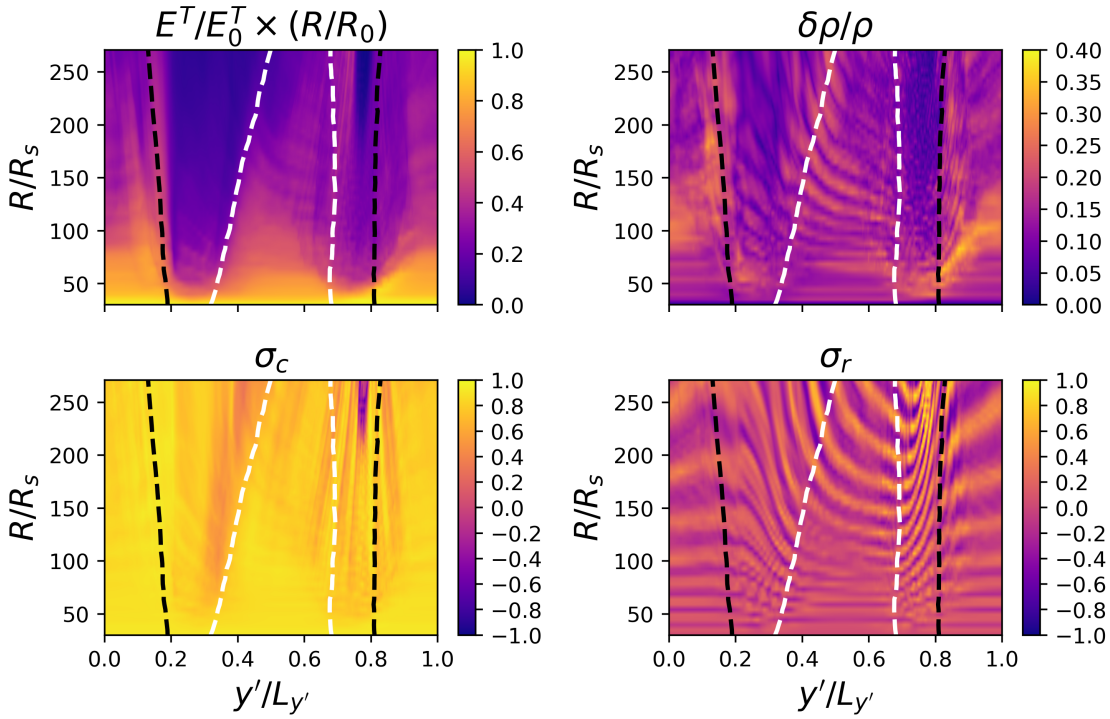

Figure 3.8: $y' - R$ contours of the total Elsässer energy E^T/E_0^T compensated by R/R_0 where E_0^T is $E^T(t=0)$ (top-left), the normalized density perturbation $\delta\rho/\rho$ (top-right), the normalized cross-helicity σ_c (bottom left) and the normalized residual energy σ_r (bottom right) for Run B. White dashed lines mark the longitudes where the x'-averaged radial speed u_{0x} equals 650 km/s and black dashed lines mark the longitudes where the x'-averaged radial speed u_{0x} equals 400 km/s.

asymmetry between the compression and rarefaction regions: at high-$k_{x'}$ ranges ($k_{x'}R_s \gtrsim 1$), the inward wave energy dominates in the rarefaction region while in the compression region the outward wave energy dominates. Third, inside the fast and slow streams, the evolution of the spectra is different in Run B compared with Run A. At $R = 107.1R_s$, the inward waves show $-5/3$ spectra over a substantial range of $k_{x'}$ but the outward waves show spectra steeper than $k_{x'}^{-5/3}$. During the evolution toward 1 AU, the spectra of $\mathbf{z_{in}}$ steepen while the spectra of $\mathbf{z_{out}}$ develop a Kolmogorov-like inertial range as seen in plot (b) of Figure 3.9. The span of the inertial range in the fast stream is larger than that in the slow stream.

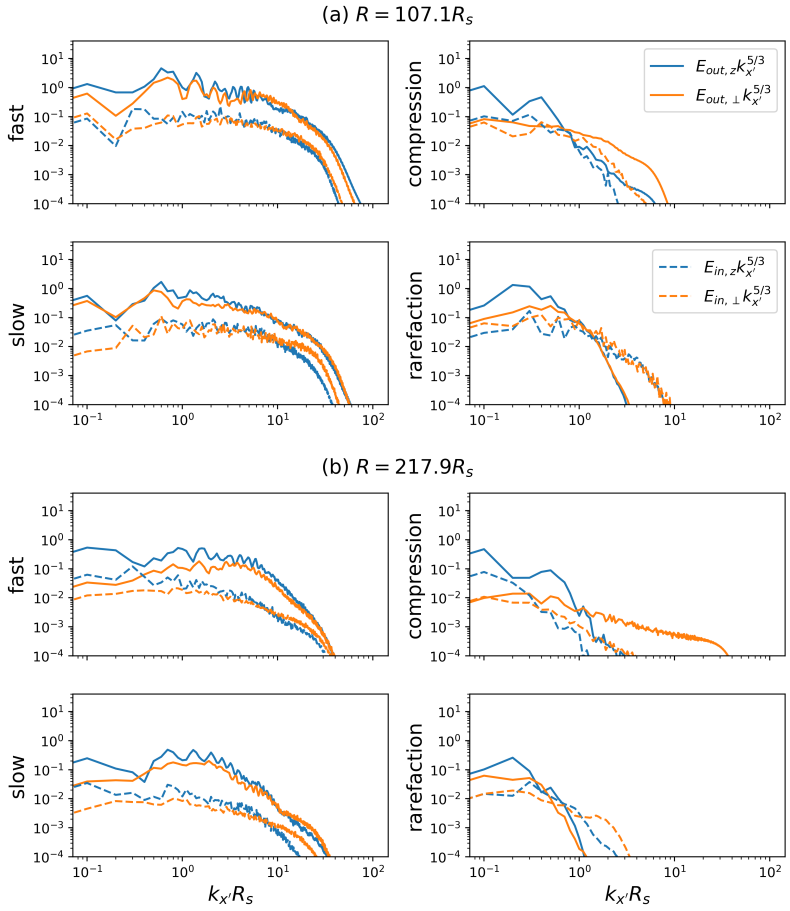

Figure 3.9: Power spectra of the Elsässer variables in Run B at (a) $R = 107.1R_s$ and (b) $R = 217.9R_s$ averaged in different regions: fast stream (top left), slow stream (bottom left), compression region (top right) and rarefaction region (bottom right). The spectra are calculated along parallel direction $\hat{e}_{x'}$. Blue and orange solid lines are the z-component and in-plane perpendicular-to-$\mathbf{B_0}$-component of the outward Alfvén wave. Blue and orange dashed lines are the two components of the inward Alfvén wave. The spectra are multiplied by $k_{x'}^{5/3}$.

Figure 3.10 is the x'-averaged y'-spectra of $\mathbf{z_{out}}$ and $\mathbf{z_{in}}$ corrected by $k_{y'}^{5/3}$ in Run B. At $R = 107.1R_s$ the Kolmogorov-type inertial range is well established for both outward and inward waves. Different from Run A, the shape of the spectra is only slightly changed throughout the simulation in this run.

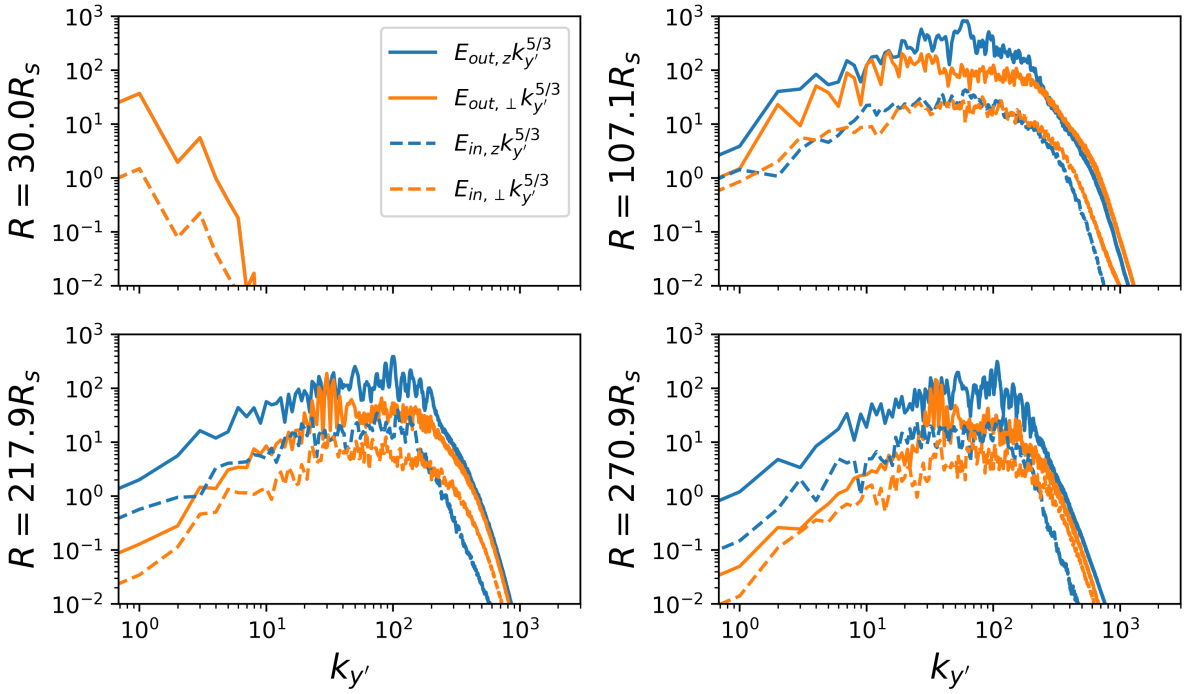

Figure 3.10: Power spectra of the Elsässer variables calculated along $\hat{e}_{y'}$ and averaged in x' in Run B. From top-left to bottom-right are at $R = 30.0R_s$, $107.1R_s$, $217.9R_s$ & $270.9R_s$ respectively. Blue and orange solid lines are the z-component and in-plane perpendicular-to-$\mathbf{B_0}$-component of the outward Alfvén wave. Blue and orange dashed lines are the two components of the inward Alfvén wave. The spectra are multiplied by $k_{y'}^{5/3}$.

3.1.3.6 Run C and Run D

Run C and Run D have both corotation and expansion turned on, similar to Run B, but have $r_{io} = 1$ and $r_{io} = 5$ respectively. They are carried out to show how the inward and outward waves evolve differently when their amplitudes change.

Figure 3.11 compares the $k_{x'}^{5/3}$-corrected parallel power spectra of the Elsässer variables inside the fast and slow streams at $217.9R_s$ for Run B-D. For Run C and Run D, the spectra inside the slow stream show inertial ranges steeper than $k_{x'}^{-5/3}$. Inside the fast stream, Run D shows a short Kolmogorov-like range at $k_{x'}R_s \sim 1 - 4$ for E_{in} while Run C shows a shorter one in $E_{out,z}$ and $E_{in,z}$. Note that in Run B, clear Kolmogorov-like inertial ranges are

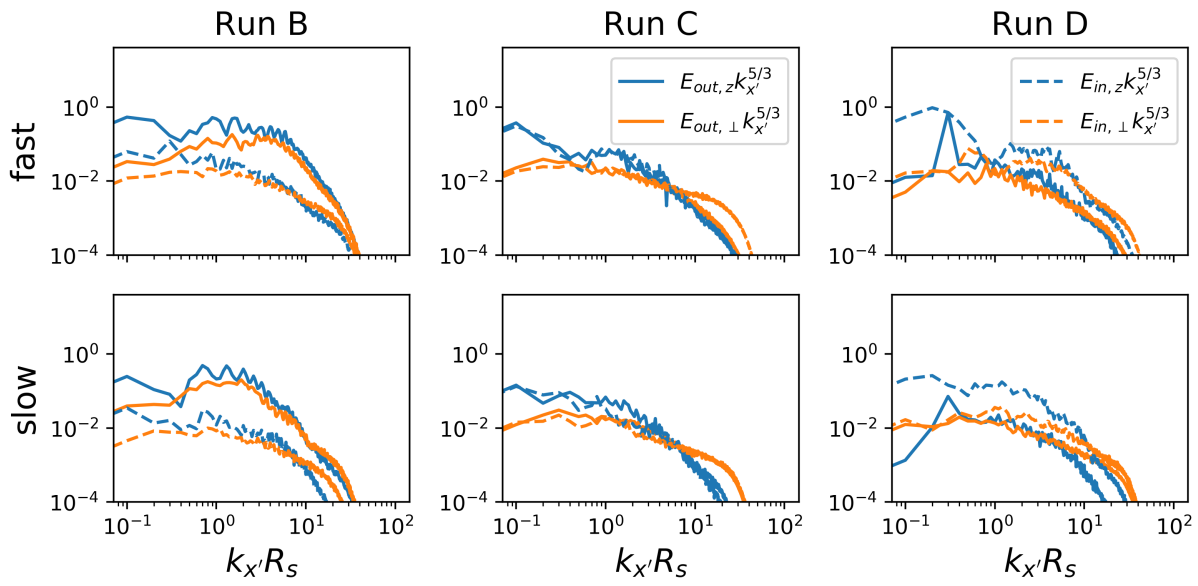

Figure 3.11: Parallel power spectra multiplied by $k_{x'}^{5/3}$ of Elsässer variables inside the fast (top row) and slow streams (bottom row) at $217.9R_s$ for Run B (left column), C (middle column), and D(right column). Blue and orange solid lines are the z-component and in-plane perpendicular-component of the outward Alfvén wave. Blue and orange dashed lines are the two components of the inward Alfvén wave.

observed in E_{out} spectra inside both fast and slow streams. In other words, in order to get Kolmogorov-like parallel spectra, the outward-dominant initial condition is preferred to the balanced and the inward-dominant ones. However, as shown in Figure 3.12, the $k_{y'}$ spectra at $217.9R_s$ are similar for Run B, C and D as clear $k_{y'}^{-5/3}$ inertial ranges are observed in all of the 3 runs.

We then inspect the radial evolution of E_{out} and E_{in} inside different regions for Run A-D and the results are shown in Figure 3.13. The energies are corrected by R/R_0 and the plot is log-log scale. Solid and dashed curves are E_{out} and E_{in} respectively. Colors represent different regions as shown in the legend and described in the caption where the subscripts "f", "s", "c", and "r" represent fast stream, slow stream, compression region, and rarefaction region respectively. For Run C, we multiply the energies in the four regions by different factors, as shown in the plot, in order to separate the overlapped curves and

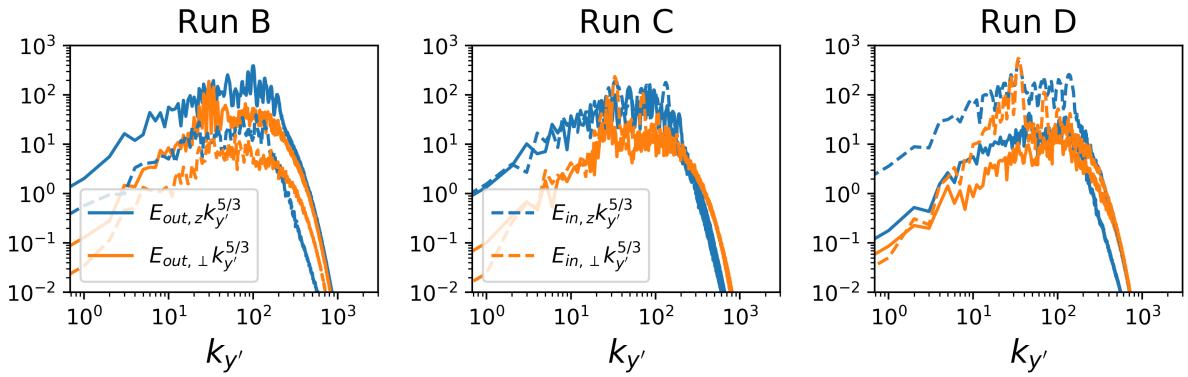

Figure 3.12: Power spectra of Elsässer variables calculated along $\hat{e}_{y'}$ averaged in x' at $217.9R_s$ for Run B (left), C (middle) and D (right). Blue and orange solid lines are the z-component and in-plane perpendicular-component of the outward Alfvén wave. Blue and orange dashed lines are the two components of the inward Alfvén wave. The spectra are multiplied by $k_{y'}^{5/3}$.

make the plot more readable. The energies are calculated by averaging $\frac{1}{2}|z^{\pm}|^2$ over different regions at each time. We first compare Run A and Run B. These two runs are both outward-dominant but Run A lacks the compression and rarefaction between streams. Compared with Run B, in Run A E_{out} decays much slower inside the fast and slow streams but faster inside the shear regions, i.e. the compression effect speeds up the dissipation of the outward waves in the regions without large velocity gradients but it slows down the dissipation inside the regions with large velocity gradients. The evolution of E_{in} inside the fast and slow streams do not show significant differences between Run A and Run B and approximately follow the R^{-1} WKB prediction. But in the shear regions E_{in}, similar to E_{out}, decays faster in Run A than Run B. Then we compare Run C with Run B. In Run C the initial condition consists of balanced outward/inward waves instead of outward-dominant waves. By comparing the blue and orange curves in panel Run C, we see that the evolution of E_{out} and E_{in} is very similar to each other inside the fast and slow streams and the decay rates are similar to those of E_{out} in Run B. Inside the rarefaction region, the inward waves decay much slower than the outward waves. Compared to Run B, E_{in} shows a slower decay rate while E_{out} has

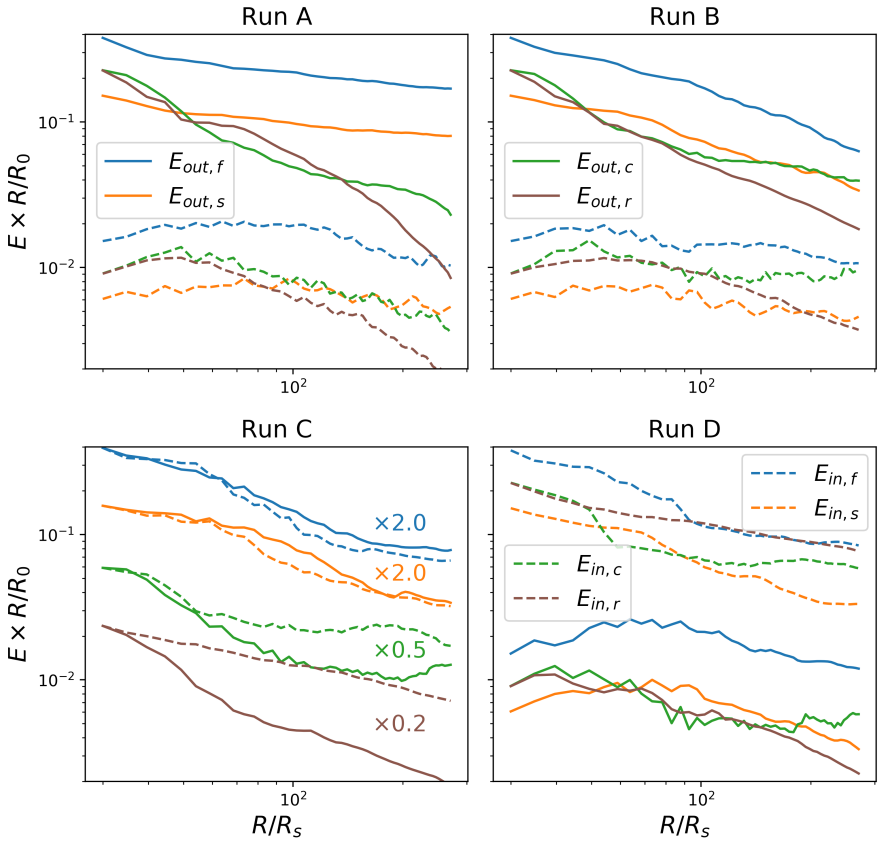

Figure 3.13: Radial evolution of the Elsässer energies E_{out} (solid curves) and E_{in} (dashed curves) in different regions. The energies are corrected by R/R_0. From top-left to bottom-right panels are Run A-D respectively. The plot is in log-log scale. Blue, orange, green and brown represent fast stream ("f"), slow stream ("s"), compression region ("c") and rarefaction region ("r"). For Run A the compression and the rarefaction regions are the two shear regions around $y' = 0.75L_{y'}$ and $y' = 0.25L_{y'}$ respectively. For Run C we multiply the energies in the four regions by different factors as shown in the plot in order to separate the overlapped curves.

similar decay rate. In the compression region, both E_{in} and E_{out} show similar evolution as in Run B: a decay followed by a plateau or even an increase. Last, we inspect Run D where the initial condition is inward-dominant wave band, inverse to Run B. Inside the fast stream and the slow stream, E_{in} in Run D evolves similarly with E_{out} in Run B. E_{out} grows at the

beginning and then decays with R, similar to E_{in} in Run B but its growth and decay are stronger. Consistent with Run C, this result shows that when the wave amplitude is large enough, its radial evolution inside the fast and slow streams is not affected by the direction of the propagation. It is likely that there is some mechanism that generates/depletes small-amplitude waves and it works differently for outward and inward waves. In the compression region, E_{in} in Run D evolves similar with E_{out} in Run B and E_{out} in Run D decreases to a smaller level compared with E_{in} in Run B although both of them reach a plateau beyond $R \approx 10^2 R_s$. In the rarefaction region, E_{in} in Run D has a decay rate similar with that in Run C, i.e. slower than that in Run B. On the other hand, E_{out} in Run B, C and D show very close decay rate beyond $R \approx 10^2 R_s$, indicating that the decay of E_{out} in the rarefaction region is not affected by the wave amplitude significantly.

To summarize the above paragraph, we list the major findings from Figure 3.13 below: (1) The radial decrease of the wave amplitude is faster than the WKB prediction when the amplitude is large but gets closer to the WKB prediction when the amplitude is small, especially inside the fast and slow streams where the velocity shear is small. (2) The compression between fast and slow streams speeds up the dissipation of the waves inside the fast and slow streams but slows down the dissipation inside the compression and rarefaction regions. (3) Inside the fast and slow streams, the outward and inward waves do not show significant differences: the radial evolution of their energies are controlled mainly by their amplitudes instead of the propagation directions. (4) In the compression region, the outward wave decays faster than the inward wave but both of them decay slower as the radial distance increases. (5) Inside the rarefaction region, the outward and inward waves show strong asymmetry. The radial decay of the outward wave is in general faster than the inward wave and is not affected by the wave amplitude significantly. The decay of the inward wave energy, on the contrary, is modulated by the wave amplitude: the larger the wave amplitude is, the slower E_{in} decreases with distance.

3.1.4 Summary

In this part of study, we use the corotating expanding box model (2D version) to simulate the propagation of Alfvén waves and turbulence in the solar wind. The large-scale stream interactions, including shear, compression and rarefaction, are evolved self-consistently. The simulation parameters are chosen to be close to the realistic solar wind. We find that the Elsässer energies are depleted in the strong-shear regions due to phase-mixing, accompanied by a decrease of the normalized cross-helicity. This process is greatly enhanced by the compression between fast and slow streams. The generated density fluctuations are overall small ($\delta\rho/\rho \lesssim 0.2$ on average) and there are high-density structures born near the boundaries between the shear regions and the slow streams. The normalized residual energy fluctuates around zero due to the correlation and de-correlation between the outward and inward waves but no net growth or decrease of it is observed, contrary to the solar wind observations which show prevailing excess of magnetic energy (e.g. Roberts et al., 1987b; Grappin et al., 1990; Chen et al., 2013). The parallel spectra of the Elässer variables show Kolmogorov-like inertial ranges only inside the fast and slow streams and when the shear and compression between streams are present. Besides, the outward-dominant waveband is preferred. Otherwise, the parallel spectra are in general steeper than $k^{-5/3}$. On the other hand, the perpendicular, or more precisely the quasi-longitudinal, spectra show Kolmogorov-like inertial ranges in all the runs carried out, no matter whether the compression between streams is present and how the initial waveband is configured. Since the Alfvénic fluctuations are in the perpendicular-to-$\mathbf{B_0}$ direction, it is reasonable to expect that the spectra are more developed in this direction (plane). The radial evolution of the Elässer energies shows significant longitudinal-dependence, symmetry/asymmetry between the outward and inward waves and the wave-amplitude dependence.

In this study we have allowed for the large scale stream structure, but we have not included the corresponding sector structure with heliospheric current sheet. The heliospheric current sheet is known to be embedded inside the slow wind, at least at solar minimum (Smith, 2001), and the corresponding magnetic shears might modify the conclusions reached

above. Current sheets themselves might evolve dynamically and interact with a turbulence in a non trivial way, as in the region where the magnetic field changes sign, the magnetic field velocity field correlation for outwardly propagating Alfvénic fluctuations must also change sign, leaving a region with little correlation and probably a strong magnetic excess in between. The influence of heliospheric current sheets on the solar wind turbulence is present in Section 3.2.

3.2 Influence of heliospheric current sheets on Alfvénic turbulence in the solar wind

3.2.1 Introduction

In Section 3.1, we show that the large-scale velocity shear leads to a decrease of normalized cross helicity (σ_c) with radial distance. Our results confirm the hypothesis proposed by Coleman (1968) that the differential streaming generates Alfvén waves at long wavelengths which do not have a preferential propagating direction and thus the initial dominance of the outward wave gradually declines. Velocity shear is widely adopted in turbulence models as a source for the wave energies and is able to reproduce the observed decrease of σ_c in the models. On the contrary, there has been no satisfactory solar wind turbulence model that leads to negative normalized residual energy (σ_r) so far. For example, in the model by (Zank et al., 2017), the source term for the residual energy is attributed to the stream shear but whether this term causes growth or decay of the residual energy is arbitrary.

Heliospheric current sheet (HCS) is a good candidacy that may influence the evolution of Alfvénic turbulence. In this study, we extend the simulations in Section 3.1. Both large-scale stream interaction regions (SIRs) and HCSs are constructed and evolve self-consistently in the simulations. We investigate how properties of the Alfvénic turbulence evolve radially and how HCSs modify its evolution. A superposed-epoch analysis of HCS crossings at 1 AU is carried out using the OMNI dataset and Alfvénic turbulence properties near HCSs are examined. This section is organized as follows. In Section 3.2.2 we present the results of the

MHD simulations. In Section 3.2.3 we present the superposed-epoch analysis of HCSs. We then discuss our results in Section 3.2.4 and summarize this part in Section 3.2.5.

3.2.2 Expanding-Box-Model simulation

3.2.2.1 Numerical method

The simulation code used in this study is exactly the same as that used in Section 3.1. We carried out four simulations with two free parameters, namely whether a non-zero spiral angle is set and whether the expansion effect is included. Here we mainly present results from the run with both a non-zero spiral angle and the expansion effect, i.e. the most realistic run. The parameters for initial setup is chosen according to solar wind observations. The simulation starts from $R_0 = 30R_s$ and ends at $R = 270.9R_s$ where R_s is solar radius. The initial spiral angle is $\alpha = 0.142$ so that the angle becomes $\pi/4$ at 1 AU. The size of the simulation domain is $L_{x'} \times L_{y'} = 10R_s \times 2\pi R_0$ where $x' - y'$ is corotating coordinates, i.e. x' is parallel to the spiral direction of magnetic field (see Section 3.1). $L_{y'} = 2\pi R_0$ means that the domain is a full circle in the ecliptic plane. The background fields as functions of the quasi-longitudinal direction y' are plotted in Figure 3.14. The wind consists of two fast streams and two slow streams. The transition between fast and slow streams is of the form $\tanh(y'/a_{sh})$ where $a_{sh} = 0.075\pi R_0$. The velocity of the streams is purely radial with the speed ranges from 340 km/s to 700 km/s. The density is 360 cm^{-3} for the slow streams and 140 cm^{-3} for the fast streams. The radial speed of the expanding box, which is defined as the average speed of the plasma inside the simulation domain, is $U_0 = 464$ km/s. Two Harris current sheets with thickness $a_{cs} = 0.025\pi R_0$ are embedded in the center of the slow streams. The current sheets are force-free and a finite z-component is used to make sure that $|\mathbf{B}|$ is constant and the magnetic field strength is uniformly 250 nT. The pressure is uniform and equals 5 nPa so that the temperatures of the fast and slow streams are 2.6×10^6K and 1.0×10^6K respectively. The adiabatic index is set to be $-3/2$ instead of $-5/3$ because the solar wind observations show that the cooling rate of solar wind plasma is slower than a $-5/3$ adiabatic cooling (e.g. Hellinger et al., 2011).

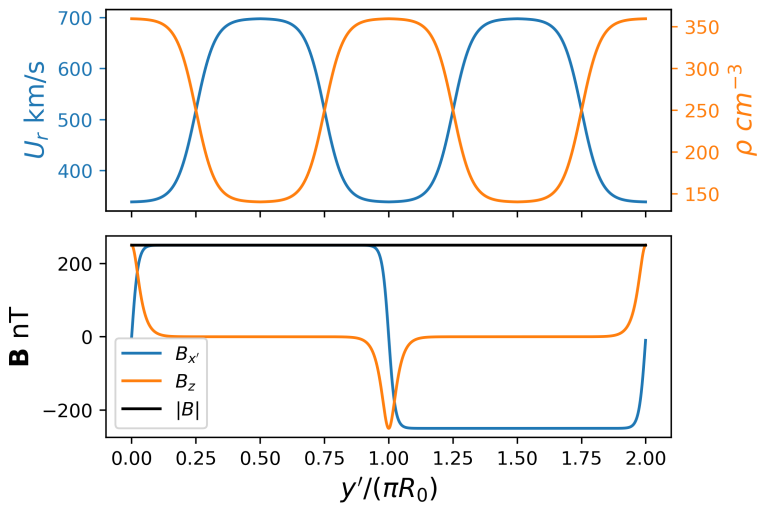

Figure 3.14: Profiles of the background fields along the quasi-longitudinal direction y'.

Circularly-polarized Alfvénic wave bands comprising 16 modes are added on top of the background streams with wave vectors parallel to $\hat{e}_{x'}$. The energy spectrum of the initial waves obeys $E(k_{x'}) \propto k_{x'}^{-1}$. Both outward and inward waves are added with the amplitude of inward waves being 1/5 of the amplitude of outward waves. The amplitude of the first mode of outward waves is $0.2B_0$. To avoid sharp jumps in perturbation fields across the current sheets, we modulate the wave amplitudes by the x'-component of background magnetic field such that the wave amplitudes are exactly 0 at the center of the current sheets. Note that this requires non-zero wave components along x' inside the current sheets to ensure $\nabla \cdot \mathbf{B} = 0$. The number of grid points is $n_{x'} \times n_{y'} = 2048 \times 8192$ so that the smallest wavelength the simulation resolves is $\lambda = 2\Delta x' \approx 0.01 R_s$, corresponding to a wave period $T \approx \lambda / U_0 \approx 15$s.

3.2.2.2 Simulation results

We process the simulation data using the same method as described in Section 3.1. At each time, or radial distance to the Sun, we first calculate the x'-averaged fields, i.e. the background fields. Then we remove the background fields to get the wave fields. We only analyze wave components that are perpendicular to the background magnetic field $\mathbf{B_0} =$

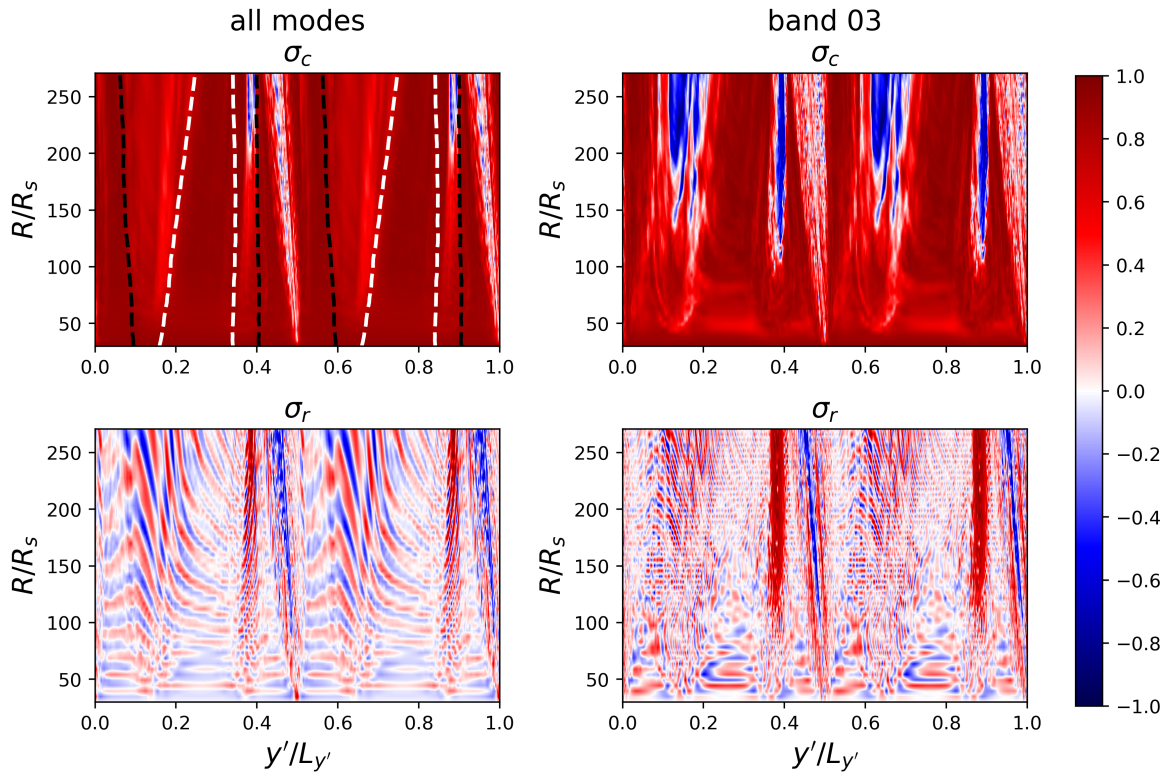

Figure 3.15: $y' - R(t)$ contours of the normalized cross helicity (top row) and the normalized residual energy (bottom row). Left column is the result using wave energies integrated over all modes and right column is the result for wave modes $[4, 8)$, or wave length $\lambda \in [2.5R_s, 1.25R_s)$.

$B_0\,(y')\,\hat{e}_{x'}$. The perturbed Elsässer variables are defined by

$$\mathbf{z_{out}} = \mathbf{u_1} - \text{sign}(B_0)\frac{\mathbf{b_1}}{\sqrt{\rho}},\ \mathbf{z_{in}} = \mathbf{u_1} + \text{sign}(B_0)\frac{\mathbf{b_1}}{\sqrt{\rho}}. \tag{3.31}$$

We then apply Fourier transform along x' to $\mathbf{u}_1$, $\mathbf{b}_1/\sqrt{\rho}$, $\mathbf{z_{out}}$ and $\mathbf{z_{in}}$. We divide the wave modes into 10 wave-number bands which are logarithmically spaced, i.e. band i contains modes $[2^{i-1}, 2^i)$. We calculate $\sigma_c(y')$ and $\sigma_r(y')$ for each wave-number band and also for integration of all wave modes.

In Figure 3.15 we present the $y' - R(t)$ contours of σ_c (top row) and σ_r (bottom row) for all wave modes (left column) and for band 03 (right column) which corresponds to wave length $\lambda \in [2.5R_s, 1.25R_s)$. In top-left panel, we mark the boundaries of fast streams, defined

by $y'(t)$ at which the background radial speed equals 650 km/s, by dashed white lines and mark the boundaries of slow streams, defined by $y'(t)$ at which the background radial speed equals 400 km/s by dashed black lines. The two current sheets are located in the center of the slow streams, around $y' = 0.5L_{y'}$ and $y' = L_{y'}$. We first inspect left column of Figure 3.15 which shows σ_c and σ_r calculated using wave energies integrated over all wave-numbers. As already discussed in Section 3.1, in regions with nearly uniform background fields, i.e. inside fast streams and inside slow streams far from the current sheets, σ_c remains almost constant throughout the evolution and so for σ_r, indicating that the Alfvénicity remains high in these regions. In the velocity-shear regions (regions between the black and white lines), σ_c declines with radial distance. Especially, in the compression region (around $y' = (0.35 - 0.4)L_{y'}$ and $y' = (0.85 - 0.9)L_{y'}$), σ_c drops below 0 beyond $200R_s$. In Section 3.1, we show that in shear regions, the damping of the outward Alfvén wave is significantly faster than the inward Alfvén wave, leading to the decrease in σ_c. Except for near the current sheets, which will be discussed in detail later, σ_r oscillates around 0 in all regions, indicating that the Alfvénicity of the waves is well conserved. The oscillation in σ_r is caused by correlation and de-correlation between the outward and inward waves. From left column of Figure 3.15, we also see that the evolution of Alfvén waves is significantly modified by the current sheets. In the neighborhood of the current sheets, σ_c decreases quite fast and σ_r evolves toward negative values. In the left panel of Figure 3.16 we plot the radial evolution of σ_c and σ_r in a band of width $2a_{cs}$ around the current sheet initially located at $y' = 0.5L_{y'}$. σ_c starts from a high value, i.e. 0.92 determined by the initial condition, drops to around 0.2 within $100R_s$ and then remains stable. σ_r starts from exactly 0, rises slightly at the beginning and then starts to drop continuously, reaching a value -0.3 at 1 AU. For comparison, we plot the time evolution of σ_c and σ_r in the run without expansion in the right panel of Figure 3.16. Evolution of σ_c does not show much difference between the two runs while σ_r remains around 0 in the run without expansion, indicating that expansion effect is important in reduction of σ_r.

In right column of Figure 3.15, we show the $y' - R(t)$ contours of σ_c and σ_r for wave band 03. Compared with left column, the drop of σ_c in velocity-shear regions is much more

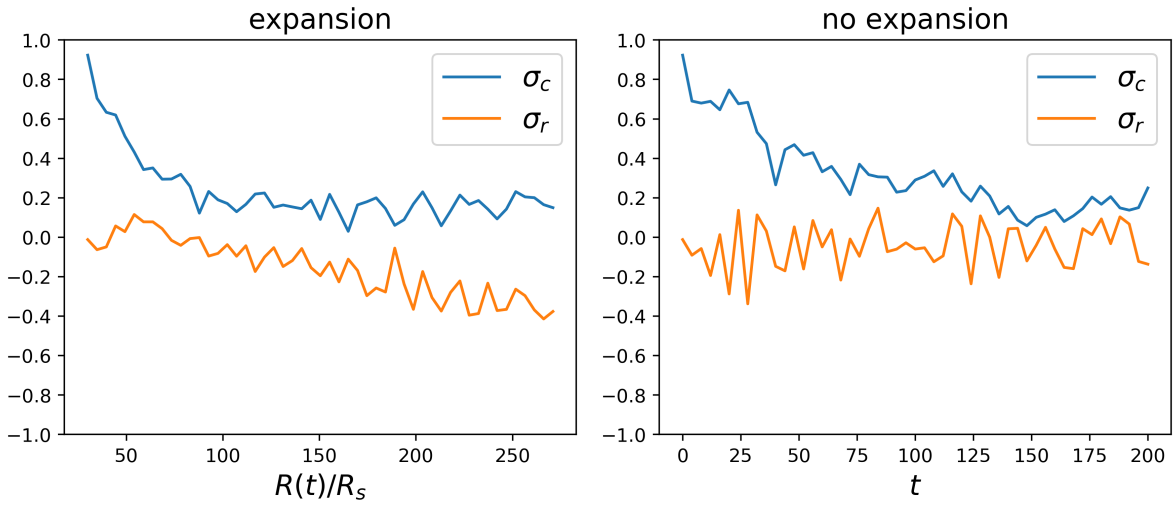

Figure 3.16: Left: radial evolution of σ_c (blue) and σ_r (orange) near the current sheet initially located at $y' = 0.5L_{y'}$ in the run with expansion. Right: time evolution of σ_c (blue) and σ_r (orange) near the current sheet initially located at $y' = 0.5L_{y'}$ in the run without expansion.

significant and the σ_c-drop regions around the current sheets are wider. For σ_r, the most prominent feature is that inside the compression regions, σ_r evolves toward +1, i.e. kinetic energy is dominant in these regions, indicating that the large velocity shear and compression facilitate the transfer of kinetic energy toward small scales. In Figure 3.17 we show the x'-spectra of various fields calculated at the moment $R(t) = 217.9R_s$. From left to right columns are spectra averaged in y'-bands of width $2a_{cs}$ inside fast stream, current sheet and compression region respectively. Top row shows the spectra of outward (blue) and inward (orange) Elsässer variables. Middle row shows the spectra of kinetic (blue) and magnetic (orange) perturbations. We multiply these spectra by $k_{x'}^{5/3}$. In general, these spectra are steeper than Kolmogorov's $-5/3$ prediction except for inside the fast stream. Bottom row shows the spectra of σ_c and σ_r calculated from the spectra shown in top and middle rows. Inside the fast stream, σ_c is close to 1 and σ_r is close to 0 for most modes, except for close to the numerical dissipation range, meaning that the waves maintain a high Alfvénicity over a large span of wave numbers. Around the current sheet, σ_c decreases to nearly 0 for all wave numbers. σ_r is negative for most of the wave numbers, except for an intermediate range

$(1 < k_{x'} < 3)$ where it is around 0. In the compression region, σ_c is overall smaller than the initial condition 0.92 but the curve of σ_c shows a decrease with $k_{x'}$ at small wave numbers and rises again. σ_r is around 0 for small wave numbers and shows a significant increase with $k_{x'}$, reaching its maximum value at the same $k_{x'}$ where σ_c reaches its local minimum. It indicates that in the compression region the large scale stream structure generates fluctuations that are kinetic energy dominated. The newly-generated fluctuations weaken the dominance of the outward Alfvén waves, consistent with the scenario proposed by Coleman (1968).

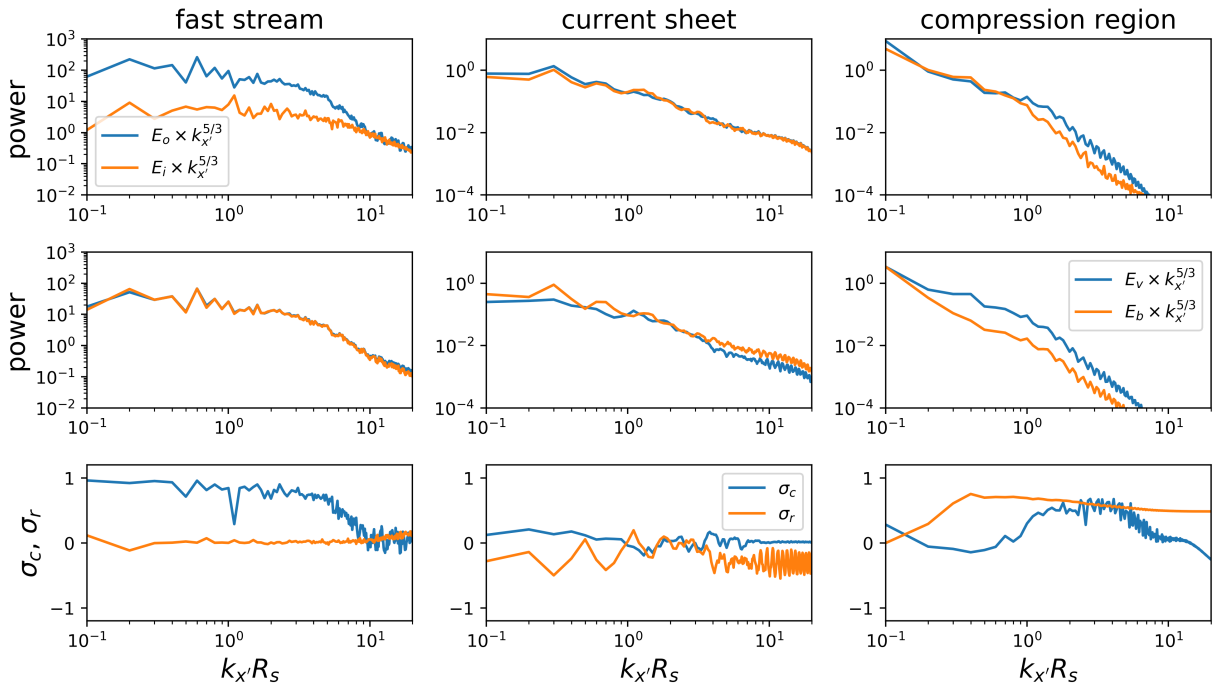

Figure 3.17: x'-spectra of various fields at $R(t) = 217.9R_s$ inside the fast stream (left column), the current sheet (middle column) and the compression region (right column). The spectra are averaged in a y'-band of width $2a_{cs}$ inside each region. Top row: spectra of the outward (blue) and inward (orange) Alfvén waves. Middle row: spectra of the kinetic (blue) and magnetic (orange) perturbations. Bottom row: spectra of σ_c (blue) and σ_r (orange) calculated from the spectra in top and middle rows.

3.2.3 Superposed-epoch analysis of HCSs at 1 AU

Although works have been carried out on turbulence properties around SIRs (e.g. Borovsky & Denton, 2010), literature on how HCSs affect the solar wind turbulence still lacks. Here we carry out a superposed-epoch analysis of HCS crossings at 1 AU and we study how the properties of turbulence change near HCSs.

3.2.3.1 Selection and structure of HCSs

For current study, we use OMNI dataset, which contains magnetic field and plasma data from multiple spacecraft, including ACE and WIND (King & Papitashvili, 2005). Time resolution of the data is 1 minute, enough for study of MHD turbulence. We analyze data during two 4-year periods: 2000-2003 which is around solar maximum and 2007-2010 which is around solar minimum as shown by the shaded regions in Figure 3.18, which plots monthly sunspot number.

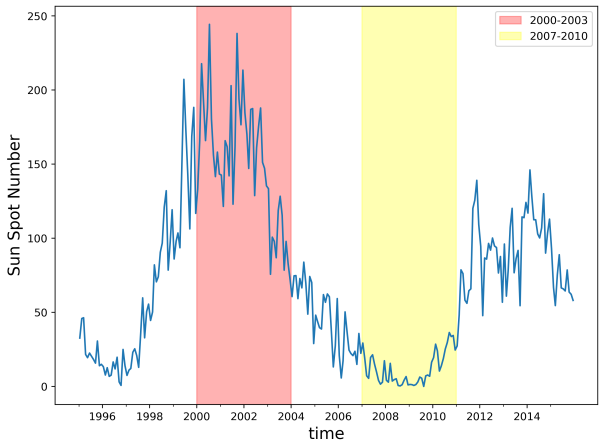

Figure 3.18: Monthly sunspot number from 1995 to 2015. The two shaded regions mark the two time periods used for OMNI data analysis and correspond to solar maximum (2000-2003) and solar minimum (2007-2010) respectively.

The procedure to select HCS crossings is stated as follows. We first calculate one-day average of $B_{x,GSE}$, which is essentially the opposite of radial component of the solar wind

magnetic field. Then we find days when its polarity changes and we require that the polarities before and after each polarity-reversal day maintain at least 4 days. Then we inspect the 1-minute data to determine the exact polarity reversal times. We identify 48 events for solar maximum and 45 events for solar minimum. List of the HCS crossings is shown in Table C.1 in Appendix C.

Superposed-epoch analysis of the HCS structure is shown in Figure 3.19. From top to bottom panels are GSE B_x, B_y, B_z, V_r, GSE V_y, proton density and proton temperature respectively. Left column is solar maximum and right column is solar minimum. In each panel, grey curves are individual events and blue curve is the median value of all events. We have reversed the time series of certain events such that B_x is always turning from negative to positive. Consistent with previous works (e.g. Smith, 2001), HCSs are more likely to be found in slow solar wind. The time scale for HCS crossings is on average 1-2 hours and the HCSs are embedded in much thicker (1-2 days) plasma sheets with enhanced proton density and lower proton temperature. By comparing left and right columns of Figure 3.19, we see that the strength of magnetic field is larger in solar maximum than solar minimum. Another thing to notice is that there is a negative GSE V_y at the HCSs, i.e. the plasma flow is rotating in the same direction with the solar rotation. The reason might be that HCSs are usually embedded in slow solar wind ahead of the compression region and are pushed along longitudinal direction in accordance with solar rotation (Eselevich & Filippov, 1988; Siscoe, 1972).

3.2.3.2 Turbulence properties near HCSs

We then analyze turbulence properties near HCSs. We use a running time window of width 128-min. A time window with data gap ratio larger than 20% is not considered. Inside each time window, we first apply linear interpolation to velocity, magnetic field, and proton density to fill the data gaps. Then we calculate Els asser variables after determining the polarity of radial magnetic field by averaging B_x in the time window. Then we apply Fourier transform to these fields. Similar to the process of simulation data in the prior section,

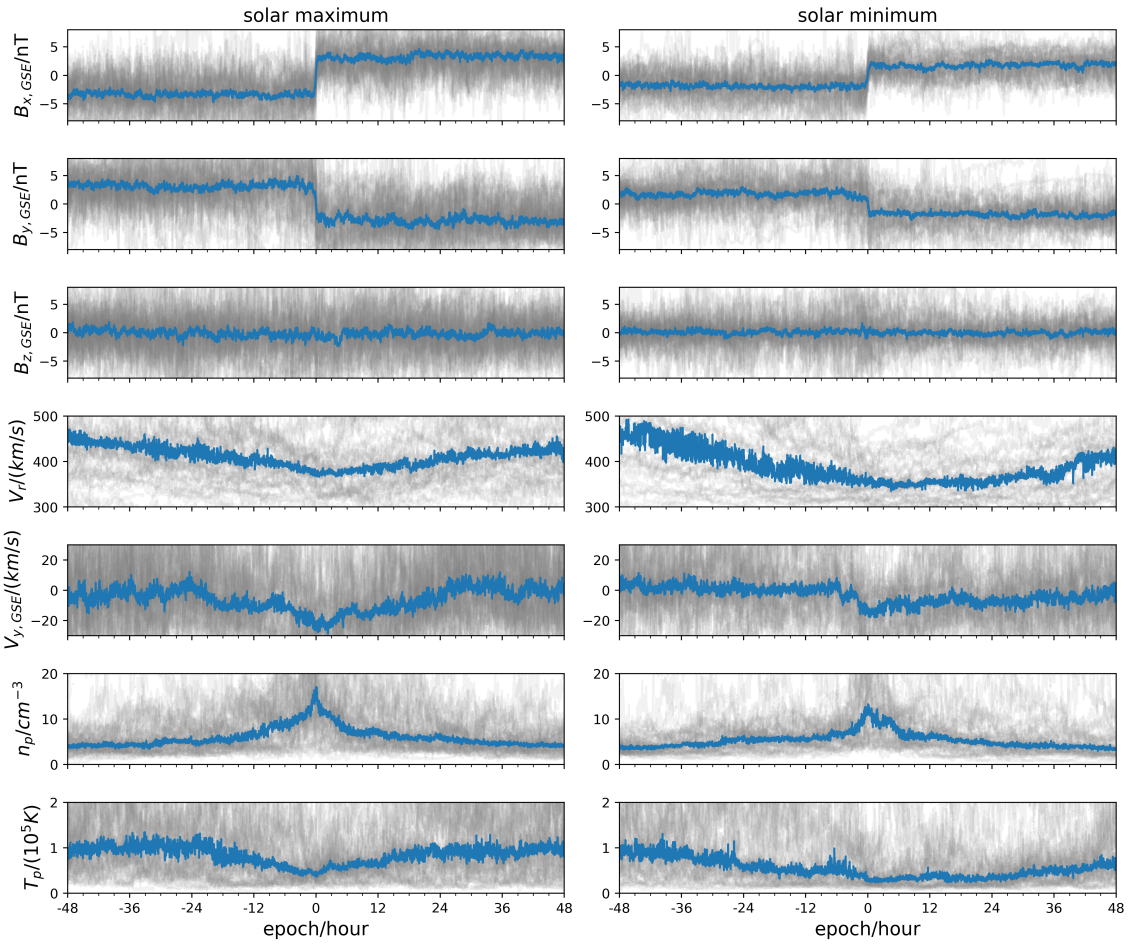

Figure 3.19: Superposed-epoch analysis of the HCS crossings. Epoch 0 is the moment of crossing. From top to bottom rows are B_x, B_y, B_z in GSE coordinates, V_r, GSE V_y, proton density and proton temperature respectively. Left column is solar maximum and right column is solar minimum. In each panel, grey lines are individual events and blue line is the median value.

we divide the frequency into 6 bands such that band i contains wave modes $[2^{i-1}, 2^i)$. We then calculate σ_c and σ_r for each wave band by integrating wave energies in each band. In addition, we fit the spectra and get the spectral slopes for velocity, magnetic field, outward and inward Els asser variables.

In Figure 3.20, we show superposed-epoch analysis of σ_c (top row) and σ_r (bottom row). Left column is solar maximum and right column is solar minimum. Colors represent different

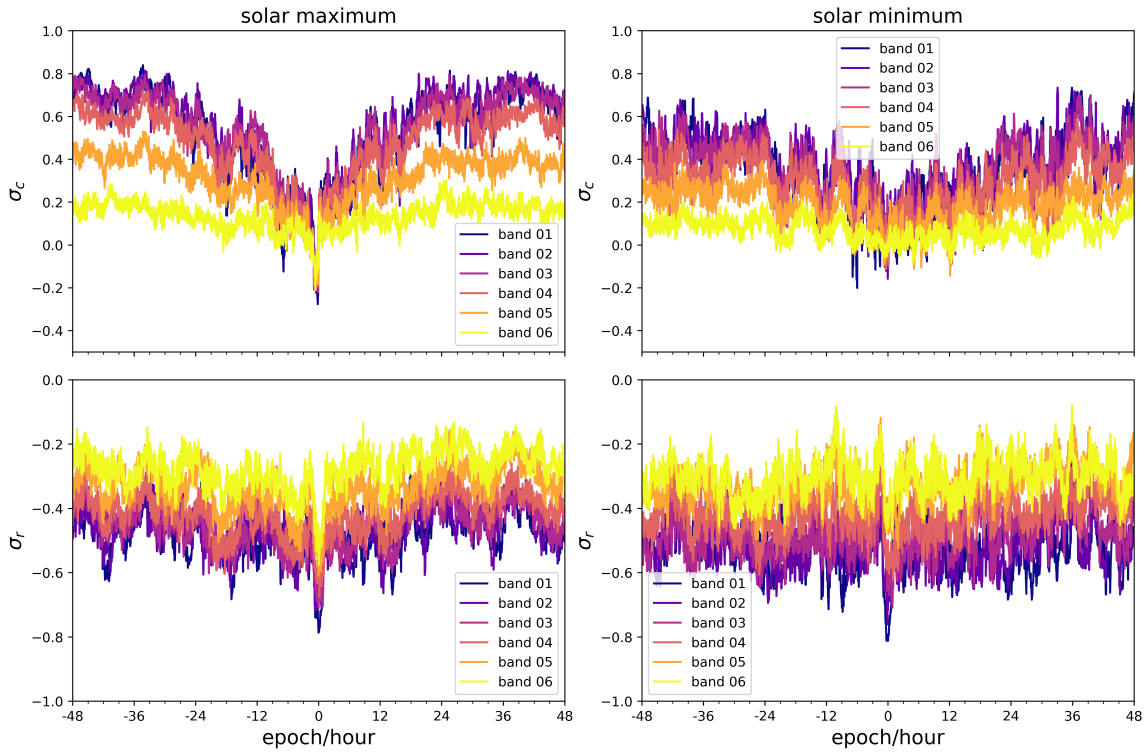

Figure 3.20: Superposed-epoch analysis of σ_c (top row) and σ_r (bottom row) near HCSs. Left column is solar maximum and right column is solar minimum. In each panel, dark to light colors are wave band 01-06 respectively, i.e. from low to high frequency.

wave bands such that dark to light colors are band 01-06. We see that in general σ_c decreases with frequency while σ_r increases with frequency. Top-left panel shows that in a time window $\pm$ 1 day, approximately the width of plasma sheets, σ_c drops as we approach the center of HCSs. In a narrow window of width comparable to the thickness of HCSs, i.e. 1-2 hours, σ_c drops significantly since the outward and inward waves mix with each other. Bottom-left panel of Figure 3.20 shows slightly decrease of σ_r inside plasma sheets while a large drop of σ_r is observed near HCSs. In solar minimum (right column of Figure 3.20), the above results qualitatively hold but both σ_c and σ_r are lower compared with solar maximum.

In Figure 3.21, we show the superposed-epoch analysis of various spectral slopes. Again, left and right columns are solar maximum and solar minimum respectively. In top row, blue and orange curves are spectral slopes of velocity and magnetic field. In bottom row, blue

and orange curves are spectral slopes of outward and inward Elsässer variables. In each panel, the two horizontal dashed lines mark the values 5/3 and 3/2 for reference. Away from HCSs, velocity spectrum has a slope near $-3/2$ and magnetic field spectrum has a slope near $-5/3$. Near HCSs, both of the two spectra steepen and the steepening is more pronounced in solar maximum. The outward Elsässer variable has a spectral slope near $-5/3$ and shows a slight steepening near HCS in solar maximum while no obvious steepening is observed in solar minimum. The variation in spectral slope of inward Elsässer variable is more dramatic compared with the other quantities. $\mathbf{z_{in}}$ spectrum is quite flat far from HCSs, around -1 in solar maximum and -1.2 in solar minimum. Note that in Figure 3.21 we only plot a time window ± 2 days but asymptotic values of the slopes are observed if we extend the range of abscissa. Steepening of the $\mathbf{z_{in}}$ spectrum happens in a large time range, approximately within the plasma sheet. At the center of HCSs, the inward and outward Elsässer variables have the same slope as expected since the two wave populations are not well separated near the polarity-reversal time.

3.2.4 Discussion

We compare the simulation results from Section 3.2.2 and the superposed-epoch analysis from Section 3.2.3. In the simulation, σ_c drops in a wide longitudinal range around the current sheet (Figure 3.15), which is also observed at 1 AU (Figure 3.20), although in the simulation the plasma sheet bounding the current sheet is not present. Similarly, in both simulation and observation, σ_r drops in the neighbourhood of HCSs. Grappin et al. (1991) analyzed four-month of Helios 1 data and found that within the neutral sheet, the turbulence properties are close to the "standard", or fully-developed, MHD turbulence, rather than Alfvénic turbulence. Standard MHD turbulence is characterized by balanced outward/inward Elsässer energies and an excess of magnetic energy, consistent with our results. In this scenario, the background magnetic field dissipates the residual energy (the so-called "Alfvén effect") which is generated by intrinsic nonlinear interaction. Thus, residual energy is large inside current sheets where Alfvén effect is weak. Grappin et al. (1991) explained the balance between

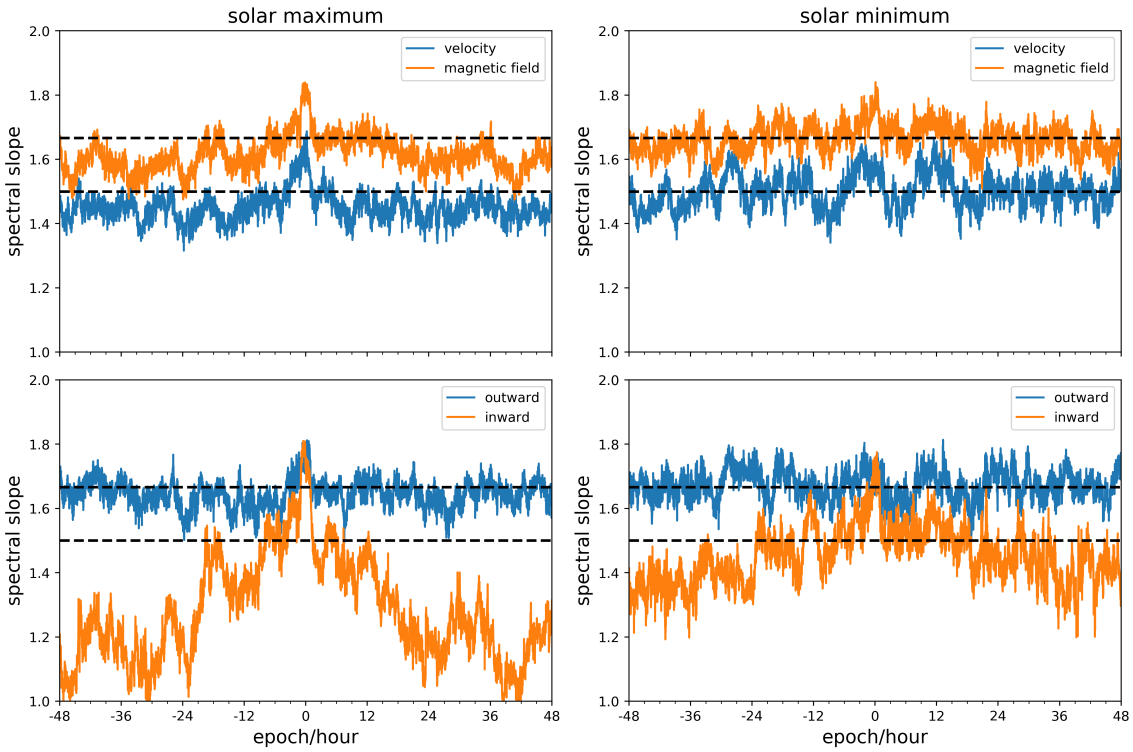

Figure 3.21: Superposed-epoch analysis of various spectral slopes near HCSs. Top panels show slopes of velocity (blue) and magnetic field (orange) and bottom panels show slopes of outward (blue) and inward (orange) Els asser variables. Left column is solar maximum and right column is solar minimum. In each panel, the two horizontal lines mark the values 3/2 and 5/3 for reference.

outward/inward Elsässer energies at small scales by the fact that the injected energy at large scales due to velocity shear is balanced in $\mathbf{z_{in}}$ and $\mathbf{z_{out}}$. This interpretation, however, cannot explain the decrease in σ_c around the current sheet in our simulation because there is no such energy source near the current sheet in the simulation. Here we propose another possible mechanism related to the expansion effect of the solar wind. Near HCSs, the weak background magnetic field allows fluctuations to evolve freely. As a consequence, the radial expansion leads to $\mathbf{u}_\perp \sim 1/R$ and $\mathbf{b}_\perp/\sqrt{\rho} \sim 1$. Hence, as the radial distance increases, the transverse magnetic field fluctuation becomes larger than the transverse velocity fluctuation, leading to a negative σ_r. This mechanism is supported by Figure 3.16 which shows that

without expansion no net residual energy is produced. However, Figure 3.16 also shows that the decrease of σ_c cannot be explained by expansion effect and must be caused by intrinsic nonlinear processes.

However, our simulation cannot explain why σ_r is generally negative even far from HCSs as can be seen from Figure 3.20. Recent studies using Parker Solar Probe data show that σ_r is already negative ($\sigma_r \approx -0.2$) at 35 solar radii while σ_c is increasingly high as the satellite moves closer to the Sun (Chen et al., 2020). Our results show that the presence of a current sheet indeed leads to a dominance of magnetic energy, but it also results in a decrease in σ_c. Thus the observed ($\sigma_c \approx 0, \sigma_r \approx -1$) population of the solar wind fluctuations (e.g. D'Amicis & Bruno, 2015) is possibly Alfvénic turbulence evolved under the influence of current sheets, while the prevailing ($\sigma_c \lesssim 1, \sigma_r \approx -0.2$) population may be generated in very young solar wind with other processes taking effect.

Last, we would like to comment that, the statistical study of Alfvénic turbulence properties near SIRs by Borovsky & Denton (2010) shows results quite different from our simulations. Their Figure 11 and Figure 16 show that, at the fast-slow stream interface, the magnetic energy dominance is enhanced, i.e. σ_r decreases, and the Elsässer ratio $|\mathbf{z_{out}}|/|\mathbf{z_{in}}|$ increases, contradicting our simulation results that σ_c declines and σ_r increases at SIRs (Figure 3.15). The reason for this contradiction is unknown and needs further study.

3.2.5 Summary

In this study, we carry out both two-dimensional MHD simulations, using expanding-box-model, and a superposed-epoch analysis, using OMNI data, to study turbulence properties in the solar wind with a focus on heliospheric current sheets (HCSs). The simulation results show that both the normalized cross helicity σ_c and normalized residual energy σ_r drop in the neighborhood of HCSs. The observation at 1 AU shows that σ_c and σ_r decrease sharply at the center of HCSs, on a time scale of $1-2$ hours which is the scale of the HCS crossings. The observation also shows that σ_c starts to drop gradually in a much wider time range $\Delta t > \pm 1$ day, inside the plasma sheets bounding HCSs. The power spectra, calculated over frequency

range $f \in [128^{-1}, 2^{-1}]min^{-1}$ using OMNI data, of velocity, magnetic field, outward and inward Elsässer variables steepen near HCSs. Especially, spectrum of the inward Elsässer variable starts to steepen far from the center of HCSs ($\Delta t > 1$ day) and is very flat there, with slopes around $-(1 - 1.2)$.

Our results confirm that current sheets significantly influence the evolution of solar wind turbulence. They may explain the low cross helicity and magnetic-energy-dominated population of fluctuations in solar wind. But the origin of the prevailing high cross helicity and slightly magnetic-energy-dominated fluctuations needs other mechanisms that play important roles close to the Sun, or at the source region of the Alfvénic fluctuations. Thus, inspection of the Parker Solar Probe data is necessary to fully understand these mechanisms.

3.3 Parker Solar Probe

3.3.1 Introduction

By April, 2020, PSP has finished four orbits and collected a large volume of data. The perihelion is 35.7 solar radii for the first three orbits and 27.9 solar radii for the fourth orbit. In this section, we conducted a statistical analysis of PSP data on Alfvénic turbulence properties and present the preliminary results.

3.3.2 Instruments & Data

We use plasma data from Solar Probe Cup (SPC) and magnetic field data from FIELDS for this study. SPC is a Faraday Cup that looks directly at the Sun and measures ion and electron fluxes and flow angles as a function of energy. Level-3 SPC data contains moments of proton distribution function, i.e. density, velocity and thermal velocity, which are used for our analysis.

We refer to the four orbits of PSP as "Encounter 1,2,3,4" as the high resolution data is only produced near perihelions of the orbits ($R \lesssim 0.3 - 0.4$ AU). During encounters,

SPC provides measurement of one spectrum every 0.218-0.874 s and the cadence of FIELDS is smaller than 13.7 ms. Thus, we re-sample the measurements of magnetic field, proton density, velocity, and thermal speed to a time resolution 0.874s. Then we bin the data into 2048-point time windows. We discard windows with data gap ratio larger than 10% and fill data gaps by linear interpolation. We determine the polarity of radial magnetic field by averaging B_r inside each time window and define Elsässer varibles

$$\mathbf{z_{o,i}} = \mathbf{U} \mp \text{sign}(B_{r0}) \frac{\mathbf{B}}{\sqrt{\mu_0 \rho}} \tag{3.32}$$

where subscripts "o" and "in" represent "outward" and "inward" respectively. Fourier transform is applied to $\mathbf{U}$, $\mathbf{V_A} = \mathbf{B}/\sqrt{\mu_0 \rho}$, and $\mathbf{z_{o,i}}$. We fit the power spectra over mode 5-60, which correspond to wave period $T \in [30s, 360s]$, within inertial range. As shown by Chen et al. (2020), at 0.17 AU, for frequency $f \lesssim 2 \times 10^{-3}$ Hz the spectra are inside the flat energy-containing range and for frequency $f \gtrsim 0.02$ Hz the spectra are contaminated by velocity noise of SPC measurements. Similar to Section 3.2, we divide the wave modes into 10 logarithmic bands such that band i includes modes $[2^{i-1}, 2^i)$. Inside each band, normalized cross helicity σ_c and normalized residual energy σ_r are calculated after integrating energies of all modes.

3.3.3 Statistics on turbulence properties

In Figure 3.22 we show the normalized density fluctuation, defined as the root-mean-square of ion density normalized by averaged density $\Delta n/n$, and ion temperature, defined as ion thermal speed squared V_{th}^2, as functions of radial speed of the solar wind. Colors of the data points represent radial distance. Blue curves are median (solid) and 25%/75% (dashed) values of V_r-binned data. Figure 3.23 is similar to Figure 3.22 but show $\Delta n/n$ and V_{th}^2 as functions of radial distance to the Sun. We first examine the two plots of $\Delta n/n$. We see that $\Delta n/n$ is in general small ($\lesssim 0.2$) and is anti-correlated with solar wind speed. From left panel of Figure 3.23, it can be seen that $\Delta n/n - R$ is slightly negative correlated. Note that the drop of $\Delta n/n$ around $R = 60 R_s$ is the consequence of the lack of slow wind observation. This is a warning that more data is necessary to solidate the results made here. Then we

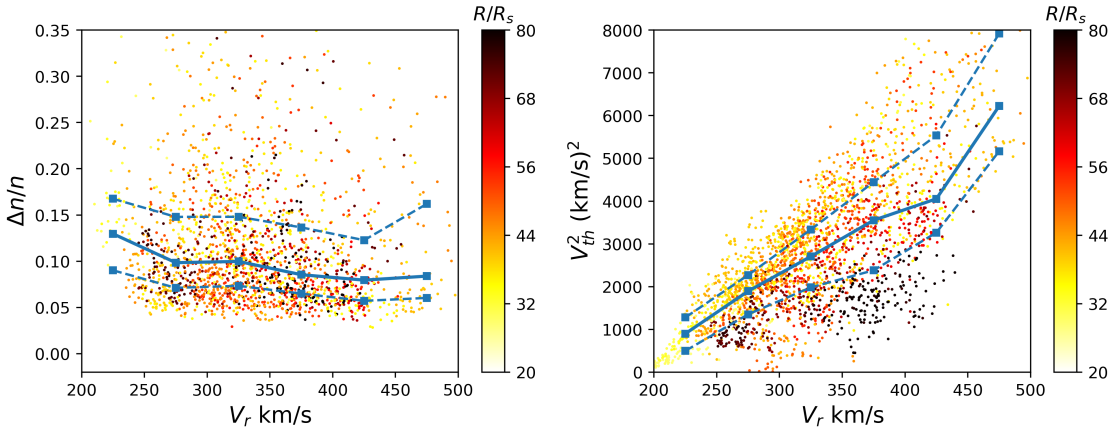

Figure 3.22: Density fluctuations (left panel) and ion temperature ($V^2_{vhermal}$) (right panel) as functions of radial solar wind speed. Colors represent radial distance to the Sun. Blue curves are median (solid) and 25%/75% (dashed) values of V_r-binned data. Encounter 1-4 data of PSP are used.

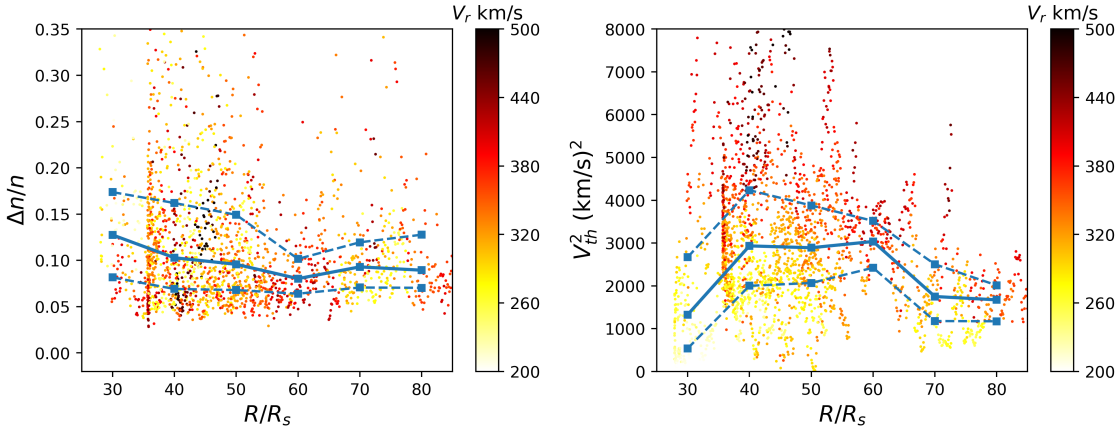

Figure 3.23: Density fluctuations (left panel) and ion temperature ($V^2_{vhermal}$) (right panel) as functions of radial distance to the Sun. Colors represent radial solar wind speed. Blue curves are median (solid) and 25%/75% (dashed) values of R-binned data. Encounter 1-4 data of PSP are used.

check the ion temperature (V^2_{th}) as a function of V_r and R. The right panel of Figure 3.22 shows that V^2_{th} is roughly a linear function of V_r. From the colors of this scatter plot, we observe a drop in the slope of $V^2_{th} - V_r$ relation with increasing radial distance. This indicates

that the radial cooling of solar wind is non-adiabatic, or at least the adiabatic index varies with solar wind speed. Otherwise, since the temperature (which is proportional to V_{th}^2) obeys $T(V_r, R) = T(V_r, R_0) \times (R/R_0)^{-\kappa}$ where R_0 is a reference radius and κ is the adiabatic index, we have $T(V_r, R) \propto T(V_r, R_0)$ when κ is a constant, meaning that the shape of $T - V_r$ is independent of R. The result shown in 3.22 indicates that the fast solar wind cools faster with radial distance than the slow solar wind. The reason is unknown but one possibility is the relatively high density fluctuations in the slow wind which potentially dissipate more energy that heats the wind. The right panel of Figure 3.23 shows a clear radial cooling of the temperature. However, as has been commented for the left panel, effect of the wind speed is non-negligible, which leads to the rise of $V_{th}^2 - R$ curve around $R = 60R_s$. One interesting point here is the extremely low temperature measured during Encounter 4 ($R \lesssim 35R_s$). Even if we only check the light-colored data points that correspond to small wind speed, a clear drop of V_{th}^2 from $R = 40R_s$ to $R = 30R_s$ is observed. Is this a sign of solar wind heating, however, needs further investigation as streams of different solar origins are measured during different encounters.

Figure 3.24 shows the spectral slopes as functions of radial distance to the Sun R and radial solar wind speed V_r. From top-left to bottom right are magnetic field in Alfvén unit S_b, velocity S_v, outward Elsässer variable S_o, and inward Elsässer variable S_i. The data points are binned on $R - V_r$ plane and median value of the data points is calculated inside each block. Colors of the blocks represent these median values which are also written in the blocks. The bracketed numbers show the number of data points inside each block. If there are less than 15 data points inside one block, the value will be set as N/A. We first compare the spectral slopes of magnetic field and velocity, i.e. the top two panels. There is no clear V_r-dependence of S_v while a negative $S_b - V_r$ correlation is observed in the range $R \in [35, 65]R_s$. Close to the Sun ($R < 45R_s$), the difference between S_b and S_v is small. Both of the magnetic field and velocity spectra are flatter than the Kolmogorov's prediction $-5/3$ are around -1.5. As the radial distance increases, steepening of magnetic field spectrum toward $-5/3$ is seen while the velocity spectrum remains almost invariant. It has been

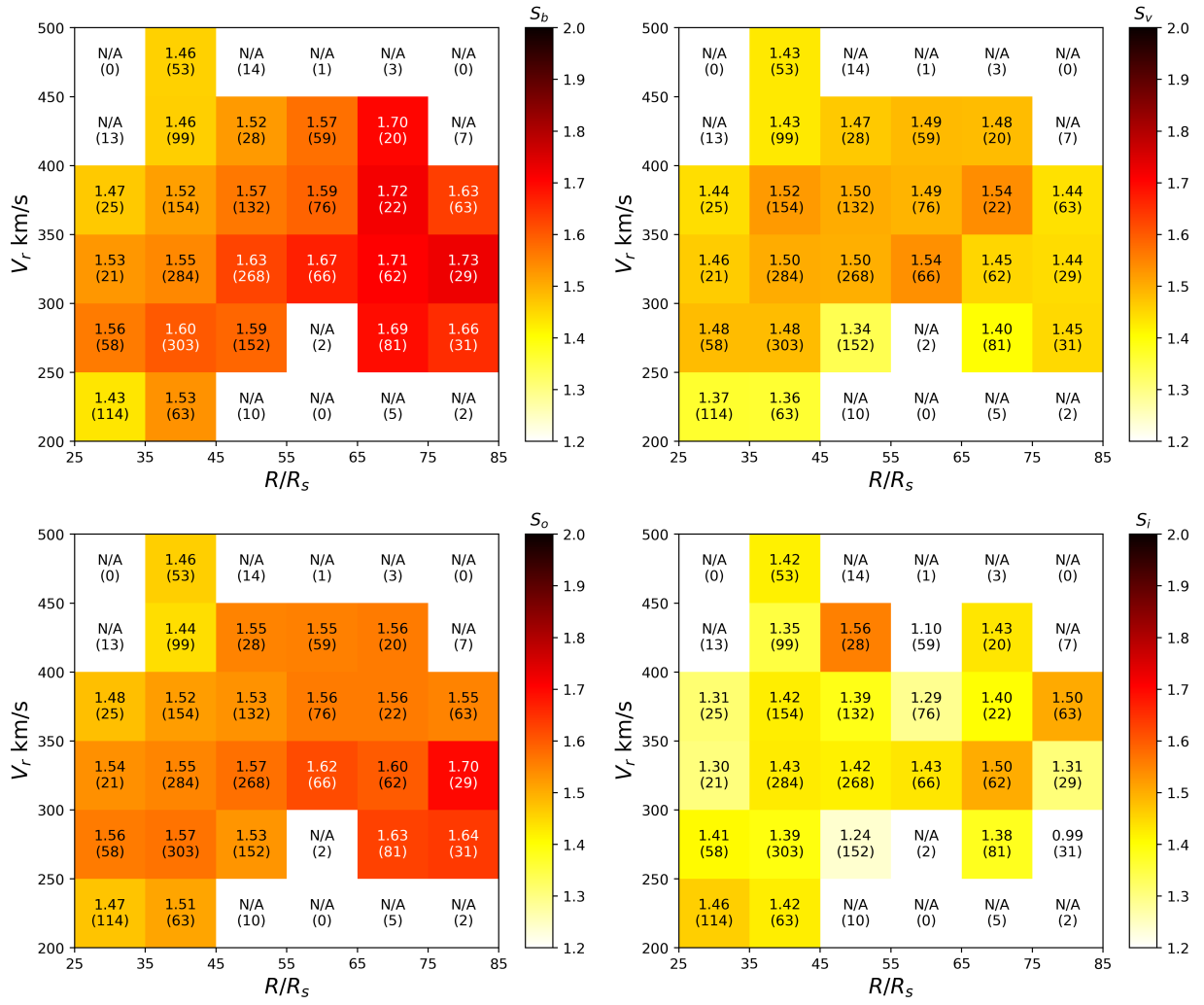

Figure 3.24: Spectral slopes of magnetic field (in Alfvén unit $\mathbf{B}/\sqrt{\mu_0\rho}$) (top-left panel), velocity (top-right panel), outward Elsässer variable (bottom-left panel), and inward Elsässer variable (bottom-right panel), as functions of radial distance to the Sun (x-axis) and radial solar wind speed V_r (y-axis). Colors of each block represent the median values of the binned data. Text on each block shows the value of the block and number of data points (in brackets) in the block.

long observed outside 0.3AU that the magnetic field spectrum is sleeper than the velocity spectrum (e.g. Grappin et al., 1991). Our results here show that, the difference between the two spectra seems to be a result of the dynamic evolution of solar wind turbulence. The spectral slope of $\mathbf{z_o}$ is close to that of magnetic field but slightly shallower. The spectral

slope of $\mathbf{z_i}$, on the other hand, resembles the velocity, i.e. does not show significant radial evolution and is even smaller than the velocity slope. In Figure 3.25 we show the correlation between S_o and S_b on left panel and correlation between S_v and S_b on right panel. Both of the two correlations are high, especially that between S_o and S_b. For reference, we mark $S_b = 5/3$ by the vertical lines and $S_o = 5/3$, $S_v = 3/2$ by the two horizontal lines. We see that, on average S_o is close to S_b, though slightly smaller, while S_v is clearly smaller than S_b such that $S_b = 5/3$ corresponds to a S_v around $1.55 - 1.6$. This result is similar to that reported by Grappin et al. (1991) (see their Figure 7) although the data used here is mainly within 0.3 AU while Grappin et al. (1991) analyzed Helios data that were collected outside 0.3 AU.

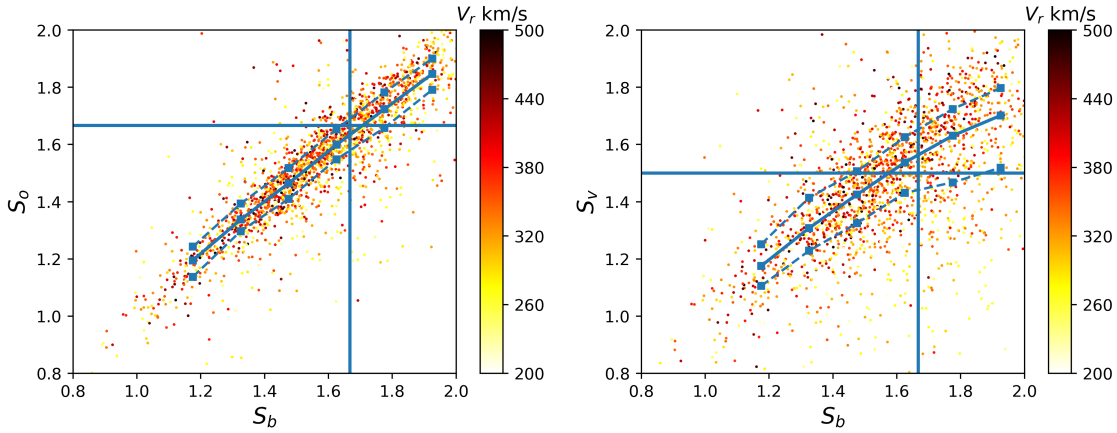

Figure 3.25: Left: spectral slope of outward Elsässer variable S_o as a function of the spectral slope of magnetic field S_b. Right: spectral slope of velocity S_v as a function of the spectral slope of magnetic field S_b. Vertical lines mark $S_b = 5/3$ Horizontal line on left panel mark $S_o = 5/3$ and horizontal line on right panel mark $S_v = 3/2$. Colors represent radial speed of the solar wind.

In Figure 3.26 we show the normalized cross helicity σ_c (left) and normalized residual energy σ_r as functions of radial distance to the Sun R and radial speed of the solar wind V_r. Only wave band 2, i.e. waves with periods between $900 - 450$ seconds, are shown while other wave bands show similar features. We first inspect σ_c on the left panel. In general, σ_c is of quite high values. A radial decrease of σ_c is seen, e.g. by looking at the blocks of

$V_r \in [300, 400]$ km/s, which is already reported by Chen et al. (2020) where only Encounter 1 data is analyzed and σ_c is calculated based on 6-hour time period. However, the negative radial dependence is not strong for other velocity segments such as $V_r < 300$km/s. If we look at blocks of $R \in [35, 45]R_s$ and $V_r \leq 400$km/s where substantial amount of data points fall, we can see a positive V_r dependence of σ_c. Again, in other radial distances, this correlation is not strong, possibly due to the lack of data points. Thus, data from future encounters is necessary. From the right panel of Figure 3.26, we observe a clear radial dependence of σ_r. Near perihelions of PSP encounters ($R < 45R_s$), σ_r is in general close to 0, i.e. kinetic and magnetic energies are almost equipartitioned in the fluctuations. Further out, evolution toward negative values is clearly observed. At 1 AU, a prevailing negative σ_r is observed and our results suggest that this negative σ_r is a result of the turbulence evolution in the inner heliosphere. Note that, Chen et al. (2020) does not report a radial decrease of σ_r. Instead, they found a negative σ_r (~ -0.3) at the perihelion of encounter 1 and a increase of σ_r with radial distance. The difference between their and our results may come from the fact that Chen et al. (2020) calculate σ_r by 6-hour averages while our calculation is confined to wave period smaller than 30 minutes. Thus, the result of Chen et al. (2020) may be influenced by some large-scale structures such as stream shears.

3.3.4 Discussion and future work

In Section 3.3.3, we present some statistical results on turbulence properties using PSP data. However, more analyses are necessary in order to fully undertand the evolution of solar wind turbulence. One outstanding question that arises is that, what roles do solar wind speed and radial distance to the Sun play in the evolution of the turbulence? The density fluctuation and temperature analyzed in Section 3.3.3 indicate that solar wind streams with different speeds can be very different at their origins. Except for the strong speed-dependent ion temperature, slow streams seem to contain stronger compressive fluctuations than the fast streams and these compressive fluctuations may influence properties of the Alfvénic turbulence. However, despite the varying plasma parameters, Figure 3.24 and 3.26 show

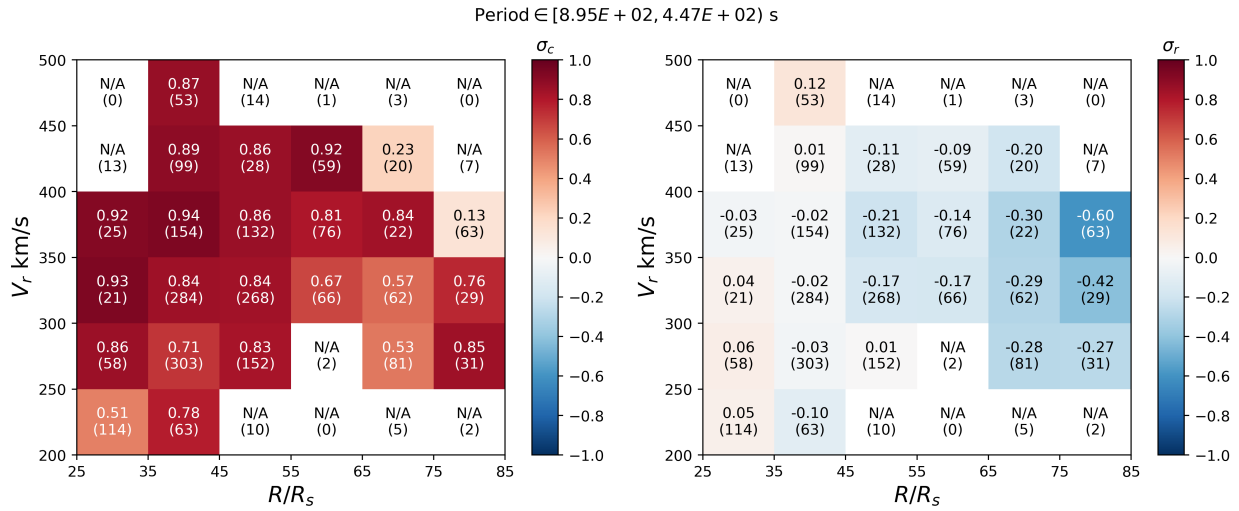

Figure 3.26: σ_c (left) and σ_r (right) of wave band 2 ($T \approx 900 - 450$ s) as functions of radial distance to the Sun R and radial speed of solar wind V_r. Colors of each block represent the median values of the binned data. Text on each block shows the value of the block and number of data points (in brackets) in the block.

that the turbulence properties do not have significant wind-speed dependence. Only the spectral slope of magnetic field S_b and σ_c show slight correlation with V_r. On the other hand, radial evolution of various quantities, i.e. S_b, S_o, σ_c and σ_r, is clearly observed. Indeed, by comparing the radial evolution of S_b for $V_r \in [300, 350]$km/s and $V_r \in [350, 400]$km/s, we can see a faster radial steepening process in the slower wind, indicating a possible scenario that some kind of "age", determined by both V_r and R, controls the evolution of turbulence (see Grappin et al., 1991). Another question, as already mentioned in Section 3.3.3, is that whether the discrepancy between velocity spectrum and magnetic field spectrum tends to diminish as we move close to the Sun. From Figure 3.24, it can be seen that S_b and S_v are similar at very small radial distances to the Sun and S_b steepens radially while S_v remains relatively constant. Last question, is it true that the negative residual energy measured outside 0.3 AU is a result of the dynamically evolving turbulence? From Figure 3.26, it seems true that residual energy is initially zero close to the Sun and evolves toward negative values as the solar wind propagates. To answer the above questions, we need a larger

volume of data from PSP to solidate our statistical results and data closer to the Sun. Thus, data from the next two encounters, especially Encounter 6, during which PSP will lower its perihelion to abount $20R_s$, are favored.

3.4 Conclusion

In this chapter, we present our studies on the solar wind turbulence. In the first part (Section 3.1), we carry out two-dimensional expanding-box-model (EBM) simulations and show that the large-scale stream interaction has significant impact on the Alfvénic fluctuations. In particular, the dominance of outward Alfvén waves is destroyed inside the stream shear region where the outward and inward Alfvén waves decay at different rates. In the second part (Section 3.2), we carry out simulations similar to those in Section 3.1 but with heliospheric current sheets embedded in the slow streams. We show that in the neighborhood of current sheets, the dominance of outward Alfvén waves is weakened and excess of magnetic energy is observed. We also do a superposed-epoch analysis of heliospheric current sheet crossings at 1 AU using OMNI data. Results of superposed-epoch analysis support the simulations. In the last part (Section 3.3), we show preliminary results by analyzing Parker Solar Probe data. The data clearly reveals the evolution of turbulence in the solar wind which is dependent on the radial distance to the Sun and also the solar wind speed. However, more analysis of PSP data is necessary before a solid conclusion is made. As Parker Solar Probe continues to lower its orbit toward the Sun, our knowledge of the early-stage turbulence will be refreshed in the future. Meanwhile, we propose to conduct improved numerical simulations with three-dimensional code and possibly with the accelerating expanding-box-model (AEBM) (Tenerani & Velli, 2017).

CHAPTER 4

Conclusion and Future Work

In this dissertation, we explored some aspects of two of the most fundamental processes in the inner heliosphere: magnetic reconnection and solar wind turbulence. Magnetic reconnection is believed to be the underlying mechanism that triggers most of the explosive phenomena in the heliosphere such as the coronal mass ejection and magnetic substorms. Turbulence is ubiquitous in the solar wind and plays a major role in many important processes, such as the heating of solar wind and generation of high-energy particles. Thus, understanding magnetic reconnection and solar wind turbulence is crucial for a complete description of the heliosphere.

Although the idea of reconnection was proposed in 1950s, significant progress on understanding how fast reconnection is initiated and proceeds from MHD scales was not made until recent years. It is now widely accepted that the fast-growing tearing mode instability dominates the reconnection process at MHD scales. In Chapter 2, we studied several problems related to tearing instability that were not fully understood. The first one regards the marginal stability of the current sheets at low Lundquist numbers. Prvious numerical work shows that a current sheet is susceptible to tearing instability only when its Lundquist number exceeds some threshold (Biskamp, 1986). Our analysis shows that, the inhomogeneous flow inside a reconnecting current sheet, such as a Sweet-Parker type current sheet, stabilizes the tearing instability if the Lundquist number is smaller than $O(10^4)$. The stabilization effect comes from three aspectes. First, the inhomogeneous flow directly decreases the growth rate of tearing instability. Second, the strethcing effect of the inhomogeneous flow changes the effective wave number. Third, the flow limits the growing period of the magnetic islands by ejecting the islands out of the current sheet. The second problem we discuss is the ef-

fect of ion-scale kinetic physics, i.e. Hall effect, on the recursive plasmoid generation. As shown by previous nonlinear MHD simulations of a collapsing current sheet (Tenerani et al., 2015), tearing instability leads to a recursive generation of secondary plasmoids and current sheets. We carried out nonlinear Hall-MHD simulations and showed that, the recursive reconnection process changes significantly when the current sheet thickness approaches the ion inertial length. The generation of secondary plasmoids and current sheets is suppressed by the Hall effect and a single X-point forms. In the last part of Chapter 2, we extended the linear analysis of tearing instability to a three-dimensional configuration in the presence of a guide field. We showed that, although a strong guide field makes the fastest growing mode oblique instead of parallel for small wave lengths, the most unstable mode on the whole wave vector plane does not change with the guide field and remains parallel to the reconnecting magnetic field.

Studies of solar wind turbulence have been conducted for several decades by means of satellite measurements, numerical simulations and analytical modeling and our understanding of the nature of the solar wind turbulence, especially Alfvénic turbulence, was well established. Researchers have realized that the large-scale structures in the solar wind, especially the fast-slow stream shears, have significant effects on the turbulence and the velocity shear effects have been assimilated in various turbulence models. In the first part of Chapter 3, we study numerically how the stream interaction regions affect the evolution of Alfvénic turbulence. We adopt the expanding-box-model so that our simulations are more self-consistent compared with previous works (e.g. Roberts et al., 1992). We show that stream shears are necessary in decreasing the dominance of outward propagating Alfvén waves observed in the solar wind since there is an asymmetry between the evolution of outward and inward waves inside the shear regions. However, we do not observe a magnetic energy excess inside the shear regions although the solar wind observations, at least observations at 1 AU, show a prevailing magnetic energy excess. We then explore numerically the influence of heliospheric current sheets on the turbulence. We show that, due to the weak radial magnetic field, the "Alfvén effect", which keeps the velocity and magnetic field correlated, is also week near

the current sheets. This results in a decoupling of velocity perturbation from magnetic field perturbation and leads to a magnetic field dominance with the aid of radial expansion effect of the solar wind. A superposed-epoch analysis using OMNI data collected at 1 AU supports the numerical results. In the last part of Chapter 3, we conduct a statistical analysis of the Parker Solar Probe data from its first four orbits. Our results indicate that, very close to the Sun $R \lesssim 30R_s$, the turbulence is in a highly Alfvénic state, with a dominance of outward propagating waves and almost equipartitioned kinetic and magnetic energies. In particular, the spectra of magnetic field and velocity have similar slopes close to the Sun (1.4-1.5) and the spectrum of magnetic field steepens toward the Kolmogorov slope (-5/3) while the spectrum of velocity has a nearly constant slope. These results may be important since they reveal that the turbulence is dynamically evolving in the inner heliosphere and should be considered when we establish self-consistent models of the solar wind turbulence.

Despite all the works that have been done so far, there are still a lot of open questions left. In Section 2.2, we presume an environment in which fast reconnection is already allowed to happen. However, how such environment, i.e. a current sheet with large aspect ratio $L/a \sim S^{1/3}$ with S to be the Lundquist number measured by L, forms is still not fully understood. This is the so called "onset" problem of the reconnection. Whether it is in the solar corona or in the Earth's magnetotail, some kind of energy build-up process is necessary and the underlying mechanism may be complicated and highly dependent on external environments. For example, in the corona, the onset of fast reconnection before solar flares or CMEs is highly dependent on the topology of magnetic field near the neutral lines embedded in the photosphere (Chen, 2011). Solution of the onset problem is not easy and needs comprehensive analysis of specific plasma environments. Another question is how the recursive reconnection proceeds in three-dimensional configuration with guide field. Although our linear calculation predicts that the fastest-growing mode is parallel, i.e. two-dimensional or slab, in nonlinear stage the physics is much more complex and thus the third dimension might be nontrivial. Besides, in the solar corona, topology of the magnetic field lines is usually complicated and may result in conditions where oblique tearing mode is

most important, e.g. when the parallel wave length is limited. Other configurations such as double current sheet may also be common in the solar corona where the nonlinear tearing instability can be quite different from the single current sheet case (e.g. Baty, 2017). To fully understand these processes, large-scale numerical simulations will be carried out in the future.

As presented in Chapter 3, Parker Solar Probe data provides us with unprecedented insights on the young solar wind turbulence. Although we have obtained some preliminary results so far, more analyses of its data are necessary in order to answer the following questions regarding the turbulence. First, what is the nature of the MHD turbulence at its origin? Is it purely, or at least nearly, Alfvénic close to the Sun? Our results shown in Section 3.3 suggest so but we need data from more orbits to solidate this conclusion. Second, how are the discrepancies between velocity fluctuation and magnetic fluctuation generated? Here, the discrepancies refer to the excess of magnetic energy over kinetic energy and also the different spectral slopes of the two fields. In Section 3.3, we show that these discrepancies seem to vanish as we get close to the Sun but again, we should confirm this result with more PSP data in the future. Third, how important are the velocity shears and current sheets for the evolution of the young turbulence? In Section 3.3, we do not remove any stream interaction regions or current sheet crossings. It will be necessary to carefully analyze the effects of these structures. Fourth, is the compressive component in the turbulence important? As shown in Section 3.3, the density fluctuation is anti-correlatd with the solar wind speed. For very slow wind ($V_r \lesssim 300$ km/s), the relative density flucuation can be quite large, say, larger than 0.2. Thus, the compressive fluctuations may play a role in the evolution of turbulence, especially in the slow solar wind. We will combine the PSP data with numerical simulations to study the young solar wind turbulence. Compared with those presented in Chapter 3, our future simulations will be three-dimenional and take the acceleration of solar wind into consideration (Tenerani & Velli, 2017). Besides, with deeper insight of the young turbulence, we will work to establish more self-consistent models for the solar wind turbulence.

APPENDIX A

Series-expansion Method for Solving Ordinary Differential Equation Set

Eq (2.20) is a 5th order homogeneous boundary value problem (BVP) with a regular singular point $y = 0$. The widely used methods for BVPs, e.g. the shooting method, usually involve the integrals of the ODEs over the domain. However, for ODEs with singular points such as Eq (2.20) it is hard to evaluate the integrals. Thus we adopt the method of series-expansion to solve Eq (2.20). For simplicity, we write Eq (2.20) in the form

$$\mathcal{L}(v, b|\gamma, k, S) = 0 \tag{A.1}$$

where $\mathcal{L}$ is the linear operator corresponding to the ODE set with γ, k, S (and $B_0(y)$) as parameters. Our goal is, by imposing proper boundary conditions, to determine the dispersion relation $\gamma(k)$ and the solution $v(y)$ and $b(y)$ simultaneously.

Before discussing the series expansion method, we would like to first clarify the boundary conditions. The equation is 5th order so 5 boundary conditions are needed. We set the domain to be $y \in [0, L_y]$ where $L_y = 17$ so that the right boundary is far enough to impose the asymptotic boundary conditions. We expect v to be odd and b to be even in y so that

$$v(0) = 0, \quad b'(0) = 0 \tag{A.2}$$

For large enough y, $B_0(y)$ (Eq (2.8)) can be approximated by

$$B_0(y) \approx 1.31 \times \frac{1}{y} + O(1/y^3) \tag{A.3}$$

Far from the center of the current sheet, the perturbations asymptote to 0. Plugging Eq (A.3) in Eq (2.20) and eliminating v, we get a 5th order ODE for b, which by keeping only

the 5th and 4th order derivative terms a priori, becomes

$$b^{(5)} + (yb)^{(4)} = 0 \tag{A.4}$$

which gives the solution

$$b(y) \propto \exp(-\frac{1}{2}y^2) \tag{A.5}$$

and we further get

$$v(y) = \frac{1}{1.31} \times S^{-\frac{1}{2}} \frac{k^2 + \gamma + 2}{k} yb(y) \tag{A.6}$$

The 3 boundary conditions at the right boundary are then given by

$$b' + L_y b = 0 \tag{A.7a}$$

$$v' + (L_y - \frac{1}{L_y})v = 0 \tag{A.7b}$$

$$v - \frac{1}{1.31} S^{-\frac{1}{2}} \frac{k^2 + \gamma + 2}{k} L_y b = 0 \tag{A.7c}$$

Eq (A.2) and (A.7) are the 5 boundary conditions for the BVP. Note that Eq (A.7) are not equivalent to open-boundary conditions adopted in the simulations unless $L_y \to \infty$ where all 1st order quantities vanish. But as the simulation box is large enough $\max(|y|) \sim 10a$ and the initial perturbations are localized around $y = 0$, the difference in the boundary conditions is negligible and we are still allowed to make comparisons between the linear theory and the simulations.

We expand $v(y)$, $b(y)$ and $B_0(y)$ in power series of y around a point y_c

$$v(y) = \sum_{n=0}^{N} v_n (y - y_c)^n, \quad b(y) = \sum_{n=0}^{N} b_n (y - y_c)^n, \quad B_0(y) = \sum_{n=0}^{N} B_n (y - y_c)^n \tag{A.8}$$

where v_n and b_n are quantities to be determined and $N = 100$ is the cut-off order of the series. B_n are given by the Taylor expansion of $B_0(y)$ around y_c. Once we get the values of v_n and b_n, the solution $v(y)$ and $b(y)$ can be recovered. We plug Eq (A.8) into Eq (2.20) and

get the recurrence relations by matching the coefficients in front of $(y-y_c)^n$:

$$\begin{aligned} y_c(n+3)(n+2)(n+1)v_{n+3} =&(n+2)(n+1)(\gamma+1-n)v_{n+2}+k^2y_c(n+1)v_{n+1} \\ &-(\gamma-1-n)k^2v_n+kS^{\frac{1}{2}}\sum_{l=0}^{n}\big[(l+2)(l+1)B_{n-l}b_{l+2} \\ &-k^2B_{n-l}b_l-(n-l+2)(n-l+1)B_{n-l+2}b_l\big] \end{aligned} \tag{A.9a}$$

$$(n+2)(n+1)b_{n+2}=(\gamma+1-n+k^2)b_n-y_c(n+1)b_{n+1}-kS^{\frac{1}{2}}\sum_{l=0}^{n}B_{n-l}v_l \tag{A.9b}$$

From Eq (A.9) it is obvious that there are only 5 free parameters $(v_0, v_1, v_2, b_0, b_1)$: all the v_n for $n \geq 3$ and b_n for $n \geq 2$ can be expressed in the 5 free parameters and so for $v(y)$ and $b(y)$:

$$v(y)=v(y|v_0,v_1,v_2,b_0,b_1), \quad b(y)=b(y|v_0,v_1,v_2,b_0,b_1) \tag{A.10}$$

Then the 5 boundary conditions can be written as a linear algebraic equation set

$$\mathbf{M}(\gamma,k,S)\mathbf{V}=0 \tag{A.11}$$

where $\mathbf{V}=(v_0,v_1,v_2,b_0,b_1)^T$ and $\mathbf{M}$ is a matrix which is a function of γ, k, S. In order to get a nontrivial solution, we need

$$\det(\mathbf{M})=0 \tag{A.12}$$

which gives the dispersion relation $\gamma(k,S)$ and then we get $v(y)$ and $b(y)$.

In practice, we must do the expansion at multiple points (y_c) to ensure convergence of the series. If we use N_c points to expand the functions, we need $5N_c$ equations to determine the solution. Apart from the 5 boundary conditions Eq (A.2) and (A.7), the other $5(N_c-1)$ equations come from the continuities of $v(y)$, $v'(y)$, $v''(y)$, $b(y)$, $b'(y)$ at N_c-1 junction points (y_m), each of which lies between two neighbouring expansion points. In solving Eq (2.20) we use 11 expansion points.

APPENDIX B

Description of the MHD code

The MHD code used in our studies was developed based on the version in (Landi et al., 2005). Here I must acknowledge Anna Tenerani who shared the original code with me and gave me a lot of help in learning the code. In addition, Franco Rappazzo, as an expert in MHD simulations, gave me many useful suggestions.

Several versions varying in programming language (either C or Fortran), boundary condition, numerical scheme, and equation set were developed. We have both two- and three-dimensional versions and all versions are parallelized via Message Passing Interface (MPI).

B.1 Equation Set

The basic equation set used in the code is the MHD equation set with resistive and viscous terms. To achieve the goals of our studies, we implemented linear terms, Hall term, and expanding-box module to the code as described in Section 2.1, 2.2, and 3.1. For purely spectral code, such that used in Section 3.1 and 3.2, we write the equation set in conservation-form, otherwise convective-form equation is used.

B.2 Numerical Scheme

Explicit third order Runge-Kutta method is adopted to integrate the equation:

$$\mathbf{f_i} = \mathbf{f_{i-1}} + dt \times \left[c_i \times \left(\frac{d\mathbf{f}}{dt} \right)_i + d_i \times \left(\frac{d\mathbf{f}}{dt} \right)_{i-1} \right] \tag{B.1}$$

where $i = 1, 2, 3$ and

$$\begin{aligned} c_1 &= \frac{8}{15}, \quad c_2 = \frac{5}{12}, \quad c_3 = \frac{3}{4} \\ d_1 &= 0, \quad d_2 = -\frac{17}{60}, \quad d_3 = -\frac{5}{12} \end{aligned} \tag{B.2}$$

f_3 will be the final, integrated field.

To calculate spatial derivatives, two types of methods are implemented. The first one is spectral method. We apply Fourier transform to field $f(x)$ on a discrete grid such that

$$\hat{f}_k = \sum_{j=0}^{n-1} f_j e^{-i\frac{2\pi}{n}jk} \tag{B.3}$$

where $f_j = f(j\Delta x)$ is value of f on jth grid point, n is the total number of grid points, k is the wave number. Since the inverse Fourier transform gives

$$f_j = \sum_{k=0}^{n-1} \hat{f}_k e^{i\frac{2\pi}{n}jk}, \tag{B.4}$$

we can calculate the derivative of f by

$$\left(\frac{df}{dx}\right)_j = \sum_{k=0}^{n-1} i\frac{2\pi k}{n\Delta x}\hat{f}_k e^{i\frac{2\pi}{n}jk} \tag{B.5}$$

Apparently, spectral method is only applicable to periodic boundary condition.

The second method is compact-finite-difference (CFD) scheme first proposed by Lele (1992). It is a"spectral-like" finite difference scheme taking the form

$$\beta f'_{i-2} + \alpha f'_{i-1} + f'_i + \alpha f'_{i+1} + \beta f'_{i+2} = c\frac{f_{i+3} - f_{i-3}}{6\Delta x} + b\frac{f_{i+2} - f_{i-2}}{4\Delta x} + a\frac{f_{i+1} - f_{i-1}}{2\Delta x} \tag{B.6}$$

where prime means spatial derivative and constant coefficients α, β, a, b, c are given by matching Taylor series on the two sides of the equation to a chosen order of error. As this scheme couples the derivatives to be calculated at neighboring grid points, a global matrix inversion is needed to simultaneously determine f'_i. In our code, 6th order scheme is adopted.

Since both spectral method and the original CFD scheme require information on global scale, *scalability* of parallelization is significantly limited. To resolve this problem, we implement an improved CFD scheme (Kim & Sandberg, 2012) which only needs several halo points from adjacent block of grid points and thus is much more efficient under parallelization.

For spectral method, we apply the standard de-aliasing by zero-padding wave modes larger than $\frac{1}{3}n$ where n is number of grid points. For CFD schemes, we apply numerical filters to remove the large wave number oscillations (see Lele, 1992; Kim & Sandberg, 2012).

B.3 Boundary Condition

Two types of boundary conditions are available. One is periodic and the other is open, or non-reflecting. Periodic boundary condition is easy to implement so here we focus on how to impose open boundary condition.

The ideal MHD equation set is a partial differential equation system and can be written in the form:

$$\frac{\partial \mathbf{U}}{\partial t} + \mathbf{A}\frac{\partial \mathbf{U}}{\partial x} + \mathbf{C}\frac{\partial \mathbf{U}}{\partial y} = 0 \tag{B.7}$$

where

$$\mathbf{U} = (\rho, u_x, u_y, u_z, B_x, B_y, B_z, P) \tag{B.8}$$

The calculation of the characteristics is already shown in (Landi et al., 2005). For example, along x, we first diagonalize matrix $\mathbf{A}$

$$\mathbf{A} = \mathbf{S}\mathbf{\Lambda}\mathbf{S^{-1}} \tag{B.9}$$

where the diagonal matrix

$$\Lambda = \mathrm{diag}\{u_x + f_x, u_x + a_x, u_x + s_x, u_x, u_x - s_x, u_x - a_x, u_x - f_x\} \tag{B.10}$$

consists of the speeds of the 7 MHD modes (projected along the x direction). u_x, s_x, a_x, f_x are the local entropy mode (flow) speed, slow magnetosonic wave speed, Alfvén speed and fast magnetosonic wave speed projected along x. Note that when we calculate the characteristics along x, there is no need to consider B_x because of the divergence-free condition. Then we are able to decompose $\mathbf{A}\partial\mathbf{U}/\partial x$ into linear combinations of the 7 characteristics.

In order to impose open-boundary condition on a certain side of the simulation box, we decompose the corresponding derivatives into the linear combination of the characteristics,

e.g., decompose the x-derivative terms at the right/left boundaries. For each of the 7 characteristics, we decide whether it is propagating inward or outward of the domain by looking at its mode speed. If it is outgoing, we keep this characteristic; otherwise we set it as 0. By doing this we ensure that no information is going into the simulation domain and the boundary is "open".

For non-ideal MHD equation, the 2nd order derivative terms and other source terms produce some reflections at the boundaries. If they are significantly small it is safe to neglect them at the boundaries, otherwise we need to taper these terms close to the boundaries.

APPENDIX C

List of heliospheric current sheet crossings identified using OMNI data

The full list of HCS-crossings (refer to Section 3.2) is shown in Table C.1.

solar maximum					
#	year	month	day	hour	minute
01	2000	01	10	00	30
02	2000	02	05	17	50
03	2000	07	31	19	40
04	2000	08	27	17	33
05	2000	09	24	15	50
06	2000	10	14	18	04
07	2000	11	23	19	33
08	2000	12	16	21	03
09	2000	12	22	21	23
10	2001	01	10	21	03
11	2001	02	14	07	17
12	2001	03	12	14	55
13	2001	04	22	00	23
14	2001	05	06	10	40
15	2001	05	17	21	32
16	2001	06	29	06	21
17	2001	07	10	16	30

18	2001	07	24	15	05
19	2001	11	16	11	28
20	2002	02	04	21	21
21	2002	03	03	22	49
22	2002	05	06	09	55
23	2002	06	02	02	40
24	2002	06	16	06	08
25	2002	06	25	16	37
26	2002	09	03	06	46
27	2002	09	27	05	29
28	2002	10	23	17	02
29	2002	11	10	02	57
30	2002	12	06	11	21
31	2002	12	19	07	41
32	2003	01	17	14	08
33	2003	02	12	22	54
34	2003	02	26	19	48
35	2003	03	11	17	18
36	2003	03	26	09	40
37	2003	04	08	02	34
38	2003	04	20	19	07
39	2003	05	04	16	00
40	2003	05	18	16	23
41	2003	06	26	12	30
42	2003	07	11	15	25
43	2003	07	26	12	01
44	2003	08	04	06	52
45	2003	09	01	06	13

46	2003	10	13	09	27
47	2003	12	05	01	26
48	2003	12	19	19	50

solar minimum

#	year	month	day	hour	minute
01	2007	01	08	02	01
02	2007	01	15	08	39
03	2007	02	04	01	44
04	2007	02	12	15	17
05	2007	03	03	08	18
06	2007	03	11	18	17
07	2007	03	31	23	21
08	2007	06	02	15	19
09	2007	06	08	01	24
10	2007	06	13	18	59
11	2007	08	05	16	02
12	2007	08	31	20	25
13	2007	09	09	23	45
14	2007	10	11	06	22
15	2007	11	20	09	33
16	2007	12	17	06	12
17	2008	01	12	13	06
18	2008	01	31	15	24
19	2008	02	07	17	25
20	2008	02	27	17	03
21	2008	03	08	08	01
22	2008	04	03	03	00
23	2008	04	22	15	28

24	2008	04	30	16	56
25	2008	06	25	16	14
26	2008	07	21	03	41
27	2008	07	30	10	50
28	2008	08	24	23	43
29	2008	11	07	03	51
30	2008	12	03	15	40
31	2008	12	11	00	09
32	2009	01	23	13	54
33	2009	02	03	00	59
34	2009	04	15	08	27
35	2009	05	13	19	36
36	2009	06	20	19	18
37	2009	07	13	13	23
38	2009	07	20	10	21
39	2010	01	31	02	21
40	2010	03	01	06	52
41	2010	03	14	23	10
42	2010	06	06	23	58
43	2010	08	20	10	01
44	2010	11	12	11	26
45	2010	12	23	16	26

Table C.1: List of HCS-crossings identified using OMNI data

Bibliography

Akçay, C., Daughton, W., Lukin, V. S., & Liu, Y.-H. 2016, Physics of Plasmas, 23, 012112

Alazraki, G., & Couturier, P. 1971, Astronomy and Astrophysics, 13, 380

Ascher, U. M., Mattheij, R. M., & Russell, R. D. 1994, Numerical solution of boundary value problems for ordinary differential equations, Vol. 13 (Siam)

Athay, R. G. 2012, The solar chromosphere and corona: Quiet Sun, Vol. 53 (Springer Science & Business Media)

Baalrud, S., Bhattacharjee, A., & Huang, Y.-M. 2012, Physics of Plasmas, 19, 022101

Bale, S., Badman, S., Bonnell, J., et al. 2019, Nature, 576, 237

Barkhudarov, M. 1991, Solar Physics, 135, 131

Baty, H. 2017, The Astrophysical Journal, 837, 74

Bavassano, B., Dobrowolny, M., Mariani, F., & Ness, N. 1982, Journal of Geophysical Research: Space Physics, 87, 3617

Belcher, J. 1971, The Astrophysical Journal, 168, 509

Belcher, J., & Davis Jr, L. 1971, Journal of Geophysical Research, 76, 3534

Birn, J., Drake, J., Shay, M., et al. 2001, Journal of Geophysical Research: Space Physics, 106, 3715

Biskamp, D. 1986, The Physics of fluids, 29, 1520

Borovsky, J. E., & Denton, M. H. 2010, Journal of Geophysical Research: Space Physics, 115

Bruno, R., & Bavassano, B. 1991, Journal of Geophysical Research: Space Physics, 96, 7841

Bulanov, S., Syrovatskii, S., & Sakai, J. 1978, JETP Letters, 28, 177

Burch, J., Moore, T., Torbert, R., & Giles, B. 2016a, Space Science Reviews, 199, 5

Burch, J., Torbert, R., Phan, T., et al. 2016b, Science, 352, aaf2939

Cao, F., & Kan, J. 1991, Journal of Geophysical Research: Space Physics, 96, 5859

Cassak, P., Shay, M., & Drake, J. 2010, Physics of Plasmas, 17, 062105

Chen, C., Bale, S., Salem, C., & Maruca, B. 2013, The Astrophysical Journal, 770, 125

Chen, C., Bale, S., Bonnell, J., et al. 2020, The Astrophysical Journal Supplement Series, 246, 53

Chen, P. 2011, Living Reviews in Solar Physics, 8, 1

Coleman, Paul J., J. 1968, ApJ, 153, 371, doi: 10.1086/149674

Coppi, B., Greene, J. M., & Johnson, J. L. 1966, Nuclear Fusion, 6, 101

Cranmer, S. R., & Van Ballegooijen, A. 2005, The Astrophysical Journal Supplement Series, 156, 265

Daughton, W., Roytershteyn, V., Albright, B., et al. 2009, Physical review letters, 103, 065004

Daughton, W., Scudder, J., & Karimabadi, H. 2006, Physics of Plasmas, 13, 072101

de Wit, T. D., Krasnoselskikh, V. V., Bale, S. D., et al. 2020, The Astrophysical Journal Supplement Series, 246, 39

Drake, J., Swisdak, M., Phan, T., et al. 2009, Journal of Geophysical Research: Space Physics, 114

D'Amicis, R., & Bruno, R. 2015, The Astrophysical Journal, 805, 84

Eselevich, V., & Filippov, M. 1988, Planetary and space science, 36, 105

Furth, H. P., Killeen, J., & Rosenbluth, M. N. 1963, The physics of Fluids, 6, 459

Giacalone, J., Jokipii, J. R., & Mazur, J. 2000, The Astrophysical Journal Letters, 532, L75

Grappin, R., Mangeney, A., & Marsch, E. 1990, Journal of Geophysical Research: Space Physics, 95, 8197

Grappin, R., & Velli, M. 1996, Journal of Geophysical Research: Space Physics, 101, 425

Grappin, R., Velli, M., & Mangeney, A. 1991, in Annales Geophysicae, Vol. 9, 416–426

Grappin, R., Velli, M., & Mangeney, A. 1993, Physical review letters, 70, 2190

Heinemann, M., & Olbert, S. 1980, Journal of Geophysical Research: Space Physics, 85, 1311

Hellinger, P., Matteini, L., Štverák, Š., Trávníček, P. M., & Marsch, E. 2011, Journal of Geophysical Research: Space Physics, 116

Hietala, H., Drake, J., Phan, T., Eastwood, J., & McFadden, J. 2015, Geophysical research letters, 42, 7239

Hollweg, J. V. 1974, Journal of Geophysical Research, 79, 1539

Huang, Y.-M., Bhattacharjee, A., & Sullivan, B. P. 2011, Physics of Plasmas, 18, 072109

Iroshnikov, P. 1964, Soviet Astronomy, 7, 566

Kierzenka, J., & Shampine, L. F. 2001, ACM Transactions on Mathematical Software (TOMS), 27, 299

Kim, J. W., & Sandberg, R. D. 2012, Computers & Fluids, 58, 70

King, J., & Papitashvili, N. 2005, Journal of Geophysical Research: Space Physics, 110

Kiyani, K. H., Osman, K. T., & Chapman, S. C. 2015, Dissipation and heating in solar wind turbulence: from the macro to the micro and back again, The Royal Society Publishing

Kolmogorov, A. N. 1941, Cr Acad. Sci. URSS, 30, 301

Kraichnan, R. H. 1965, The Physics of Fluids, 8, 1385

Kuperus, M., Ionson, J. A., & Spicer, D. S. 1981, Annual Review of Astronomy and Astrophysics, 19, 7

Landi, S., Velli, M., & Einaudi, G. 2005, The Astrophysical Journal, 624, 392

Lele, S. K. 1992, Journal of computational physics, 103, 16

Liu, Y.-H., Drake, J., & Swisdak, M. 2011, Physics of Plasmas, 18, 062110

Liu, Y.-H., Hesse, M., Guo, F., et al. 2017, Physical Review Letters, 118, 085101

Loureiro, N., Schekochihin, A., & Cowley, S. 2007, Physics of Plasmas, 14, 100703

Loureiro, N., Schekochihin, A., & Uzdensky, D. 2013, Physical Review E, 87, 013102

Lu, S., Angelopoulos, V., Artemyev, A., et al. 2019, The Astrophysical Journal, 878, 109

Ma, Z., & Bhattacharjee, A. 2001, Journal of Geophysical Research: Space Physics, 106, 3773

Marsch, E., & Tu, C.-Y. 1990, Journal of Geophysical Research: Space Physics, 95, 8211

McManus, M. D., Bowen, T. A., Mallet, A., et al. 2020, The Astrophysical Journal Supplement Series, 246, 67

Ni, L., Germaschewski, K., Huang, Y.-M., et al. 2010, Physics of Plasmas, 17, 052109

Osterbrock, D. E. 1961, The Astrophysical Journal, 134, 347

Parker, E. N. 1957, Journal of Geophysical Research, 62, 509

Parker, E. N. 1958, The Astrophysical Journal, 128, 664

Petschek, H. E. 1964, NASA Special Publication, 50, 425

Pucci, F., & Velli, M. 2013, The Astrophysical Journal Letters, 780, L19

Pucci, F., Velli, M., & Tenerani, A. 2017, The Astrophysical Journal, 845, 25

Roberts, D., Goldstein, M., Klein, L., & Matthaeus, W. 1987a, Journal of Geophysical Research: Space Physics, 92, 12023

Roberts, D., Klein, L., Goldstein, M., & Matthaeus, W. 1987b, Journal of Geophysical Research: Space Physics, 92, 11021

Roberts, D. A., Goldstein, M. L., Matthaeus, W. H., & Ghosh, S. 1992, Journal of Geophysical Research: Space Physics, 97, 17115

Shepherd, L. S., & Cassak, P. 2010, Physical review letters, 105, 015004

Shi, C., Tenerani, A., Velli, M., & Lu, S. 2019, The Astrophysical Journal, 883, 172

Shi, C., Velli, M., & Tenerani, A. 2018, The Astrophysical Journal, 859, 83

Shi, C., Velli, M., Tenerani, A., Rappazzo, F., & Réville, V. 2020, The Astrophysical Journal, 888, 68

Shibata, K., & Tanuma, S. 2001, Earth, Planets and Space, 53, 473

Siscoe, G. 1972, Journal of Geophysical Research, 77, 27

Smith, E. J. 2001, Journal of Geophysical Research: Space Physics, 106, 15819

Sweet, P. 1958, in IAU Symp. 6, Vol. 123, Kluwer Academic Publishers

Tajima, T., & Shibata, K. 2002, Plasma Astrophysics (Boulder), Westview Press

Tenerani, A., & Velli, M. 2017, The Astrophysical Journal, 843, 26

—. 2020, Monthly Notices of the Royal Astronomical Society, 491, 4267

Tenerani, A., Velli, M., Pucci, F., Landi, S., & Rappazzo, A. F. 2016, Journal of Plasma Physics, 82

Tenerani, A., Velli, M., Rappazzo, A. F., & Pucci, F. 2015, The Astrophysical Journal Letters, 813, L32

Tu, C.-Y., Pu, Z.-Y., & Wei, F.-S. 1984, Journal of Geophysical Research: Space Physics, 89, 9695

Velli, M. 1993, Astronomy and Astrophysics, 270, 304

Velli, M., Grappin, R., & Mangeney, A. 1991, Geophysical & Astrophysical Fluid Dynamics, 62, 101

Virtanen, P., Gommers, R., Oliphant, T. E., et al. 2020, Nature Methods, 1

Zank, G., Adhikari, L., Hunana, P., et al. 2017, The Astrophysical Journal, 835, 147

Zank, G., Matthaeus, W., & Smith, C. 1996, Journal of Geophysical Research: Space Physics, 101, 17093

Zhou, Y., & Matthaeus, W. H. 1990, Journal of Geophysical Research: Space Physics, 95, 10291